

Development of Carbon Materials for Use in Photosystem I-Based Biohybrid Devices

By

Christopher David Stachurski

Dissertation

Submitted to the Faculty of the
Graduate School of Vanderbilt University
in partial fulfillment of the requirements

for the degree of

DOCTOR OF PHILOSOPHY

in

Chemistry

August 31st, 2021

Nashville, Tennessee

Approved:

David E. Cliffel, Ph.D.

G. Kane Jennings, Ph.D.

Janet E. Macdonald, Ph.D.

Sandra J. Rosenthal, Ph.D.

Copyright © 2021 by Christopher David Stachurski
All rights reserved

For my family, especially Mom, Nick, and Sophie

ACKNOWLEDGEMENTS

I would first like to thank the members of the Vanderbilt community who have supporting this work, both directly and indirectly, without whom this work would not have been possible.

From my advisory committee, I would like to first thank my mentor Dr. David Cliffler, for letting me grow as a scientist in the ways I saw fit and letting me pursue my ideas within the PSI side of the group. Alongside Dr. Cliffler has been Dr. Kane Jennings, an invaluable leader on the PSI team, who was there to challenge my ideas and encouraged me to look at my research with a broad lens. Dr. Janet Macdonald first introduced me to nanoparticles and materials as a field and has been there with guidance and assistance along the way. The final member to join my committee, Dr. Sandra Rosenthal, offered significant knowledge pertaining to nanoparticles and nanomaterials, but also kept me thinking about how I would translate my results and ideas as publications or contributions for the growth of my field. Each member has added to my committee in their own way, and I will continue to grow and challenge myself as they have taught me. Outside of my graduate school committee, Dr. Susan Verberne-Sutton has also been an amazing friend, mentor, and sponsor. Thank you for taking time out of your day to talk AFM or teaching, and for letting me discover my love for teaching in your classes.

Over the past five years there have been many people who have helped me grow into the scientist I am today. Yet no one has helped me as much as my family, who is always supporting me in any way they can, while motivating me to be the best version of myself. At the center of my team, I need to acknowledge my mom, Nick, and Sophie for persisting through this process with me, pushing me when I needed it, as well as being there for Fortnite shenanigans. Nick and Sophie, I look forward for opportunities to support you two as you build your own paths through school and beyond. Grace, Neena, Dadoo, Auntie Sharon and Bobby are also to thank for being there as

sounding boards for whenever it was needed, both for things research and life related. Finally Quinn, you have motivated me in your own way and will continue to do so as I take on bigger and bolder roles in both my scientific career as well as life. I confidently go forward to my next role knowing that the Meowscles Squad will be ready to drop for a round or two (of wins of course) whenever I need them.

During my push during these last two years, Shannon Smith also had my back and was always ready to learn new board games or practice presentations and job talks. The rest of the Smiths, especially Gary and Becky, were also there to encourage me at the end of my time in graduate school, as well as through the final miles of a solo Percy Warner Marathon. Shannon, I look forward to seeing and celebrating your accomplishments as you finish your program with a bang!

I am humbled by the number of friends I have made throughout the past five years, both in lab as well as throughout Nashville. Dr. Andrew Kantor, you too have been such an inspiration and a motivation to pursue that which interests me, and to always keep my eyes set on the prize. Dr. Kody Wolfe, I cannot thank you enough for all the time spent talking about life and science, both over coffee, beers, and long runs. I look forward to reuniting at conferences and exploring the frontiers of our new fields with you to the latest hits from Jimmy Buffet. Dr. Megan van der Horst, thank you for motivating me both in long runs and long experiments, through the example you set by your own life. I look forward to exploring new trails and routes with you in DC. Johnny Cordoba was a true friend as well, and I fondly look back at our apartment shenanigans during our two years living together.

From the Clifflab, thanks to Dr. Dilek Dervishogullari, Dr. Ethan McLain and Dr. Sara Melow for your support through practice exams, research talks, and talking about research in

general. Margaret Calhoun, thank you for always challenging me to be the best scientist I can be. I look forward to seeing the culmination of your own research very soon! To the old guard, Dr. Aaron Daniel, Dr. Evan Gizzie, Dr. Max Robinson, Dr. David Crisostimo, Dr. Adam Travis, thank you for making the transition to graduate school as seamless as possible and for putting me on track with my own PSI-related projects. And to the new guard, especially Matt Galazzo, LTC John Williams, William Lowery and Nicholas Hortance – continue to explore bigger and bolder ideas within the PSI subgroup. From the Jennings group, Josh Passantino and Marc Nabhan, thank you for your input both in the lab and during PSI subgroup meetings. I look forward to seeing your own advances to the field of PSI biohybrid solar cells.

A special thanks goes to Sophia Click, for both assisting with carbon nanoparticle characterization as well as sparking my interest in Dungeons and Dragons. I would also like to thank the many graduate and undergraduate students I have had the privilege of mentoring over the past five years. In particular, Jade Stanley, Pamela Tabaquin and Steve Park for both their insight into my ongoing research projects as well as for teaching me the importance of clearly communicating science and being a good mentor. From home I need also need to thank DnD squad, Michael Gaudio, Mary Gaudio, and Michael Murphy, for being amazing friends and for bearing with me as we figure out the rules together.

The Vanderbilt Institute for Nanoscale Science and Engineering (VINSE) staff, specifically Dr. James McBride and Dr. Dmitry Koktysh also deserve significant thanks for their help using the many instruments and microscopy techniques used to characterize the materials discussed in this dissertation. And Finally, I would like to thank our funding sources over the past few years, the National Science Foundation (DMR-1507505), the United States Department of Agriculture (2013-67021-21029 & 2019-67021-29857).

Table of Contents

1. INTRODUCTION	1
2. MATERIALS AND METHODS.....	11
2.1. Extraction of Photosystem I from Whole Leaf Spinach	11
2.2. Quantification of Extracted PSI.....	15
2.3. Assembly of Photosystem I Films/Composites for Solar Energy Conversion	16
2.4. Electrochemical Techniques and Analyses.....	18
2.4.1. Cyclic Voltammetry.....	18
2.4.2. Photochronoamperometry.....	21
3. DESIGN OF CARBON NANOPARTICLES FOR ENHANCED ELECTRON TRANSFER WITH PHOTOSYSTEM I.....	23
3.1 Optical and Electrochemical Tuning of Hydrothermally Synthesized Nitrogen-Doped Carbon Dots	23
3.1.1. Introduction.....	23
3.1.2. Materials and Methods.....	24
3.1.3. Results and Discussion	28
3.1.4. Conclusions & Future Outlooks	42
4. APPLICATIONS OF CARBON NANOTUBES FOR INCREASED ELECTRODE SURFACE AREA.....	44
4.1. High Surface Area Multi-Walled Carbon Nanotube Electrodes for Photosystem I-Driven Solar Energy Conversion	44
4.1.1. Introduction.....	44
4.1.2. Materials and Methods.....	47
4.1.3. Results and Discussion	48
4.1.4. Conclusions & Future Outlooks	57
4.2. Multiwalled Carbon Nanotube Substrates as Flexible, All-Carbon Electrodes for PSI-Based Biohybrid Devices.....	58
4.2.1. Introduction.....	58
4.2.2. Materials and Methods.....	60
4.2.3. Results & Discussion	63
4.2.4. Conclusions & Future Outlooks	81
5. APPLICATION OF COMMERCIALY AVAILABLE CARBON COMPOSITES IN PHOTOSYSTEM I-BASED ELECTROCHEMICAL CELLS	82
5.1. Utilizing Toray Paper as a High Surface Area Electrode for Photosystem I-Driven Solar Energy Conversion.....	82
5.1.1. Introduction.....	82

5.1.2. Materials and Methods.....	85
5.1.3. Results and Discussion	88
5.1.4. Conclusions & Future Outlooks	101
6. CONCLUSION & FUTURE DIRECTIONS	103
6.1. Summary	103
6.2. Outlook	105
7. REFERENCES	110

List of Figures

Figure 1.1. Representation of the Quantity of Energy Striking the Earth's Surface from the Sun.	2
Figure 1.2. Crystal Structure of Monomeric PSI from <i>Spinacia oleracea</i> .	6
Figure 2.1. Overview of the Photosystem I Extraction Protocol from Baby Spinach.	12
Figure 2.2. Example Cyclic Voltammograms.	19
Figure 2.3. Normalized Cyclic Voltammograms of Common Redox Mediators used in PSI Photoelectrochemical Cells.	20
Figure 2.4. Photochronoamperometry of a PSI Multilayer in the Presence of a Diffusible Mediator.	22
Figure 3.1. Hydrothermal Synthesis of Undoped/Nitrogen-Doped Carbon Dots.	29
Figure 3.2. Transmission Electron Microscopy of Undoped Carbon Dots.	30
Figure 3.3. Absorbance and Fluorescence Spectra of Undoped Carbon Dots.	31
Figure 3.4. Fourier Transform-Infrared Spectroscopy of undoped CDs and 1:2 NCDs.	32
Figure 3.5. Optical Properties of Nitrogen-Doped Carbon Dots as a Function of Doping Ratio.	34
Figure 3.6. X-Ray Photoelectron Spectroscopy of Nitrogen-Doped Carbon Dots.	37
Figure 3.7. Electrochemical Analysis of Undoped and Nitrogen-Doped Carbon Dots.	39
Figure 3.8. Comparison of Peak Current Versus Scan Rate.	41
Figure 3.9. Photovoltage Measurements of PSI-Control and PSI:NCD Mixed Multilayers.	42
Figure 4.1. Ultraviolet-Visible Absorbance and Fourier Transform-Infrared Spectroscopy of Untreated and Acid-Treated Multiwalled Carbon Nanotubes.	49
Figure 4.2. Plot of Capacitive Current Vs. Scan Rate for Treated and Untreated Multiwalled Carbon Nanotube Films.	51
Figure 4.3. Electrochemical Impedance Spectroscopy of MWCNT Layers at Gold Electrodes.	53
Figure 4.4. Photochronoamperometry of PSI on t-MWCNT Composite.	54
Figure 4.5. Composite Steady State Photocurrent Values of PSI on Treated Multiwalled Carbon Nanotubes.	55
Figure 4.6. Percentage of Retained Peak Photocurrent Density as a Function of t-MWCNT Mass.	56
Figure 4.6. Fabrication schematic for BP electrodes using vacuum-assisted filtration.	63
Figure 4.7. Images of Buckypaper Before and After Removal from Filtration Substrates.	65

Figure 4.8. Cyclic Voltammograms of BP electrodes Under Varying Electrolyte Concentration.	66
Figure 4.9. Cyclic Voltammograms of Ferri/Ferro at GCE and BP Electrodes in Different Concentrations of Supporting Electrolyte.....	67
Figure 4.10. Cyclic Voltammograms of Ferri/Ferrocyanide Performed at BP Electrodes Prepared From Different Amounts of MWCNTs.	68
Figure 4.11. Dependence of Increases in ΔE_p with Scan Rate on Analyte Concentration for BP ₆ Electrodes.....	70
Figure 4.12. Electrochemical Impedance Spectroscopy of BP ₆ Electrodes in 0.1 and 1 M KCl. 71	
Figure 4.13. Background Subtracted Cyclic Voltammograms of BP Electrodes in the Presence of RuHex.	74
Figure 4.14. Onset Electropolymerization Potential for PEDOT:PSS and PANi at GCE and BP Electrodes.....	76
Figure 4.15. Photocurrent Densities of PANi and PANi-PSI Films on Glassy Carbon Electrodes.	78
Figure 4.16. SEM Micrographs of Pristine and PANi-Coated BP ₆	79
Figure 4.17. Photocurrent Densities of PANi and PANi-PSI Composites At GCE and BP ₆ Electrodes.....	80
Figure 5.1. Protocol for Oxidative Treatment of Carbon Paper Substrates.....	89
Figure 5.2. Raman Spectra of Untreated CP and FT-CP electrodes.....	90
Figure 5.3. Cyclic Voltammetry of Hexamineruthenium at Carbon Paper Electrodes Subjected to Different Pretreatment Methods.	91
Figure 5.4. Capacitive Cyclic Voltammograms of Carbon Paper Electrodes Following Pretreatment.	92
Figure 5.5. Photochronoamperometry of PSI Multilayers on Flame-Treated Carbon Paper.	93
Figure 5.6. Cyclic Voltammetry of Tested Mediators with PSI on Glassy Carbon Electrodes....	94
Figure 5.7. SEM Micrographs of CP, FT-CP, and FT-CP Following PEDOT:PSS Electropolymerization.	96
Figure 5.8. Photocurrent Densities of PEDOT:PSS-PSI Films on Flame-Treated Carbon Paper.	97
Figure 5.9. Photocurrent Densities of PEDOT:PSS-PSI Composites Fabricated Using Different Electrochemical Conditions.	98

Figure 5.10. Upscaling of PSI-Devices Using Carbon Paper Electrodes.	100
Figure 6.1. Proposed Use of CDs and Doped CDs as Electron and Hole Transport Materials in PSI Photovoltaics.	106
Figure 6.2. Photograph of PAni Growth at FT-CP Electrodes of Different Geometric Dimensions.	108
Figure 6.3. Comparison of Carbon Materials Prepared In Recent Years.	109

List of Tables

Table 3.1. Emissive decay lifetime and quantum yield values (ns) for synthesized NCDs	36
Table 3.2. Measured oxidative peak potentials for CD and NCD samples.....	40
Table 4.1. Deposited MWCNT mass and corresponding electrochemically active surface area enhancement factor	51
Table 4.2. ΔE_p (mV), ψ , and k^0 (cm s^{-1}) for 2mM RuHex in 1 M KCl measured at BP ₆ and BP ₁₂ electrodes at 0.1 V s ⁻¹	74
Table 4.3. ΔE_p (mV), ψ , and k^0 (cm s^{-1}) for 2mM RuHex in 2 M KCl measured at BP ₆ and BP ₁₂ electrodes at 0.1 V s ⁻¹	75
Table 5.1. Charge delivered during PEDOT:PSS electropolymerization.....	95
Table 5.2. Peak currents and total polymerization charges delivered for FT-CP devices assembled to different geometric surface areas.....	100

1. INTRODUCTION

A Growing Need for Renewable Energy

As a global community, mankind has seen consistent increases in annual energy consumption to sustain increasing populations, transportation needs, and advances in technology and manufacturing. As it stands, global energy consumption is predicted to increase nearly 50% by the year 2050, placing higher demands on both renewable and non-renewable sources of energy than ever before.¹ Over-reliance on non-renewable sources such as oil, coal, and natural gas have been the historical response to increases in energy demands; however these sources of energy are known to release harmful pollutants into the environment at an alarming rate and must be supplemented or substituted with greener sources of energy for the sake of the planet.²

Thankfully, a raising awareness towards the negative effects of non-renewable sources has initiated a paradigm shift towards investing in renewable energy. To date roughly 25% of the global energy generated comes from sustainable sources such as wind, hydroelectric, and solar thanks to the collective efforts of countries around the world.¹ Of all the sources of renewable energy generation, solar shows great promise with nearly 5×10^4 exajoules ($1 \text{ EJ} = 1 \times 10^{18} \text{ J}$), or 1.52×10^9 terawatt-hours (TWh), of energy reaching the surface of the earth annually surpassing annual global energy consumption, 1.6×10^5 TWh in 2017, by far (**Figure 1.1**).³ As such, there has been a unified effort across research disciplines to improve our ability to harvest as much of the incident solar energy as possible.

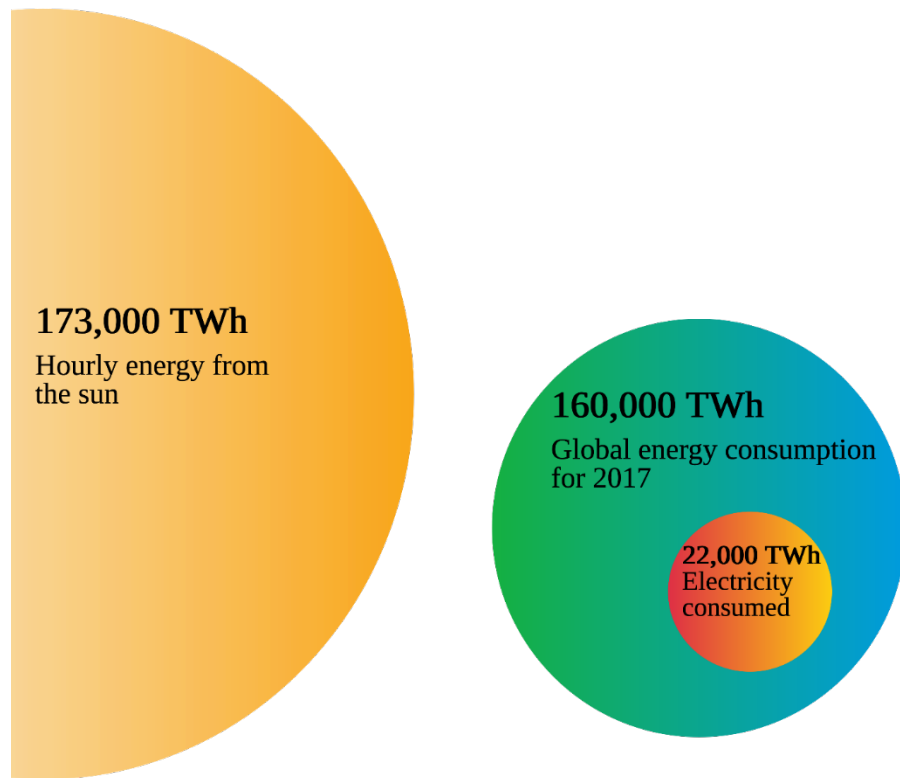


Figure 1.1. Representation of the Quantity of Energy Striking the Earth's Surface from the Sun. The calculated hourly energy from the sun surpasses the total global energy consumption in 2017 showing the immense promise of solar energy. Figure made using biorender.com.

Standard panel solar cells, or photovoltaics, have evolved immensely since their initial invention in 1954.⁴ Photovoltaics operate on the basis of the photoelectric effect, where incandescent energy in the form of photons can be transformed into electrical energy within a material. For photoelectric conversion to occur, certain conditions must be met by the material of interest. First, the selected material for the photovoltaic must absorb light in the visible and near-ultraviolet range, rather than transmitting or reflecting the incoming light.⁵ Materials with discrete energetic gaps between filled and empty molecular orbitals, or semiconductors, and highly absorptive dyes, like anthocyanin, are both capable of absorbing visible or ultraviolet light in this manner. Second, the material must not have alternative processes for using absorbed energy which could outperform photoelectric conversion. Some examples of alternative conversions of photon

energy within materials include photothermal effects (light to heat), photoacoustic (light to sound), or fluorescence (light to light).⁶⁻⁸ Extending beyond a material's interaction with light, photovoltaic devices must also be conductive, provide energetically favorable pathways for excited electrons to travel, and have some manner of creating a sustainable electronic cycle in the presence of continuous light.

At the forefront of commercially available solar cells are those utilizing bulk inorganic semiconducting materials, such as silicon.⁴ Recently, however, advances in semiconducting materials as well as nanoscale science and engineering have led to new material compositions and geometries for solar energy conversion.^{9,10} For one, nanostructured materials benefit from increased surface areas relative to planar substrates, allowing for a higher number of interactions with incident photons.¹¹ Titanium dioxide (TiO₂), for one, has been implemented in devices as thin films, nanoparticle aggregates, and ordered nanopillars in order to implement a range of solar energy conversion strategies.¹²⁻¹⁴ Other nanomaterials which have seen changed the field of solar energy conversion have been quantum dots with tunable optical properties, and perovskite materials, with variable band structures dependent on the chosen anion and cations used in their synthesis.¹⁵⁻¹⁸ Thanks to these materials advances as well as those not mentioned, the diversity in solar cell materials is greater now than ever before with further advances on the horizon.

Alternatives to Inorganic Materials for Solar Energy Conversion

Inorganic materials have progressed the field of solar energy conversion to a state where their viability rivals that of conventional energy sources.¹⁹ That being said, many of the processes needed to refine or fabricate materials at the center of inorganic photovoltaics pose significant environmental and energetic drawbacks.^{20,21} Silicon requires energy demanding refinement in order to reach a quality suitable for use in photovoltaics. Many emerging perovskite materials rely

on rare earth metals, and leave behind solvents and wastes which must be processed accordingly.²²⁻
²⁵ These negative environmental aspects of solar cell fabrication are taken into consideration when conducting life cycle assessments (LCAs) which weigh the environmental benefits of a solar cell against the economic, energetic and environmental costs of the components used in its production.²⁶ LCA calculations point to silicon production as the most energy intensive aspect of the fabrication of silicon-based photovoltaics.²⁷ Perovskite solar cells reduce the energy needed for the fabrication of their photoactive components, but in turn require the use of multiple chemicals and solvents increasing the total waste produced.²⁴ In order to overcome these barriers and progress towards truly sustainable solar cells, more benign assembly methods and environmentally compatible chemicals and materials must be used in place of inorganic components wherever possible.

Inspired by the processing drawbacks to common inorganic solar cell components, research into biocompatible or truly “green” components for solar cells has been of great interest to the renewable energy community.²² These materials, often organic or polymeric in nature, can be substituted for nearly all components in photovoltaics which has led to a range of developed organic-inorganic blended or all-organic photovoltaics over the past few decades.^{28,29} These devices score lower in LCAs than inorganic solar cells while offering benefits unique to all organic photovoltaics such as abundance of materials, biocompatible fabrication processes, and favorable device properties such as flexibility, transparency, and disposability in certain cases.³⁰⁻³²

Pushing the idea of green energy production even further is a growing subclass of organic devices which fully embody the idea of biocompatibility by using materials found in nature as active components for energy harvesting.³³⁻³⁵ These nature-inspired devices, or biohybrid devices, offer pathways to renewable energy with a considerably lower carbon footprint. There are many

ways biohybrid materials can function within a photovoltaic, from dye or pigment molecules found in fruits enhancing the range of absorbed light in TiO₂ cells, to mimicking photosynthetic processes using plant protein complexes on electrode surfaces.^{36,37} Beyond solar energy conversion, there are many ways in which inspiration from nature has led to scientific discovery, particularly in fields of nanoparticles or surface engineering, and can be explored in more depth in many reviews and articles published on the topic.³⁸⁻⁴⁰

Photosystem I-Based Solar Energy Conversion

Of all the classes of biohybrid devices seen in the literature today, none embody the motivation behind this technology as well as energy harvesting schemes based on photosynthetic processes. Photosynthesis has been refined by nature to efficiently convert sunlight into usable chemical energy by plants and phototropic organisms alike, storing on average 4.2×10^{17} kJ annually, nearly four times the total energy consumption for the U.S. in 2019 (1.06×10^{17} kJ).⁴¹ Furthermore, photosynthesis actively removes carbon dioxide from the environment, making it one of the only truly carbon negative energy production processes.³⁴ One of the first instances of artificial photosynthesis was reported by Greenbaum in 1985, which saw Photosystem I (PSI), the primary exciton source for photosynthesis, used for the reductive deposition of platinum particles on the surface of the protein for light-driven hydrogen production.^{42,43} Stemming from this initial use of PSI have been a multitude of devices and designs interfacing the protein with various conducting and semiconducting materials owing to the resilience of the membrane protein complex following removal from its native environment, retaining both its structure and functionality.

It is no surprise that PSI quickly became a strong contender for use in biohybrid energy production as its role in nature, to use incident light to photoexcite an electron nearly 1 V in energy,

directly mimics photodiodes commonly seen in solar cells.⁴⁴ Furthermore, the structure of PSI facilitates rapid generation of an exciton pair, occurring on the order of 10 ns, with high spatial separation of the hole and pair, leading to an internal quantum efficiency of 100% which triumphs over conventional materials (**Figure 1.2**).⁴⁵

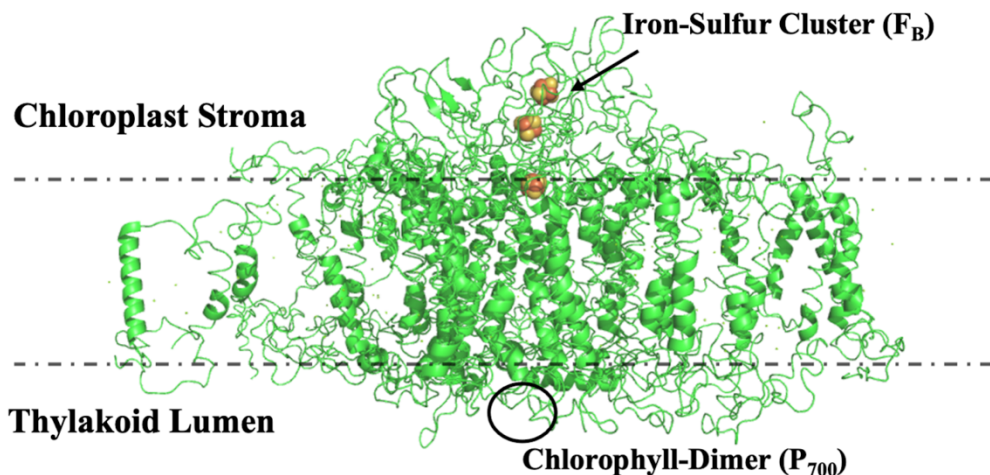


Figure 1.2. Crystal Structure of Monomeric PSI from *Spinacia oleracea*. Structure of photosystem I from *Spinacia oleracea*. Denoted on the structure are the two terminal reaction centers, the special chlorophyll dimer (P₇₀₀) and the iron-sulfur cluster (F_B) where protein reduction and oxidation occur, respectively. The thylakoid membrane is simulated by dashed lines across the transmembrane region of PSI. (Structure taken from PDB: 2WSC)

The high photovoltage and perfect internal efficiency make PSI a promising choice for photovoltaics and mediator-based photoelectrochemical cells, which has led to a wide range of devices of both varieties have been seen throughout the field of biohybrid solar energy conversion.⁴⁶⁻⁵² The challenge with implementing PSI in conventional photovoltaics arises when addressing efficient extraction of charge from the two terminal reaction centers on either face of the protein.^{35,44} On the luminal face, the unique chlorophyll dimer, P₇₀₀, converts light to electrical energy initiating the internal exciton transfer through the protein. The internal charge transfer chain within PSI consists of a series of subunits, primarily quinones and metal-containing centers, before

reaching the terminal iron-sulfur cluster, F_B , on the stromal face of the protein.³⁴ To complete the photo-excitonic cycle *in vivo*, P_{700}^+ and F_B^- are ultimately reduced and oxidized by the metalloproteins plastocyanin and ferredoxin, respectively, facilitating turnover of P_{700} .^{53,54} Once removed from its native environment, PSI must rely on either alternative mediated electron transport (MET) or direct electron transport (DET) to adjacent materials or redox molecules to fill the role of the native components lost when removing the protein from its native environment.⁵⁵ Designing and implementing these materials is one of the leading areas of research regarding PSI-biohybrid devices which simultaneously can boost produced photocurrent densities and photovoltage of fabricated devices.

Additional considerations when designing a PSI-biohybrid device are tied to the host environments of PSI in solar cell devices as well as the environmental impact of fabrication processes.³⁵ The structure of PSI contains both hydrophobic and hydrophilic domains localized to the transmembrane region and the stromal/luminal faces, respectively. Usually a solubilizing material, commonly surfactant, is required to ensure protein solubility throughout aqueous phase deposition techniques.⁵⁶ Once deposited, the intrinsic bulk of the membrane protein prevents substantial denaturing and overall stability regardless of the underlying substrate provided any solution exposure is limited to protein-friendly media. Due to this structural resilience, traditional metal (gold, silver, copper, ITO) or semiconducting (silicon, TiO_2) electrodes have seen ample use in the fabrication of both solid-state and chemically mediated PSI devices.^{48,57-65} Even modified substrates, such as those with structural patterning or chemical modification with components like self-assembled monolayers (SAMs) can host PSI active layers continually inspiring research efforts seen throughout the literature.

An Application for Carbon Materials

To continue improving PSI-biohybrid solar energy conversion, new components to serve as protein scaffolds or electrodes must be found which offer desirable properties (high conductivity, chemical diversity, increased surface area) while remaining biocompatible. One class of underexplored material for applications in PSI-based devices which fit these criteria are allotropes of carbon. As a material, carbon exhibits high biocompatibility, low environmental toxicity, and high conductivity, all of which translate across all carbon allotropes.^{66,67} Examples of allotropes of carbon range from two dimensional planar sheets, or graphene, to more complex structures such as nanotubes, spheres, or fibers depending on the growth or processing conditions. The structural diversity of carbon materials quickly opens the door to different strategies towards implementing into biohybrid device designs.

To date, PSI has seen limited use with allotropes of carbon, restricted to graphene and carbon nanotubes.^{68,69} From past group members, Gunther et al. first interfaced PSI monolayers with graphene deposited on glass as transparent photoanodes capable of generating photocurrent densities up to 550 nA cm^{-2} .⁵⁸ Following this work, more durable graphene oxide layers were implemented for their ability to support multilayers of PSI boosting photocurrent densities to $4 \text{ }\mu\text{A cm}^{-2}$ on glass and $140 \text{ }\mu\text{A cm}^{-2}$ on etched p-doped silicon.^{59,70} While impressive photocurrents were achieved and synergy between carbon surfaces and PSI was demonstrated, efforts were limited to planar graphene flakes and fail to capitalize on the diversity of carbon allotropes.

Research efforts expanding on carbon-PSI systems have since been published, with the most recent efforts, detailed by Morlock et al., focused on 3-dimensional scaffolds of graphene oxide serving as porous substrates for PSI electrochemical cells, capable of generating up to $14 \text{ }\mu\text{A cm}^{-2}$.⁷¹ Additional efforts towards orienting PSI on graphene through the use of coenzymes

such as cytochrome C (cyt C) or chemical tags have also been reported, demonstrating the diverse chemistry available at carbon surfaces.^{72,73} Moving beyond 2-dimensional carbon materials, PSI has also been interfaced with carbon nanotubes, again demonstrating the compatibility between the membrane protein complex and carbon surfaces.^{68,69} Despite their advances, PSI-carbon devices often still rely on inorganic terminal electrodes or support materials, or genetically modified PSI to preferentially bind carbon surfaces, straying from the possibility of an all carbon, truly “green” device.

The work presented in this dissertation seeks to expand upon the use of carbon materials within PSI-biohybrid devices in an effort to progress towards an all-carbon solar cell. In Chapter 2, general materials and methods can be found for the extraction of PSI from whole leaf spinach, quantification of PSI post-extraction, general processes for device fabrication, and guiding protocols for electrochemical tests and analyses critical to testing biohybrid PSI devices. In Chapter 3, the work synthesizing and characterizing small carbon nanoparticles and their prospect as charge transport materials for PSI will be discussed. Chapter 4 will transition to rapid and approachable ways carbon nanotubes can be incorporated into existing PSI devices to enhance the electrode area accessible for PSI loading or used as freestanding flexible electrode substrates. Chapter 5 brings macroscopic carbon materials into the light as inexpensive, highly modifiable electrodes for rapid PSI immobilization leading to biocompatible photoanodes for photocurrent generation or chemical fuel conversion. The accessibility of the bulk carbon electrode and scalability of the techniques used allow for the rapid assembly of devices surpassing typical benchtop dimensions helping fully realize the rapid mobilization of PSI-carbon solar energy conversion. Chapter 6 will conclude this dissertation with remarks on how the ideas and devices

designed and tested in this dissertation can be improved upon to push biohybrid solar energy conversion beyond where it is today.

2. MATERIALS AND METHODS

Chapter 2 contains general materials, methods, and instrumentation used throughout the research discussed in this dissertation. Application specific protocols can be found in the corresponding chapters.

2.1. Extraction of Photosystem I from Whole Leaf Spinach

Throughout all PSI-based research, careful choice of a source organism for the protein is necessary depending on the desired application. In general, the two main sources of PSI seen in the literature today are *Synechococcus elongatus*, a strain of thermophilic cyanobacterium, and whole leaf vegetation such as *Spinacia oleracea*.⁴⁴ PSI from cyanobacterium is often more favorable in applications requiring precise modifications to the protein structure in order to achieve specific binding to target substrates or more invasive access to the terminal F_B and P₇₀₀ reaction centers due to more control over the final structure of the protein complex.⁷⁴ Photosystem I from cyanobacterial strains is also expressed in a trimeric form which offers advantages towards building more dense active layers in devices. Harvesting PSI from whole leaf vegetation, on the other hand, can rapidly yield high quantities of protein from low cost or naturally available source material making it an ideal process for deployable, cost-effective fabrication of biohybrid devices. While multiple classes of leafy green vegetation have been tested as suitable sources for Photosystem I, baby spinach has proven to be a superior source due to the photoelectrochemical performance of its protein as well as the large amount of leafy area per mass further improving its cost effectiveness in terms of the quantity of provided PSI.^{75,76} Photosystem I from *Synechococcus elongatus* has been applied to innovative research in other research groups in the field. This dissertation will focus exclusively on PSI harvested from store bought baby spinach.

The extraction protocol for PSI from whole leaf baby spinach used throughout this dissertation was modified from a previously published method by Reeves and Hall which focused on the extraction of whole thylakoids.⁷⁷ A summative scheme of the extraction protocol, modified from a protocol prepared by Dr. Kody Wolfe, can be found below (**Figure 2.1**).

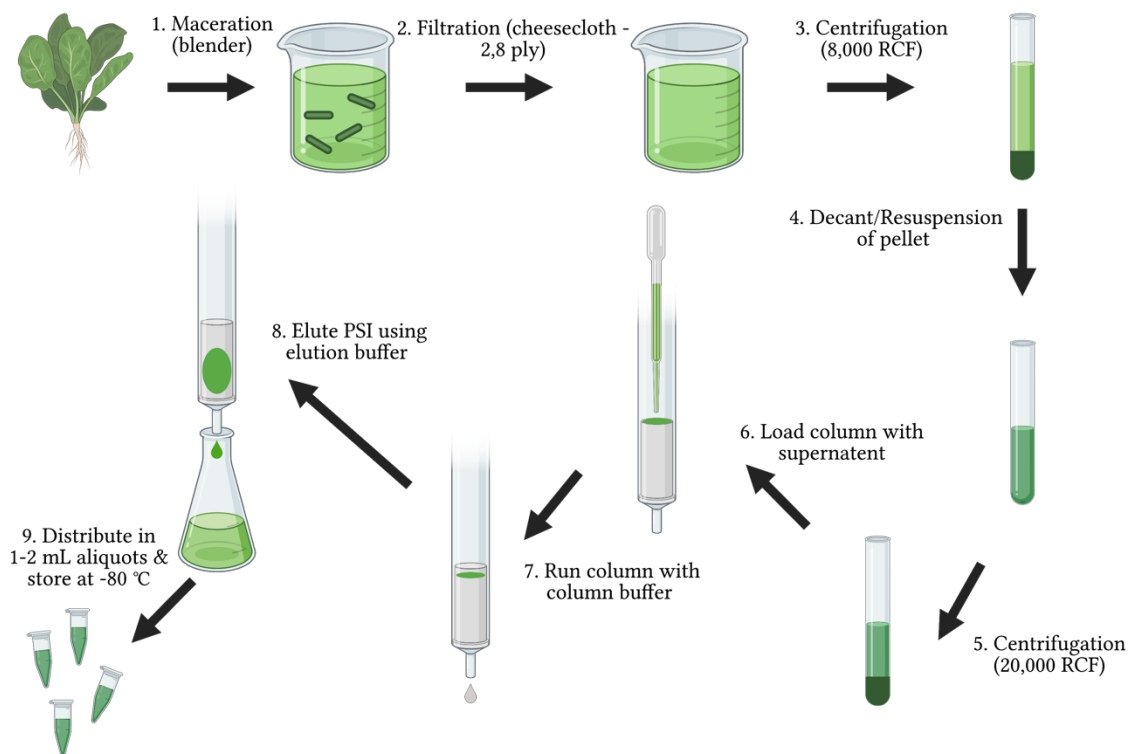


Figure 2.1. Overview of the Photosystem I Extraction Protocol from Baby Spinach. Flowchart of the process for extracting Photosystem I from whole leaf spinach (created with inspiration from an original image made by Dr. Kody Wolfe).

For efficiency and convenience, the solutions and buffers used in the extraction should be prepared the night before and stored at 4 °C, while the spinach is best purchased a day before use to maintain freshness. The solutions needed to complete the extraction are as follows:

1. **Grinding Medium** (~300 mL) consisting of sorbitol (330mM, 18.040 g), sodium pyrophosphate (10 mM, 1.340 g), magnesium chloride (4 mM, 0.240 g), and L-ascorbic acid (2mM, 0.110 g). The grinding medium should be adjusted to pH 6.5 and kept at –

10 °C and slightly thawed prior to use.

2. **Resuspension Buffer** (100 mL) consisting of 2-[4-(2-hydroxyethyl)piperazin-1-yl]ethanesulfonic acid (HEPES) (50mM, 1.192 g), sorbitol (6.012 g), ethylenediaminetetraacetic acid (2mM, 0.058 g), magnesium chloride (1mM, 0.020g), manganese chloride (1mM, 0.020g) and Triton X-100 (1% wt., 1.000g)
3. **Column Buffer** (1 L) consisting of a 20 mM phosphate buffer adjusted to pH 7.0.
4. **Elution Buffer** (1 L) consisting of a 200 mM phosphate buffer adjusted to pH 7.0 and containing Triton X-100 (0.05% wt., 0.500 g) to assist in liberating and stabilizing PSI following the extraction.

On the morning of the extraction, 100 g of spinach is washed and deveined, collecting the leaves while discarding the stems and any large veins easily removed. Once the desired mass of spinach is obtained, the leaves are added to a common household blender along with roughly half of the partially thawed (such that it has the consistency of slush) grinding medium. The spinach leaves and grinding medium should be pulsed until mostly homogenized.

Following maceration, the cell walls of the plant cells are lysed and the whole thylakoid stacks are free in solution. The homogenized solution is then filtered through cheesecloth, first through a two-ply cut of cheesecloth followed by an eight-ply cut of cheesecloth. Through this process the leaf material is removed from the thylakoid-containing solution. The filtered solution is then subjected to centrifugation to remove the thylakoids from solution. Centrifugation should be conducted with care, making sure to chill the chamber to 4 °C and using vessels of similar mass with differences no greater than 5 mg, or to the specifications of the used instrument. Once the proper conditions have been met, the thylakoid-containing solutions can be centrifuged at 8,000 RCF for 1 minute. Following centrifugation, the thylakoids form a condensed pellet visible on the

bottom of the centrifuge tube. Discard the supernatant and keep the thylakoid pellet.

The next step of the extraction is to collect the pellets in resuspension buffer while simultaneously lysing the thylakoid membrane, isolating PSI for future collection. In this extraction protocol, Triton X-100 is used as a surfactant to both lyse thylakoid membranes while solubilizing PSI due to its proven compatibility with the protein. Other surfactants could be substituted for Triton X-100 and studies have been conducted on their impact on PSI activity and are worth investigating.^{78,79} To the thylakoid pellets, add a few drops (1-2 mL) of resuspension buffer and vortex to free the content of the pellet from the bottom of the tube. Then combine the pellet-containing solutions of each centrifuge tube into a single vial to be centrifuged a second time. It is important to minimize the volume of resuspension buffer used during this step as this will assist in concentrating the final aliquots of PSI. The second centrifugation should be conducted at 20,000 RCF for 15 minutes. Following this centrifugation step, PSI, along with other thylakoid proteins as well as organelles previously contained by the membrane, will be suspended in solution due to the high concentration of surfactant while the remains of the lipid membrane precipitate out of solution. Keep the supernatant (suspended protein solution) and discard the remaining pellet.

Once PSI has been isolated from the thylakoid membrane it then needs to be separated from other proteins and organelles. To do this, a hydroxyapatite column is used to electrostatically attract PSI over other solubilized species. Prior to assembling the column, the target amount of fast-flow hydroxyapatite (15 g) should first be washed and activated with column buffer prior to pouring the resin in a column fit with a water jacket for temperature control. Once the resin has been packed, the supernatant containing PSI can be loaded onto the column and flushed with column buffer. While running a steady flow of column buffer through the hydroxyapatite, the eluant will slowly turn green, indicating the elution of non-PSI proteins and structures, such as

chlorophyll, while a discrete dark green band should persist on the column, containing the desired PSI.

After all non-PSI moieties have been eluted from the column, elution buffer should be used exclusively to elute and store PSI. After swapping to elution buffer, continue to run the column until the eluant becomes solid green in color, at which point the solution should be collected in a clean vessel. The volume of collected green eluant will control the final concentration of the PSI aliquots from the extraction, as a larger volume will decrease the final concentration of the extracted protein. Once the target volume has been reached (roughly 80 – 100 mL/100g of spinach) proceed to distribute the collected eluant into the desired volume aliquots and store at -80 °C.

2.2. Quantification of Extracted PSI

The concentration of PSI in the isolated aliquots can be determined spectroscopically following a method first reported by Baba et al.⁸⁰ This procedure measures the difference in absorbance of two PSI solutions of equal concentration following simultaneous oxidation and reduction. The absorbance at 725 nm can then be used to measure the concentration of P₇₀₀ reaction centers, and consequentially PSI protein. In short, first prepare the following solutions immediately prior to use (the oxidizing and reducing solutions readily hydrolyze and as such these solutions should be prepared fresh for each quantification experiment):

1. **Baba's Assay Buffer** (100 mL) consisting of tricine (50 mM, 0.896 g), sorbitol (100 mM, 1.822 g), sodium chloride (10 mM, 0.059 g), and Triton X-100 (5% wt., 0.050 g).
2. **Oxidizing Solution** (10 mL) consisting of ferricyanide (1 M, 3.293 g).
3. **Reducing solution** (1 mL) consisting of sodium ascorbate (500 mM, 0.099 g) and dithiothreitol (5 mM, 0.001 g).

Once the required solutions are prepared, retrieve a frozen aliquot of PSI and allow it to thaw. Meanwhile the UV-vis spectrometer can be powered on and set to scan between 650 and 750 nm. When the PSI aliquot has thawed, prepare two cuvettes with 2275 μL of Baba's assay buffer and 100 μL of undialyzed PSI. Scan both cuvettes and save the resulting spectra as background scans for the respective cuvettes. Then, to one cuvette add 120 μL of DI- H_2O and 5 μL of reducing solution and invert to mix. To the other cuvette, add 125 μL of the oxidizing solution and invert to mix. Allow both cuvettes to react for 15 min prior to measuring the absorbances a second time. Subtract the baselines from their respective reaction spectra and then subtract the reduction spectra from the oxidation spectra. In the final absorbance plot, the value obtained from subtracting the absorbance at 725 nm from the peak absorbance point can be used in the following equation to determine the PSI concentration in the initial aliquot:

$$C_{PSI,aliquot} (mM) = \frac{A}{64 (mM^{-1}cm^{-1}) \times L (cm)} \times \frac{V_{total,cuvette}}{V_{PSI,cuvette}} \quad \text{Equation 2.1}$$

where $V_{total,cuvette}$ is the volume contained in the cuvette (2500 μL if following this procedure), $V_{PSI,cuvette}$ is the volume of undialyzed PSI added to the cuvette (100 μL if following this procedure), and L is the path length of the cuvette used. In most cases the path length of the cuvette will be 1 cm. Using this procedure, the concentration of PSI per extraction batch can be known allowing for normalization of devices to the quantity of deposited PSI in most scenarios.

2.3. Assembly of Photosystem I Films/Composites for Solar Energy Conversion

Once isolated PSI has been acquired, the resulting solution can be used to prepare bioelectrodes through one of many deposition processes, discussed in this dissertation as well as in the many research articles published on the topic.^{44,81-83} In most cases, the PSI solution must first be purified of excess surfactant, salts, and small biological molecules and structures not

removed through the hydroxyapatite column. To achieve this, PSI aliquots are typically subjected to dialysis prior to use. Dialysis works by manipulating the diffusion rates of different species through a semi-permeable membrane chosen to selectively allow species below a specific molecular cut-off weight (MCOW) to pass through the membrane, leaving the initial solution, or retentate, consisting of species too large for diffusion through the tubing. For PSI extract, a 3.5 kilodalton (kDa) MCOW is chosen to allow low molecular weight species such as surfactant, salts, and small biological molecules and proteins to leave the PSI solution preventing their interference with future device fabrication and performance. It should be noted that once dialyzed, the solubility of PSI in aqueous solutions diminishes immensely and it is recommended that the dialyzed solution be used immediately.

Once PSI has been dialyzed (overnight or 12 -16 hours), it is then ready for deposition onto suitable electrode substrates. One common method for depositing dialyzed PSI onto electrode surfaces is vacuum-assisted evaporation which can easily assemble dense multilayers of PSI protein on flat, hydrophilic electrode materials. It is recommended that substrates first be cleaned adequately, either by sonication in suitable solvent baths or through more extreme methods (i.e. treatment with piranha acid or hydrofluoric acid) to remove any contaminants prior to PSI deposition. Common substrates to be used with vacuum-assisted evaporation include glassy carbon electrodes, gold wafers, silicon wafers, and toray paper, all of which should be cut to reasonable dimensions (1.2 cm x 2.5 cm) and masked with inert electrochemical masking tape to control the coated surface area (unless otherwise specified substrates were masked leaving an exposed surface area of 0.71 cm²)

The density of the formed film can be controlled by adjusting the deposition volume, number of additions, and in some cases PSI concentration to build multilayers of thicknesses

extending into the hundreds of nanometer range.^{84,85} The protein multilayer films are then suitable for light-to-energy conversion in the presence of chemical mediators for photoelectrochemical cells or as a photoactive layer in a bulk-heterojunction photovoltaic when sandwiched between appropriate materials.^{46,48} Techniques increasing the active surface area of the chosen substrate can enhance mediator-based devices assembled using vacuum assisted evaporation by increasing the ratio of surface area to protein which can lead to enhanced mediator conversion rates.^{46,63}

2.4. Electrochemical Techniques and Analyses

Electrochemistry plays a critical role in all aspects of PSI biohybrid device design, from designing devices to testing their efficacy. This section will contain a brief overview of the fundamental processes and experiments key to developing PSI based devices as used in this dissertation. Experimentally, solutions of sufficiently high supporting electrolyte concentration (0.1 M for planar electrodes and 1.0 M for high surface area carbon materials) should be used alongside the species of interest, typically diffusible redox molecules such as ferri/ferrocyanide or hexamine ruthenium (RuHex). Potassium chloride (KCl) is a widely used mediator for aqueous systems, though other small molecule salts can also be employed depending on the application or solvent. All the techniques listed here are described for applications in three electrode electrochemical cells, with platinum mesh substrates acting as counter electrodes and silver/silver chloride (1M) reference electrodes unless otherwise noted. For a more in-depth overview of electrochemistry fundamentals and practices, outside references or textbooks on the topic should be consulted.⁸⁶

2.4.1. Cyclic Voltammetry

Cyclic voltammetry is a powerful diagnostic tool in determining electrochemical properties pertaining to both electrode materials and diffusible species in solution. At its core, cyclic

voltammetry is a potential sweep method in which the potential of the working electrode is cycled between two set values, measuring current as a function of working potential.

Typical current output falls under one of two categories: non-faradaic and faradaic current. Non-faradaic current represents background charging processes tied to the electrode surface, making it useful when investigating the capacitive behavior of the system in question as seen in chapters 4 and 5. Faradaic current, or a rapid increase in current over the baseline value, occurs when heterogeneous electron transfers occur between the working electrode and a secondary species at the electrode surface as seen in chapter 3. Both non-faradaic and faradaic current can be seen in nearly all cyclic voltammograms, commonly referred to as “duck-like” for the distinct shape seen in the current output. (**Figure 2.2**) From these voltammograms, system parameters such as surface area or overpotentials can be determined through interpretation of the resulting data.

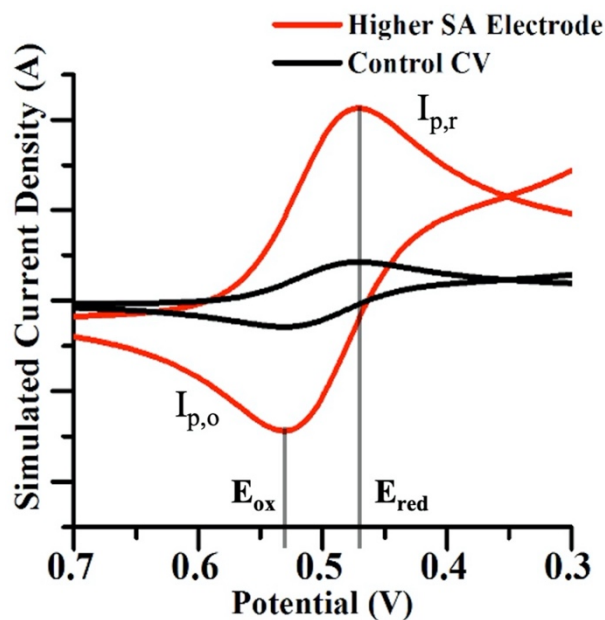


Figure 2.2. Example Cyclic Voltammograms. Simulated cyclic voltammograms of a reversible redox probe at electrodes of different surface areas. Denoted values include reductive peak current ($I_{p,r}$), oxidative peak current ($I_{p,o}$), oxidation peak potential (E_{ox}), and reduction peak potential (E_{red}).

Pertaining to PSI biohybrid devices, cyclic voltammetry is most useful for characterizing the oxidation and reduction potentials of mediator candidates or for characterizing electrodes to be used in devices. By determining the oxidation (E_{ox}), reduction (E_{red}), and half-reaction potential ($E_{1/2}$ – midpoint potential between E_{ox} and E_{red}) of a diffusible species in solution, its viability as a reducing or oxidizing agent for either P_{700}^+ or F_B^- can be evaluated based on the proximity of the respective potentials to the established values for either protein reaction center (**Figure 2.3**).⁶⁵

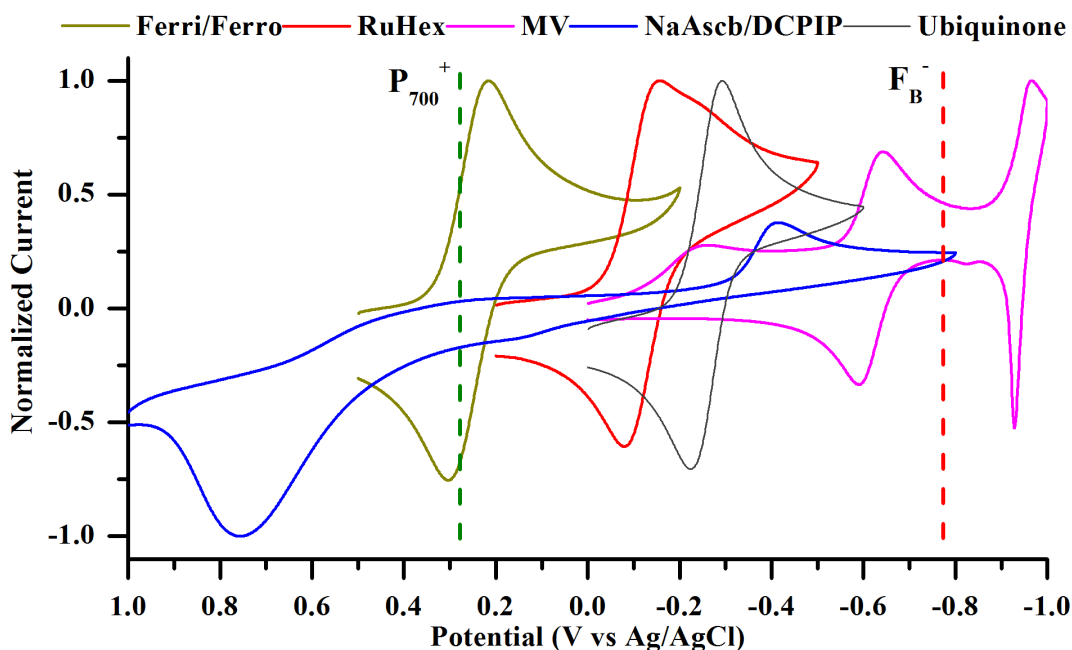


Figure 2.3. Normalized Cyclic Voltammograms of Common Redox Mediators used in PSI Photoelectrochemical Cells. The cyclic voltammetry responses for common mediators used with PSI, ferricyanide/ferrocyanide (Ferri/Ferro) – hexamine ruthenium (RuHex) – methyl viologen (MV) – sodium ascorbate/2,6-dichlorophenolindophenol (NaAscb/DCPIP) - 2,3-dimethoxy-5-methyl-p-benzoquinone (Ubi), at a gold disk working electrode are shown above. Also denoted are the agreed formal potentials for the reduction of P_{700}^+ (green dashed line) and F_B^- (red dashed line).

Alternatively, when designing porous or three-dimensional electrodes, changes in the magnitude of either peak faradaic ($I_{p,o/r}$) or non-faradaic current can be used to compare the electrochemically active surface areas of different electrodes offering unique advantages over their planar counterparts (**Figure 2.2**). The application of cyclic voltammetry extends beyond the

applications discussed here and additional references can offer more insight to the full capabilities of the technique.⁸⁷⁻⁸⁹

2.4.2. Photochronoamperometry

The critical metric of interest when optimizing PSI-based biohybrid devices is the photocurrent density, or light-driven current production, of the system at hand. To measure the photocurrent of PSI biohybrid devices, chronoamperometry is used to measure current versus time responses (known as i-t curves) of bioelectrodes held at a constant working potential. The act of testing a PSI device can be modeled as a potential step experiment initiated by the photoexcitation of electrons within the protein complex. To determine the generated photocurrent at a PSI-modified electrode, typically the difference between the current produced in the light versus the current produced in the dark is measured and reported as a photocurrent density (j , $A\ cm^{-2}$), or current normalized to the geometric area of the device. PSI i-t curves are commonly measured at the measured open-circuit potential (OCP) as to not apply electrochemical bias to the system which can influence the observed photo-response. Under normal mediated electron transfer in photoelectrochemical cells, the typical light-driven response of a PSI device can be well characterized by Cottrellian behavior modeled by Equation 2.2:

$$i_d(t) = \frac{nFAD_O^{1/2}C_O^*}{(\pi t)^{1/2}} \quad \text{Equation 2.2}$$

In the above equation, t is the elapsed time following the potential step (s), n is the number of transferred electrons, A is the area of the electrode (cm^2), D is the diffusion coefficient of the redox probe ($cm^2\ s^{-1}$), and C is the concentration of the redox molecule in solution ($mol\ cm^{-3}$). As such, the current profile observed in a potential step experiment resembles that shown below (**Figure 2.4**)

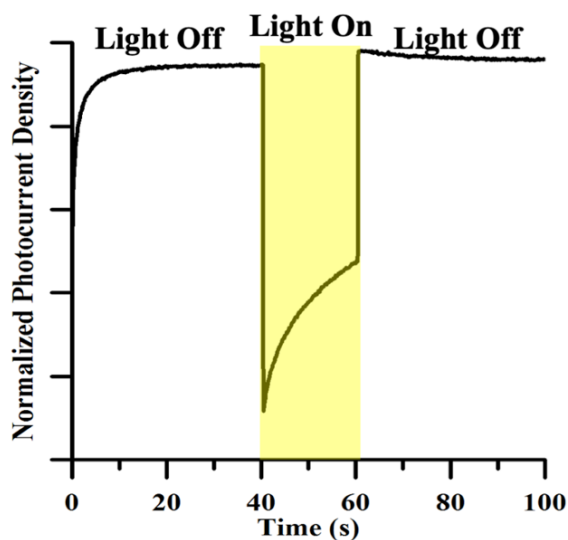


Figure 2.4. Photochronoamperometry of a PSI Multilayer in the Presence of a Diffusible Mediator. Typical current versus time response for a PSI multilayer at a conducting working electrode in the presence of a diffusible mediator. Upon illumination, the PSI photoelectrochemical cells behave as a potential step system due to excess generation of either oxidized or reduced species at the electrode surface.

The large current spike upon illumination of PSI devices confirms a sudden increase in the potential at the working electrode due to the photoexcitation of electrons to higher energy states confined in the F_B reaction center. Following the initial conversion of mediator at the bioelectrode surface, the current density quickly decays to a steady-state value reflecting limitation due to diffusion of fresh mediator to the relevant PSI reaction centers. The direction of the current (positive for cathodic behavior; negative for anodic behavior) is dependent on the direction of the net flow of current through the device, which is dictated by a build-up of either oxidized (O) or reduced (R) mediator species at the PSI-modified electrode. Whether a mediator will be oxidized or reduced by PSI is dependent on thermodynamic driving force dictated by a difference between the $E_{1/2}$ of the molecule and the formal potential of the P_{700}^+ and F_B^- reaction center (**Figure 2.3**). The directionality of the net current can also be influenced by the fermi level or redox potentials of supporting electrode materials, such as hole or electron transport layers, which is often the case for solid-state PSI devices.^{48,90}

3. DESIGN OF CARBON NANOPARTICLES FOR ENHANCED ELECTRON TRANSFER WITH PHOTOSYSTEM I

Chapter 3 dives into the synthesis and characterization of small carbon-based nanoparticles, or carbon dots, as potential materials for the transport of charge to and from the PSI reaction centers. This research was conducted with the help of Sophia Click who provided expertise with many of the time-resolved optical measurements of the produced materials. Special thanks are given to Dr. Kody Wolfe and Dr. Dilek Dervishogullari who helped with the preparation of this manuscript.

3.1 Optical and Electrochemical Tuning of Hydrothermally Synthesized Nitrogen-Doped Carbon Dots^a

3.1.1. Introduction

Carbon dots (CDs) are an emerging class of carbon-based nanomaterial rapidly gaining interest due to their optical and electrochemical properties while maintaining low biological and environmental toxicity.⁹¹ CD materials, first identified in 2004 as fluorescent byproducts of a carbon nanotube synthesis, have been implemented as substitutes for metallic nanoparticles and quantum dots in applications ranging from bioimaging and drug delivery to energy harvesting and fuel production.⁹²⁻⁹⁷ Within energy harvesting applications, CDs have been shown to work as photocatalytic particles, charge transport materials, or fluorescent light emitters.⁹⁸⁻¹⁰⁰ The widespread use of CDs has been attributed to their facile syntheses, wide doping capabilities, and

^a Portions of this chapter are taken in part from C. D. Stachurski, S. M. Click, K. D. Wolfe, D. Dervishogullari, S. J. Rosenthal, G. K. Jennings, D. E. Cliffler. Optical and Electrochemical Tuning of Hydrothermally Synthesized Nitrogen-Doped Carbon Dots, *Nanoscale Adv*, **2020**, 2, 3375-3383.

multiple post synthesis surface functionalization strategies leading to a diverse range of materials, each suited for their intended purpose.

Carbon dots have been synthesized from both top-down and bottom-up synthetic pathways; however bottom-up approaches have produced more controlled and tunable products. Although top-down techniques are more effective at bulk conversion of macroscopic waste materials into usable CDs, they often produce polydisperse particles exhibiting broad emission spectra and non-uniform doping concentrations per CD.^{101,102} In general, bottom-up approaches, such as microwave-assisted pyrolysis or hydrothermal carbonization of a molecular precursor, provide more control over the produced nanomaterial leading to small, monodisperse particles with surfaces and compositions resembling the physical and chemical structure of the used starting materials.¹⁰³⁻¹⁰⁵

In addition to producing more uniform particles, bottom-up synthetic methods also provide control over CD doping by selective inclusion of additional molecular precursors in the reaction mixture rather than relying on heterogenous elemental compositions of bulk materials or biomass, as is often the case in top-down techniques.^{106,107} To this end, hydrothermally synthesized nitrogen-doped carbon dots (NCDs) have become prevalent in the field due to their enhanced emissive properties originating from new electronic states created by electron-rich nitrogen groups.^{107,108} Bottom-up CD or NCD syntheses typically follow similar workflows regardless of the technique: a molecular carbon source such as sucrose, citric acid, or primary alcohols is dissolved alongside any desired dopant or alkaline agent and reacted to facilitate carbon dot growth.^{109,110} These conditions are believed to initiate polymerization of the carbon source into sheets that then grow into three dimensional particles.¹¹¹

CDs and NCDs have seen use in a number of fields thanks to steady fluorescence, excellent electrical conductivity, and efficient electron transfer, with unique properties such as photoluminescence intensity and wavelength showing tunability depending on the chosen synthetic route and chosen molecular precursors.^{110,112-118} CD-based sensors synthesized from citric acid improve detection of biological analytes such as dopamine or environmental contaminants such as bisphenol A when compared to unmodified glassy carbon electrodes.¹¹⁹ Similar CDs synthesized with citrate as a carbon source and urea as a nitrogen dopant have also been used as fluorescence-based sensor for Hg^{2+} .¹²⁰ By using different molecular precursors such as 1,2,4-triaminobenzene, Jiang et al. demonstrated how a similar hydrothermal process could yield new, yellow NCDs selective for the detection of Ag^+ ions.¹²¹

Electrochemical properties of CDs and NCDs, such as band gap and oxidation/reduction potentials, have also been shown to exhibit tunability dependent upon synthetic conditions, although to a lesser extent than optical properties, leading to their incorporation in a number of different energy harvesting or photocatalytic applications.^{122,123} Rigodanza et al. demonstrated that by adding various commercially available quinones into a novel microwave treatment of arginine and ethylenediamine, the oxidation and reduction potentials of produced CD materials could be tuned to energetically match different systems.¹⁰⁵ Wang et al. showed tunable electrochemiluminescence properties in nitrogen doped CDs upon changing the concentration of ammonium hydroxide used in the synthesis, however no direct measurement of oxidation potential is reported.¹²⁴ Peng et al. reported shift in oxidation and reduction potential of nitrogen-doped CDs as a result of both changing the identity of the carbon and dopant source as well as pH of the electrolyte solution, but the impact of molar ratio of dopant to carbon source was not investigated.¹²⁵ Moving beyond synthetic parameters, Privitera et al. demonstrated how post-

synthesis surface modification of nitrogen-doped carbon dots with thiophene groups shifted oxidation potentials to more negative potentials, yet additional reactions may detract from favorable cost or environmental properties of CDs depending on the selected ligands.¹²⁶

While the impact of the identity of carbon and dopant sources have been well studied across CD research over the years, the effects of dopant concentration on intrinsic CD properties has not had much attention.^{127,128} Few articles report a dependence of optical properties on dopant concentration during CD formation, and even less attention has been given towards its impact on electrochemical properties.¹²⁹⁻¹³¹ Considering the widespread use of CDs and doped CDs in energy harvesting applications, this study seeks to identify the impact of dopant concentration on optical and electrochemical properties, specifically oxidation and reduction potential, as a way to design CD materials better suited for specific sensing and energy harvesting applications.

3.1.2. Materials and Methods

Materials

All chemicals were used as purchased from the supplier without further modification. Sodium citrate dibasic (Sigma Aldrich, St. Louis, MO) and tribasic (Fisher Chemical, Loughborough, UK) were used to create an aqueous citrate buffer (0.67 M) held at pH 6.2 which was used as the hydrothermal reaction solution of all CD syntheses. Urea (Sigma Aldrich) was used as a nitrogen dopant for select batches of CDs. Potassium chloride (Fisher Chemical) was used to make all electrolyte solutions for electrochemical measurements. All water used was deionized H₂O (DI-H₂O) (18 M Ω -cm) obtained from an in-house purification system (Barnstead Nanopure, Thermo Scientific, Waltham, MA). Dialysis was performed using a 1 kDa molecular weight cutoff membrane for 18 h to remove unreacted starting material (Repligen, Boston, MA).

Lyophilization of the retentate was performed at 0.021 mBar and -83 °C (FreeZone 4.5 Plus, Labconco, Kansas City, MO).

Undoped Carbon Dot Synthesis

CDs were synthesized via a hydrothermal synthetic method using a premade citrate buffer. Briefly, 15 mL of a 0.67 M solution of citrate buffer (10 mmol) held at pH 6.2 were added to an autoclave (Teflon, steel jacket, 43 mL, Parr Instrument Company, Moline, IL). To synthesize the CDs, the citrate buffer was heated to 200°C for 4 h then cooled to room temperature. After CD synthesis, the then yellow solution was dialyzed (1 kDa cutoff membrane, Spectrum, New Brunswick, NJ) against DI-H₂O for 18 h. The CDs were lyophilized and re-dissolved in DI-H₂O to the desired concentration of (mg/ml).

Nitrogen-Doped Carbon Dot Synthesis

To synthesize NCDs, urea was chosen as a nitrogen source due to its widespread use in similar doped CD syntheses. For all NCD syntheses, urea was dissolved at varying molar ratios (hereafter denoted as moles of urea:moles of citrate; i.e. “1:2” denoting 5 mmol of urea added to 10 mmol citrate) in 10 mL of 0.67 M citrate buffer. Once dissolved, the solution was heated to 200°C for 4 h then cooled to room temperature with fan-assisted air flow. After NCD synthesis, the yellow solution was dialyzed, lyophilized, and dissolved in DI-H₂O to the desired concentration (mg/ml). A complete list of synthesized particles can be found in table S.T1

CD and NCD Characterization

To determine the absorbance spectrum of CDs and NCDs, spectrophotometric measurements were taken. CDs and NCDs were dissolved in water to 2-2.5 mg/mL and 1 mL was added to a quartz cuvette and loaded into a Cary 5000-Bio UV-Vis spectrometer.

Fluorescence measurements of CDs and NCDs were made on a Cary Eclipse fluorescence spectrophotometer. Time-resolved photoluminescence (PL) measurements were performed with solutions dispersed on glass slides (Fisher Scientific, Pittsburgh, PA) using a custom-built epifluorescence microscope following Orfield et al. as modified from Dukes et al.^{132,133} Samples were excited under wide-field illumination using a 405 nm PicoQuant pulsed diode laser with a repetition rate of 2.5 MHz. The beam was reflected with a 420 nm long pass (LP) dichroic filter (Omega Optics, 3RD420LP) into an inverted objective (Olympus UPLSAPO, apochromatic, water immersion, 1.2 N.A., 60×) and brought into focus at the sample. Fluorescence from the focal region was collected by the same objective, passed through the dichroic filter, further filtered by a 450 nm LP dichroic filter, and focused through a 150 μm aperture onto a single-photon avalanche photodiode (SPAD, Micro Photon Devices PD-050-0TC). A time-correlated single photon-counting unit (TCSPC, PicoHarp 300, ~35 ps) was used to generate a histogram of photon arrival times. The obtained PL decay curves were fitted using a multi exponential function:

$$\mathbf{I(t)} = \mathbf{A_1 e^{\frac{-t}{\tau_1}} + A_2 e^{\frac{-t}{\tau_2}} + A_3 e^{\frac{-t}{\tau_3}}} \quad \text{Equation 3.1}$$

where the fit parameters τ_i and A_i are the PL decay time and amplitudes, respectively. The amplitude-weighted average decay time, τ_{avg} , was calculated to approximate the radiative lifetime component, τ_r , and with the ensemble quantum yield, QY , used to calculate the non-radiative lifetime component, τ_{nr} , such that:

$$QY = \frac{\tau_r}{\tau_r + \tau_{\text{nr}}} \quad \text{Equation 3.2}$$

PL spectra were collected on an ISS PC1 photon counting spectrofluorometer using a 300 W Xe arc lamp as the excitation source. PL was measured with a 1 s integration time and a 1 mm slit width. Quantum yield (QY) measurements were determined by comparing the PL of the CD samples to that of a reference dye (Coumarin 152A in hexanes, QY ~ 100%). All samples and dyes

used were diluted in their respective solvents so that their optical densities (OD) at the excitation wavelength were less than 0.1.

Infrared spectroscopy measurements of solid CD and NCD samples were made on a Nicolet iS 5 FTIR spectrometer using an ATR-IR crystal attachment for solid sample analysis.

High resolution transmission electron microscopy (TEM) was performed on a FEI Tecnai Osiris 200 keV transmission electron microscope. CDs and NCDs were deposited onto lacy carbon-coated copper grids (Ted Pella, Redding, CA) by dip-coating grids in a 2.5 mg/ml solution and air-drying overnight.

X-ray photoelectron spectroscopy (XPS) analyses were performed using an Ulvac-PHI Versaprobe 5000. Solutions of the particles were drop cast onto pieces of a silicon wafer, which were then mounted onto a sample holder using BeCu clips. A 100 μm diameter monochromatic Al K α x-ray (1486 eV) beam rastered over an approximately 800 μm by 400 μm area and a takeoff angle of 45 degrees off sample normal were used in each acquisition. Pass energies of 187.7 eV and 23.5 eV were used for the survey and high-resolution acquisitions, respectively. Charge neutralization was accomplished using 1.1 eV electrons and 10 eV Ar⁺ ions. Binding energies were calibrated by setting the peak corresponding to -CH₂- type bonding in the high-resolution carbon 1s spectrum acquired from each sample to 284.8 eV.

Electrochemical characterization was performed on a CHI-660a electrochemical workstation using a three-electrode setup in a 25 ml 3-neck round bottom flask. A 3 mm glassy carbon disk electrode (CH instruments, Austin, TX) was used as the working electrode, a homemade platinum mesh was used as the counter electrode, and a 3 M Ag/AgCl electrode (CH instruments) was used as the reference electrode. The electrolyte solution used for each measurement consisted of 100 mM KCl. Prior to each measurement, the glassy carbon electrode

was cleaned by hand-polishing using a polishing wheel with 0.05 μm alumina MicroPolish (Buehler, LTD, Lake Bluff, IL), then sonicating for 15 s in distilled water, and finally drying with a stream of nitrogen gas. The platinum counter electrode was flame polished on an open flame prior to each run.

For all electrochemical measurements, approximately 20 ml of aqueous 100 mM KCl electrolyte solution was deoxygenated with nitrogen for 15-20 min. The glassy carbon working electrode was conditioned in deoxygenated electrolyte solution using a 100-cycle cyclic voltammetry experiment between 1.0 V and -1.0 V at a scan rate of 200 mV/s. Background cyclic voltammograms were recorded prior to the addition of purified CD solutions at scan rates of 50, 100, 200, and 300 mV/s and used for background subtraction when specified. Cyclic voltammograms were recorded by scanning in the negative direction followed by a positive potential sweep using the potential window and scan rate denoted per figure. Linear sweep voltammetry followed the same general experimental workflow.

3.1.3. Results and Discussion

CD and NCD Synthesis and Characterization

CDs and NCDs were produced using a hydrothermal, bottom-up synthesis capable of tuning the electrochemical properties by varying the doping quantities in the reaction solution. The doping quantities were, in turn, controlled by varying the concentration of heteroatoms present in the reaction mixture through the addition of urea to the citrate buffer.^{96,101} This synthesis was adapted from Qu et al. who reported the successful synthesis of CDs and NCDs by the hydrothermally reacting aqueous citric acid solution containing either an excess of base (sodium hydroxide) or alkaline dopant (urea, ethylenediamine, or diethyl amine).¹¹¹ Presumably, in this synthesis the increase in pH from the addition of base or alkaline dopant facilitated the dehydration and polymerization reactions between citrate ions, a critical step in the citrate-based CD formation

mechanism. In our modified synthetic scheme, the pH is increased by buffer rather than dopant (**Figure 3.1**). By decoupling the role of the base and the dopant, lower ratios of dopant could be added to the reaction mixture without impeding solution conditions necessary for CD or NCD formation.

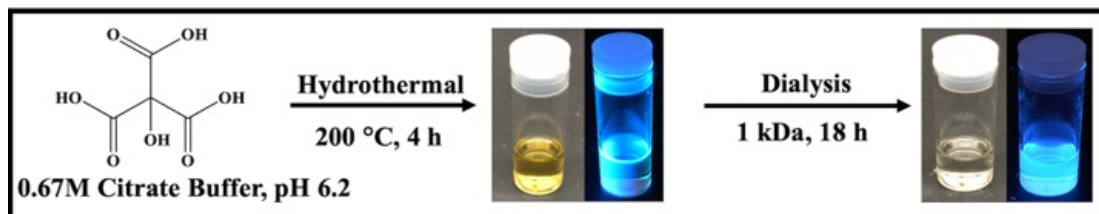


Figure 3.1. Hydrothermal Synthesis of Undoped/Nitrogen-Doped Carbon Dots. Representation of the CD synthetic scheme. For NCD synthesis, varying amount of urea (denoted as moles urea:citrate) was dissolved in the citrate buffer prior to hydrothermal treatment. Photographs of NCDs under ambient and UV (365 nm) light.

The resulting CDs or NCDs products were first subjected to purification via dialysis. Before and after purification, CDs and NCDs exhibit a yellow and pale-yellow color, respectively, with higher doping ratios leading to visibly darker solutions. The need for purification was also apparent in obstructed TEM images and broad absorbance spectra of undialyzed product emphasizing the need for purification of these materials prior to use. All products were therefore subjected to purification via dialysis with a 1 kDa cutoff membrane prior to lyophilization to remove unwanted byproducts.

Following purification, the size, crystallinity, and polydispersity of synthesized CDs were investigated to assess the quality of the formed material. Changes in the doping ratio did not impact the size distribution of the produced NCDs indicating that the citrate molecules were responsible for the majority of the CD or NCD composition. Following a 4 h synthesis, the produced CDs (**Figure 3.2A**) and NCDs (**Figure 3.2D**) exhibited diameters of 2.5 ± 0.3 nm and 3.0 ± 0.5 nm, respectively, with both amorphous and crystalline particles present (**Figure 3.2B**).

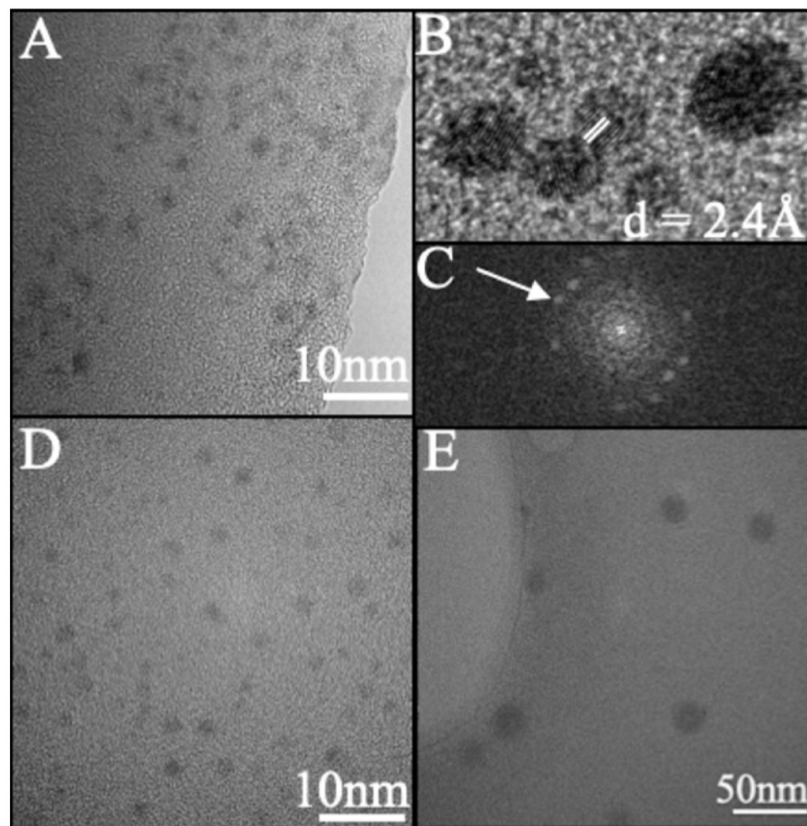


Figure 3.2. Transmission Electron Microscopy of Undoped Carbon Dots. Representative TEM image of (A) undoped CDs, 4 h reaction time (diameter = 2.5 ± 0.3 nm). (B) Undoped CDs, 4 h reaction time exhibiting lattice. (C) FFT of Figure 2B with spots matching lattice fringes at a d-spacing of 2.40 Å. (D) 1:2 NCD, 4 h (3.0 ± 0.5 nm). (E) undoped CD, 24 h (diameter = 16 ± 2 nm). All experiments were performed at room temperature under 200 keV acceleration voltage and images were processed using ImageJ.

The fast Fourier transform (FFT) revealed that crystalline particles exhibited a d-spacing of 2.40 Å for undoped CDs (**Figure 3.2C**) and 2.45 Å for NCDs, which are both in agreement with the [100] plane of graphite.¹³⁴ High resolution C(1s) spectra also confirm the graphitic nature of both CDs and NCDs, with strong peaks at 284.8 eV identifying the presence of graphitic C-C/C=C bonding. These results are also in agreement with previously reported CD syntheses in the

literature, supporting a sequential dehydration and polymerization of citrate molecules into nanoparticles as proposed by many groups in the field.^{103,107,111,135} When longer synthetic times were employed the resulting particles increased in both size and polydispersity across all doped and undoped samples (**Figure 3.2E**). This change in size and distribution is expected under the proposed CD formation scheme suggesting a similar if not identical process is at work under our novel buffer-assisted CD synthesis.¹¹¹

Optical Characterization of CDs and NCDs

The synthetic precursors, citrate and urea, both had featureless absorbance spectra in all but the deep UV region. Therefore, any significant change in the observed absorbance following CD purification must be due to products of the hydrothermal treatment. The absorption spectrum of undoped CDs demonstrated a sharp absorption edge beginning at 270 - 280 nm, indicative of $\pi \rightarrow \pi^*$ transitions within sp^2 hybridized carbon (**Figure 3.3A**).¹³⁶

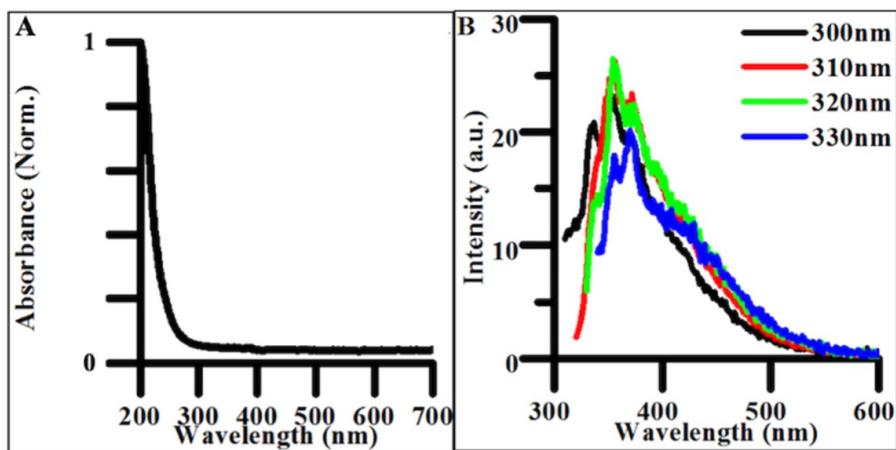


Figure 3.3. Absorbance and Fluorescence Spectra of Undoped Carbon Dots. (A) Normalized absorbance spectrum of undoped CDs synthesized for 4 h. (B) Excitation-independent emission spectra for undoped CDs synthesized for 4 h.

FTIR spectra collected on the lyophilized CD samples confirmed the presence of multiple sp^2 and sp^3 hybridized carbon-containing functional groups such as carbonyl, carboxyl, and alkene groups

which contain pi-bonded electrons capable of undergoing $\pi \rightarrow \pi^*$ transitions explaining possible sources of these optical transitions in undoped CDs (**Figure 3.4**).

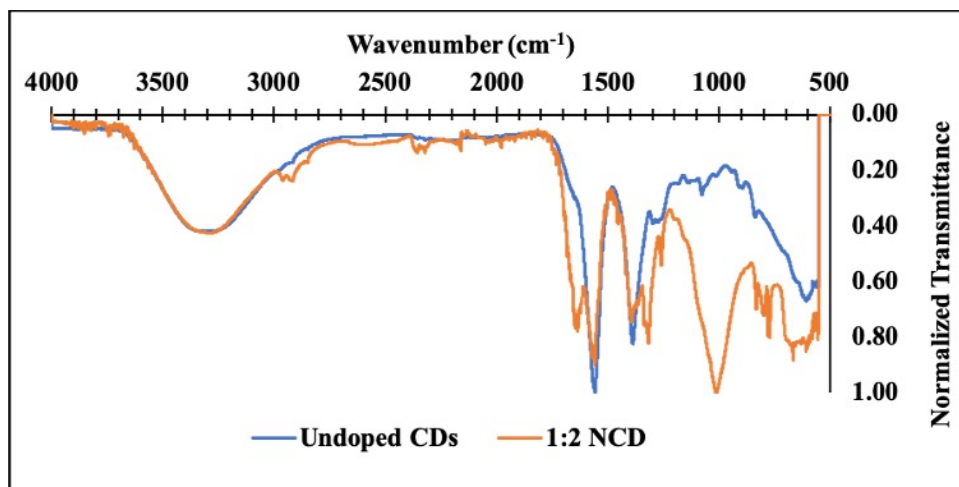


Figure 3.4. Fourier Transform-Infrared Spectroscopy of undoped CDs and 1:2 NCDs. From the spectra, oxygen containing functional groups could be identified on both CD and 1:2 NCD samples (OH stretch: 3300-3400 cm^{-1} ; CH bend: 1386 cm^{-1}). Additional peaks in the 1:2 NCD IR spectra could be assigned to nitrogen containing functional groups (CN stretch: 1315 cm^{-1} NH bend: 1634 cm^{-1} , 3100-3500 cm^{-1}) suggesting incorporation of dopant into both the core and the surface of the final product.

When excited between 300 and 330 nm, CDs exhibited weak excitation-independent emission spectra (**Figure 3.3B**). This emission is believed to be due to radiative recombination of excitons within the carbon-oxygen containing functional groups in the CDs. The origin of fluorescence in carbon materials is highly debated in the literature as both excitation-dependent and excitation-independent behavior have been characterized.¹³⁷ Excitation-independent emissive behavior is believed to be the result of both the uniformity of particle size and homogeneity of functional groups throughout the CD structure. This dependence on uniformity and functional groups explains why optical properties are closely tied to synthetic methods and precursors.¹²¹ Therefore, decreasing the uniformity in the distribution and density of electronic states expressed in the produced particles should result in excitation-dependent behavior in the synthesized product. This was verified in the photoluminescence of polydisperse undoped CD samples reacted for 24

h, where the emission peak redshifted from ~425 to ~475 nm as the excitation energy increased from 300 to 400 nm. The shift in fluorescence from excitation-independent to excitation-dependent behavior with increased reaction time suggests particles synthesized under 4 h synthetic conditions exhibit more highly uniform surface morphologies and size distributions than those formed from longer hydrothermal reactions making them more applicable for general biomedical and energy harvesting applications.

The addition of any concentration of nitrogen-containing dopants into the synthesis significantly impacted the optical properties of the materials. The absorbance spectra of NCDs exhibited the same absorption edge as the CDs in the UV region (280 – 300 nm) as well as a new peak at 340 nm, attributed to $n \rightarrow \pi^*$ electronic transitions, suggesting new electronic states tied to new functional groups resulting from heteroatom doping (**Figure 3.5A**).¹³⁸⁻¹⁴⁰

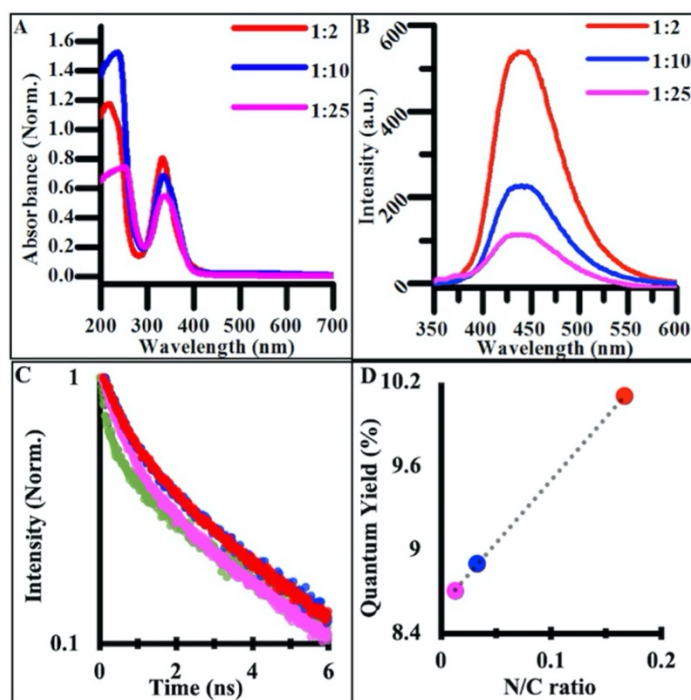


Figure 3.5. Optical Properties of Nitrogen-Doped Carbon Dots as a Function of Doping Ratio. (A) Normalized absorbance spectra of synthesized NCDs under varying doping ratios. (B) Excitation-independent emission spectra NCD samples under 340 nm excitation light. (All CD solutions measured at concentrations of 2.5 mg/ml). (C) Relative quantum yields for synthesized doped and undoped carbon materials. (D) Relative lifetime emission measurements of doped and undoped CD materials with third order polynomial best fits.

The FTIR analysis of NCD materials shows many of the same stretches and bends attributed to the carbon-oxygen containing functional groups found in undoped CDs, while also confirming the presence of new nitrogen containing groups such as pyrrolic nitrogen, nitriles, and amines based new peaks observed in the spectrum (**Figure 3.4**). These additional functional groups are all associated with nonbonding electrons capable of undergoing $n \rightarrow \pi^*$ transitions and are likely the source of new intrinsic optical properties as seen in other syntheses of NCDs.¹⁴¹

The emission spectra of NCDs also featured excitation-independent behavior, suggesting that fluorescence is tied to functional groups rather than other structure-based mechanisms such as core-shell behavior.¹⁴² NCD emission redshifted and increased in intensity with doping when

compared to undoped CDs (**Figure 3.5B**).^{138,140} The drastic increase in quantum yield (QY) from undoped CDs to highly doped NCDs is believed to originate from different electronic states and emissive pathways tied to the new nitrogen-containing functional groups. When batches of NCDs synthesized under different doping ratios were compared, the quantum yield systematically increased with the increase in the nitrogen/carbon ratio while the emission wavelength stayed constant (**Figure 3.5C**). This systematic increase in QY suggests that many of the same functional groups are present across batches of doped NCDs but in different quantities. Additionally, many of the same electronic transitions identified in undoped CDs are still present in NCDs as seen in the FTIR spectra, however their low emission intensity is masked by those of the dopant-containing functional groups when the ratio of dopant to citrate molecule in the reaction mixture is significantly large. Additionally, when NCD batches were synthesized for 24 h, a similar transition to excitation-dependent emission was observed as with undoped CDs suggesting the same dehydration/polymerization formation mechanism is at work in the reported synthesis regardless of the presence of dopant in the reaction. As such, NCDs synthesized for under 4 h of reaction time exhibit uniform surface functionalization, size, and optical emission, promoting their use in a variety of biological or energy harvesting applications.

To further compare the emissive behavior of doped and undoped carbon dots, the time-resolved photoluminescence (PL) was measured and fit to the best order polynomial (**Figure 3.5D**). The PL traces were fit with tri-exponential decay functions, providing three time-constants (**Table 3.1**) that were then used to calculate amplitude-weighted average PL lifetimes, τ_w . Each CD and NCD sample exhibited a τ_w of 2-3 ns, which agrees with previous lifetime measurements conducted on hydrothermally synthesized NCDs from other groups (**Table 3.1**).¹⁴³

Table 3.1. Emissive decay lifetime and quantum yield values (ns) for synthesized NCDs.

	τ_w	τ_1	τ_2	τ_3	X^2	Quantum Yield
1:2 NCD	2.64	0.70	3.26	8.52	1.33	10.1%
1:10 NCD	2.61	0.65	3.35	8.27	1.19	8.9%
1:25 NCD	2.38	0.57	2.95	8.63	1.20	8.7%
Undoped CD	2.25	0.26	3.06	7.17	1.19	0.9%

The origin of CD and NCD fluorescence is complex, originating from multiple emissive transitions amongst electronic states contributed by diverse functional groups within the CD structure.¹⁰¹ Across the samples, there was a slight increase in the average radiative lifetime of the CDs with the increase of dopant concentration. The undoped CDs exhibited the shortest lifetime, at 2.25 ns, while the 1:2 NCDs exhibited the longest lifetime, at 2.64 ns. This change in lifetime indicates that the addition of nitrogen groups provides a more efficient radiative recombination center in the CDs. Conversely, the non-radiative component of the undoped CDs (239 ns) was an order of magnitude larger than those of the NCDs (~25 ns). The significant difference in the non-radiative component between the doped and undoped samples further confirms the idea that nitrogen functional groups are responsible for new non-radiative pathways that are much faster than those present in undoped CDs.

High resolution XPS of the N(1s) region confirms the presence of new nitrogen-containing functional groups following the doping procedure. The 1:2 NCD (**Figure 3.6B**) and 1:10 NCD (**Figure 3.5C**) spectra show clear N(1s) signals, with the relative intensity of the 1:2 NCD spectra being much greater than that of the 1:10 NCD.

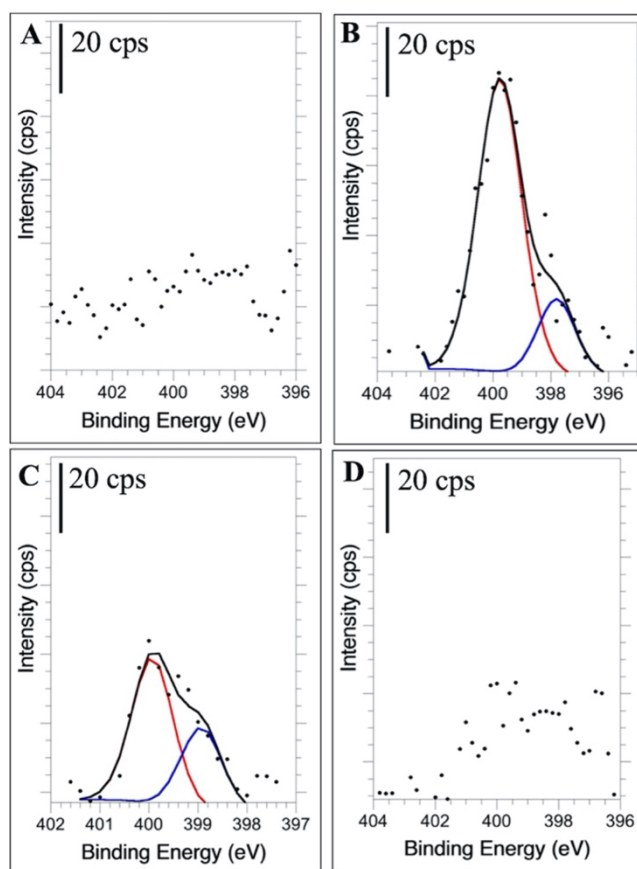


Figure 3.6. X-Ray Photoelectron Spectroscopy of Nitrogen-Doped Carbon Dots. High resolution N 1 s XPS spectra of (A) undoped CDs, (B) 1:2 NCDs, (C) 1:10 NCDs, and (D) 1:25 NCDs.

The difference in peak intensity suggests that higher doping concentrations during synthesis create more nitrogen functional groups throughout the carbon dot, leading to the enhanced absorbance and fluorescence properties observed. The identity of these functional groups, when compared to the corresponding FTIR spectra, are most likely pyridinic ($-C_3N/C-N=C$) and pyrrolic nitrogen (C-N-C) at 398.5 eV and 400 eV, respectively, verifying their incorporation into the nanoparticle (Figure 3.4).^{101,144-146} In the 1:25 NCD spectrum, a weak nitrogen signal was detected (Figure 3.6D), however its low intensity relative to the baseline prevented confident fitting of the peak. Likewise, the undoped CD samples showed no evidence of a nitrogen peak (Figure 3.6A).

Interestingly, as the radiative lifetime of the NCDs increases with dopant concentration, the non-radiative component remains relatively unchanged indicating that the efficiency of the new non-radiative pathway is not dependent on the structural changes induced by higher concentrations of doping during the carbon dot synthesis. The carboxyl groups, which are assumed to be the main radiative centers in undoped CDs, likely still contribute a radiative pathway in the NCDs, but because this pathway is highly inefficient it becomes masked as the dopant concentration, and resulting amount of nitrogen functional groups, increase. High resolution XPS spectra of the C(1s) peak confirm this rationale, as there is little change between the corresponding spectra from the undoped and doped CDs. The changes observed in the emissive properties of CDs and NCDS with respect to doping highlight how many intrinsic properties of the materials are structurally dependent and thus, easily modifiable doping routes can lead to carbon dots exhibiting a range of properties.

Electrochemical Characterization of CDs and NCDs

To apply CD materials to energy harvesting applications, attaining the proper oxidation and reduction potential is crucial in ensuring efficient band alignment between adjacent materials. Using carbon dots doped to varying degrees, electrochemical properties were measured to identify the dependence of the doping concentration on redox potential.

Cyclic voltammetry (CV) of undoped CDs synthesized for 4 h showed two prominent oxidations peak potentials (denoted $E_{\text{ox},1}$ and $E_{\text{ox},2}$, **Figure 3.7A**), in both the initial scans as well as the background subtracted scan (**Figure 3.7A inset**). Only a single reduction reaction (E_{red}) was observed in the potential window tested for the undoped CDs at around -0.44 V (vs Ag/AgCl). Varying the particle size did not significantly change the observed oxidation and reduction

potentials, indicating that size had no impact on the energetics of observed electrochemical properties and, as such, 4 h syntheses were used for all electrochemically tested materials.

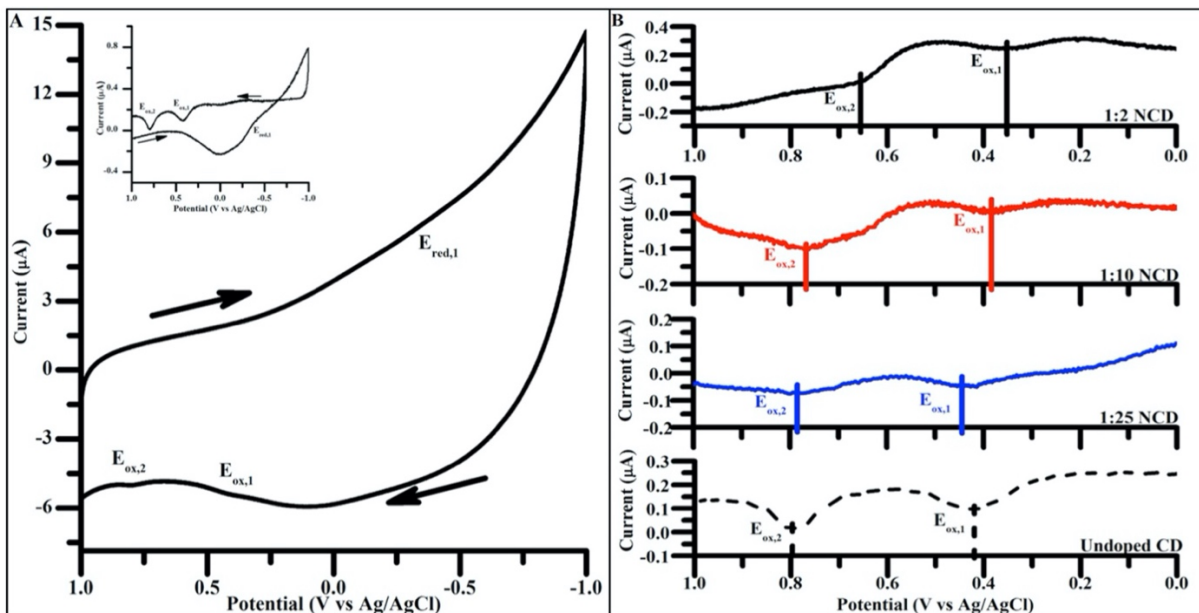


Figure 3.7. Electrochemical Analysis of Undoped and Nitrogen-Doped Carbon Dots. A) Cyclic voltammograms of undoped CDs, 4 h. (Inset: Background subtracted 4 h undoped CD cyclic voltammogram. Background scans performed over the same potential window in mediator containing only 100mM KCl) Scans taken at 200 mV/s from 1.0 V to -1.0 V (vs Ag/AgCl) in 100 mM KCl. Arrows indicate direction of potential sweep. B) Positive potential sweeps of NCDs synthesized with increasing amounts of urea (undoped CD < 1:25 NCD < 1:10 NCD < 1:2 NCD). Scans taken at 200mV/s from 0.0 V to 1.0 V (vs Ag/AgCl) in 100 mM KCl

The same electrochemical analysis was carried out on NCDs synthesized under varying doping ratios. Sweeping the potential in a positive direction showed two distinct oxidation peaks in all NCD samples as seen in the undoped CDs (**Figure 3.7B**). When comparing the E_p of the two oxidation peaks across different doping concentrations for NCD preparation, a shift of $E_{ox,1}$ and $E_{ox,2}$ to more negative potentials occurs with increased dopant levels. Over the range of dopants tested, $E_{ox,1}$ and $E_{ox,2}$ shift 100 mV and 150 mV more negative, respectively, without the need of any post-synthesis surface modifications (**Table 3.2**).

Table 3.2. Measured oxidative peak potentials for CD and NCD samples. Peak potentials were sampled from different CD and NCD batches synthesized from separate 0.67 M citrate buffers.

	$E_{ox,1}$ (V vs Ag/AgCl)	$E_{ox,2}$ (V vs Ag/AgCl)
1:2 NCD	0.35 ± 0.02	0.65 ± 0.001
1:10 NCD	0.40 ± 0.02	0.75 ± 0.02
1:25 NCD	0.39 ± 0.03	0.79 ± 0.01
Undoped CD	0.45 ± 0.03	0.81 ± 0.02

Nitrogen acts as an n-type dopant with respect to carbon, meaning that the inclusion of pyrrolic and pyridinic nitrogen in the particle introduces more electron density to the particle in the form of nonbonding electrons. Pyrrolic and pyridinic nitrogen content in carbon materials are believed to affect catalytic properties of carbon in oxygen reduction, suggesting that such nitrogen groups are also responsible for the observed changes in carbon dot electrochemical properties.^{147,148} Increasing the ratio of nitrogen-containing groups to oxygen or carbon-containing groups in the CD effectively shift the particle composition from electron withdrawing to electron donating groups, which could explain the overall negative shift in oxidative peak potential of the particle surface as the doping ratio is systematically increased over the range of tested dopant levels.¹⁴⁹

To further characterize the electrochemical properties of the as produced CDs and NCDs, the correlation between peak current (i_p) and scan rate (v) was studied using linear sweep voltammetry (LSV). When the i_p was plotted against $v^{1/2}$ and v , the increase in current was found to be more linear with $v^{1/2}$ indicating that electron transfer was governed by diffusion of the carbon dots to and from the electrode surface, rather than an absorption step (**Figure 3.8**).^{86,150}

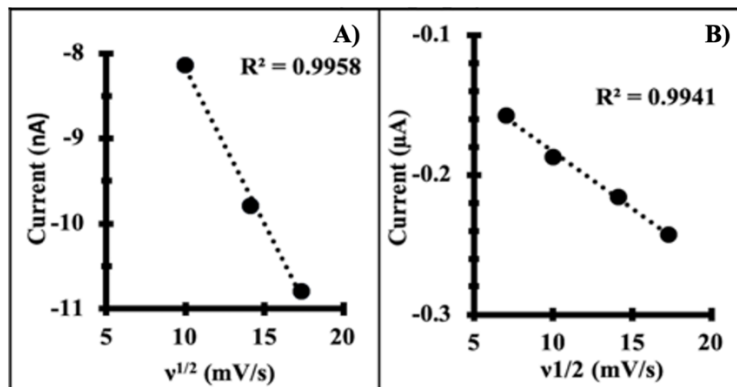


Figure 3.8. Comparison of Peak Current Versus Scan Rate. Comparison of the i_p values measured for NCDs against $v^{1/2}$. Linear correlation of i_p with $v^{1/2}$ indicates dependence on diffusional processes for the oxidations at (A) 0.35 V and (B) 0.65 V.

The same linear dependence on $v^{1/2}$ was seen for 1:2 NCDs. This is of particular interest in energy harvesting applications as it promotes the use of carbon nanoparticles as freely diffusing mediators or tunable, environmentally benign catalysts in photoelectrochemical applications without the need for post-synthesis surface functionalization.

Incorporation of NCDs into PSI-Based Photovoltaic Devices

Due to their size and shape, a prospective application for carbon dots in PSI-based solar cells is for the optimized charge delivery between the protein and external electrode materials. Based on the observed oxidation and reduction potentials for the synthesized batches of doped carbon dots, all NCD batches should be capable of oxidizing F_B^- while carbon dots synthesized under a 1:2 ratio of nitrogen to carbon would be energetically suited to reduce the P_{700}^+ reaction center. To this end, preliminary device testing was performed using mixed multilayers of dialyzed PSI and 1:2 NCDs between p-doped silicon and tin-doped indium oxide-coated polyethylene terephthalate (ITO coated PET) counter electrodes. Solid-state photovoltaics are more suited for CD incorporation as the high solubility of the carbon material would promote delamination in mediated devices.

The alignment of the oxidation bands of 1:2 NCDs and the P_{700}^+ reaction center should facilitate enhanced electron transfer into the protein through the nanoscale carbon particles, increasing the observed photopotentials of tested devices. Despite the addition of carbon dots to the resulting devices, the resulting photovoltages were not statistically different from one another (Figure 3.9).

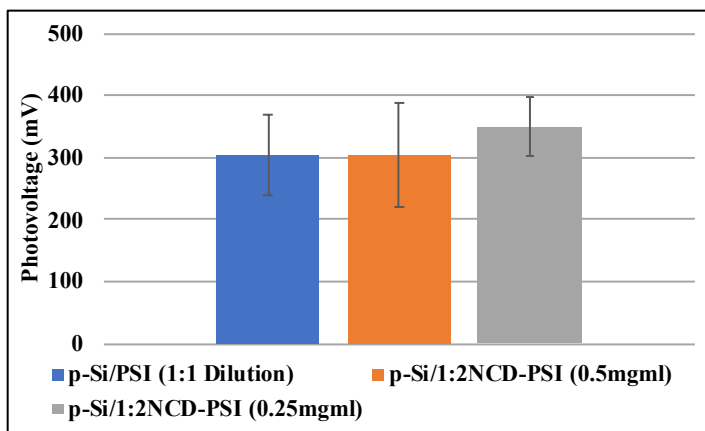


Figure 3.9. Photovoltage Measurements of PSI-Control and PSI:NCD Mixed Multilayers. Photovoltage measurements of PSI or mixed PSI:NCD multilayers on lightly p-doped silicon electrodes. Devices were completed with flexible ITO electrodes, and photovoltage was sampled after recording 20 s of open-circuit voltage in the absence of light. Each device type was tested in triplicate with error bars depicting the standard deviation.

The lack of improvement in measured photovoltages is likely due to inefficient incorporation of the CD materials to the targeted face of PSI. Side-selective functionalization of PSI with NCDs would overcome these challenges and could be achieved using common bioconjugation strategies such as carbodiimide crosslinking. More stable NCD layers consisting of carbon dot-polymer composites could also serve as promising hole transport layers for PSI multilayers within photovoltaic devices.

3.1.4. Conclusions & Future Outlooks

In this work CDs and NCDs were synthesized using a buffer-assisted hydrothermal synthesis. A variety of NCDs were produced and exhibited tunability in regard to both optical and

electrical properties, notably quantum yield and oxidation potential. While it was understood that nitrogen doping can increase the emissive properties of CDs, our findings suggest that many of the same emissive groups contribute to the electrochemical performance of the carbon dots. The negative shift in oxidative peak potential and gradual increase in quantum yield indicate that the new pyrrolic and pyridinic sites contained both on the surface and in the core of the carbon dot play a key role in defining the electronic structure of carbon dot materials. In the case of nitrogen doping, the new electronic states tied to these nitrogen-containing functional groups contribute more emissive electronic pathways. These new electronic states could also contribute new non-bonding electrons more accessible to oxidation than pi-bonded electrons shared amongst sp²-functionalized carbon. When assessing carbon nanomaterials for uses in various applications, varying the doping ratio during synthesis provides a quick and efficient way to tune CD compatibility with additional materials without the need of additional chemical modifications.

Future efforts to improve this work will should be geared towards improving the electrical conductivity and connectivity of CD-layers independent of PSI. Processes such as annealing, conjugation to polymer supports or self-assembled monolayers, or bioconjugation to PSI could help improve the response and stability CD materials in PSI devices and should be explored in future research efforts.

4. APPLICATIONS OF CARBON NANOTUBES FOR INCREASED ELECTRODE SURFACE AREA

Chapter 4 discusses advances in the application of multiwalled carbon nanotubes (MWCNTs) in PSI photoelectrochemical cells as a high surface area electrode material. The first part investigates the interaction between discrete multilayers of MWCNTs and PSI. The research in Chapter 4.1. was conducted with the help of Jade Stanley. The second part to this chapter investigates the viability of freestanding MWCNT composites, or buckypaper, as electrodes for the rapid assembly of PSI-polymer composites through electropolymerization techniques.

4.1. High Surface Area Multi-Walled Carbon Nanotube Electrodes for Photosystem I-Driven Solar Energy Conversion

4.1.1. Introduction

Alongside the rise of conventional inorganic solar cells have been those utilizing materials derived from nature, often referred to as biohybrid devices.⁷⁸ To date there are a number of biological materials implemented in biohybrid devices for energy production, ranging from bacterial colonies to enzymes to redox proteins.¹⁵¹⁻¹⁵³ While these devices differ in performance mechanisms the overall goal remains the same; efficiently generate clean sources of energy while using low-cost, environmentally benign, and easily accessible materials.

Photosystem I (PSI) has been of particular interest in the biohybrid solar cell community as it is capable of converting visible light directly into high energy excitons at near perfect internal quantum efficiency, making it a promising candidate for practical applications of solar energy conversion.¹⁵⁴ In order to improve the viability of PSI-based devices, especially ones relying on diffusional transfer of redox mediators or chemical feedstock to a photoactive electrode, one common strategy is to transition from planar to three dimensional substrates. Advanced device

architectures often immensely increase the available electrode surface area while conserving geometric area which is ideal for efficient energy production at all levels.^{63,155} In biohybrid devices, high surface area electrodes offer improved areal loading capacities for proteins or enzymes, such as PSI, which in turn leads to higher photocurrent densities. As such there is great merit in researching low-cost, biocompatible, and readily deployable materials capable of improving electroactive surface areas in biohybrid energy applications.

To date there have been many instances of utilizing high surface area electrodes with PSI for mediated solar energy conversion. One of the earliest methods reported by Ciesielski et al. utilized porous gold electrodes in PSI photoelectrochemical cells which led to a 7-fold increase in photocurrent densities over their planar counterparts.¹⁵⁶ In addition to metallic electrodes, wide bandgap semiconductors such as ITO have also been used in the fabrication of meso and microporous substrates capable of PSI entrapment, reaching photocurrent densities as high as 270 $\mu\text{A cm}^{-2}$ in mediated devices, surpassing the peak photocurrent densities achieved at porous gold electrodes (300 nA cm^{-2}).^{63,157} Planar carbon materials, such as graphene and reduced graphene oxide, have also been used as inexpensive, robust interfaces with PSI on a variety of underlying surfaces.^{59,158,159}

Carbon nanotubes (CNTs), another allotrope of carbon, offer the same desirable electronic properties as graphene or graphene oxide while offering much higher surface areas and structural stability over due to their unique cylindrical geometry.¹⁶⁰ In the past CNTs have seen limited use with PSI, often focusing on single protein-nanotube electron transfer characteristics rather than rapidly scalable designs for high energy production.¹⁶¹⁻¹⁶³ Previous work has demonstrated how PSI and CNTs conjugates led to photo-responsive devices yet often relies on advance conjugation strategies such as mutation of select residues within the protein in order to ensure

conjugation.^{161,163,164} Similar properties were observed when whole thylakoids were conjugated to multi-walled CNT (MWCNT) surfaces for the light driven splitting of water reaching steady state current densities of $38 \mu\text{A cm}^{-2}$.¹⁶⁵ Linkage of PSI to CNT surfaces has also been achieved using cytochrome c (cyt c) to facilitate direct electron transfer between the carbon surface and P₇₀₀ yielding a maximum photocurrent density of $18 \mu\text{A cm}^{-2}$ across a range of applied overpotentials.¹⁶² Moving beyond chemical conjugation of PSI to CNT structures, there have been advances in utilizing electrostatic interactions between luminal faces of multiple photosystem (PS) proteins to nitrogen-doped MWCNTs, however observed photocurrent densities only reached the order of $1.2 \mu\text{A cm}^{-2}$. Carbon nanotube scaffolds have also seen applications beyond biohybrid devices utilizing PSI, such as enzymatic fuel cells or biosensors, demonstrating the wide range of applications which can be enhanced using CNT materials.¹⁶⁶⁻¹⁶⁸

Expanding upon recent work investigating the performance of conjugated PSI-CNT composites, this research aims to improve the performance of PSI multilayers in biohybrid photoelectrochemical cells through the rapid application of MWCNTs to electrode surfaces as a means of enhancing the electrochemically active surface area. The geometry of MWCNTs and their resulting composites can improve both protein loading and mediator turnover, leading to higher photocurrent densities. In photoelectrochemical cells, the sustained photocurrent density is ultimately limited by on the process of shuttling charge between the PSI reaction centers and the underlying electrode, which can be greatly enhanced by providing more sites for mediator conversion. Carbon nanotubes, specifically MWCNTs, are inexpensive compared to SWCNTs and can be easily applied as coatings or composite layers using solution phase deposition processes with minimal pretreatment making them of particular interest for use in mediated PSI electrochemical cells.

Herein we investigate how MWCNTs can be prepared for rapid deposited following chemical pretreatment to increase the available electrode surface area for biohybrid photoelectrochemical cells. When MWCNT films were used in PSI bioanodes, a roughly 7-fold increase in steady-state photocurrent density was observed without the need of an applied overpotential, secondary electroactive proteins, or additional bioconjugation strategies. These results suggest that MWCNTs could be used to improve mediated biohybrid electrodes in biohybrid photoelectrochemical cells beyond those utilizing PSI.

4.1.2. Materials and Methods

Chemicals

Potassium chloride, ferricyanide, sodium phosphate mono and dibasic, hexamine ruthenium trichloride (RuHex), sodium ascorbate, 2,6-dichlorophenolindophenol (DCPIP) (Fisher Chemical), ferrocyanide and Triton X-100 (Millipore-Sigma) were used as received without further modification. MWCNTs (Millipore-Sigma) with an outer diameter of 20-30 nm were purchased and modified by refluxing in concentrated nitric acid (Fisher Scientific) for 16 h. After removing from reflux, the MWCNTs were collected and washed with deionized H₂O purified in house (18.2 MΩ cm, Barnstead Nanopure, Thermo Scientific, Waltham, MA) via centrifugation using a one speed table-top centrifuge (3400 rpm, Fisher Scientific).

Device Fabrication

Devices with PSI and MWCNTs were made using vacuum assisted deposition. In short, a silicon (100) wafer was coated first with chromium (25 nm) then gold (125 nm) in-house as previously described.¹⁶⁹ The gold electrode was then masked with an insulating electrochemical mask (Gamry Instruments) leaving a 0.71 cm² area exposed. Once prepared, 75 μL of either dialyzed PSI (8-10 kDa MCOW, Spectrum Labs) or 100 μL of MWCNT solutions of varying concentrations were added to the exposed surface and the solvent was removed under vacuum with

successive layers added to devices following complete drying of the prior layer.

Characterization

All electrochemical experiments were performed on a CHI660a potentiostat. Cyclic voltammetry was performed using an electrolyte solution containing either pure 100 mM KCl or 100 mM KCl and 2 mM ferri/ferrocyanide. Electrochemical impedance spectroscopy was performed in electrolyte solution containing 100 mM KCl and 2 mM ferri/ferrocyanide. Electrodes were set at the midpoint potential as measured by cyclic voltammetry and pulsed 10 mV over a frequency range from 10,000 to 0.01 Hz. Photochronoamperometry experiments were performed with varying electrolyte solutions containing one of the following mediator solutions: 2 mM RuHex, 250 μ M DCPIP and 5 mM sodium ascorbate, or 2 mM ferri/ferrocyanide. A 3 M Ag/AgCl reference electrode and platinum mesh counter electrode were also used in all experiments. The working electrode for electrochemical measurements was gold or modified gold unless specified otherwise. For photocurrent measurements, all working electrodes were held at the measured open circuit potential for the analysis.

4.1.3. Results and Discussion

The use of CNT materials as electrode modification materials is often prefaced with chemical oxidation to remove any metal impurities from synthetic catalysts and to improve solubility. Surfactants such as sodium dodecyl sulfate or Triton X-100 can also be used to improve CNT solubility, however in biohybrid electrodes or photoelectrochemical cells the presence of excess surfactant can inhibit performance and retention of vacuum-deposited biological multilayers.⁸² Since biological materials, PSI included, require aqueous conditions to avoid denaturing, chemically treated MWCNTs (t-MWCNTs) compatible with aqueous, polar solvent were used in all tested PSI electrochemical cells. Chemical treatment was achieved by reacting MWCNTs in concentrated nitric acid at 70 °C overnight (16 h). Following treatment, t-MWCNTs

were readily dispersed in DI-H₂O without aggregation leading to highly opaque solutions even after centrifugation due to retained MWCNTs in solution (**Figure 4.1A**). Highly soluble carbon nanotubes are preferable for use with conventional solution-phase deposition processes such as vacuum-assisted deposition, spin coating, and dip coating which are commonly seen in the preparation of PSI-biohybrid electrodes.

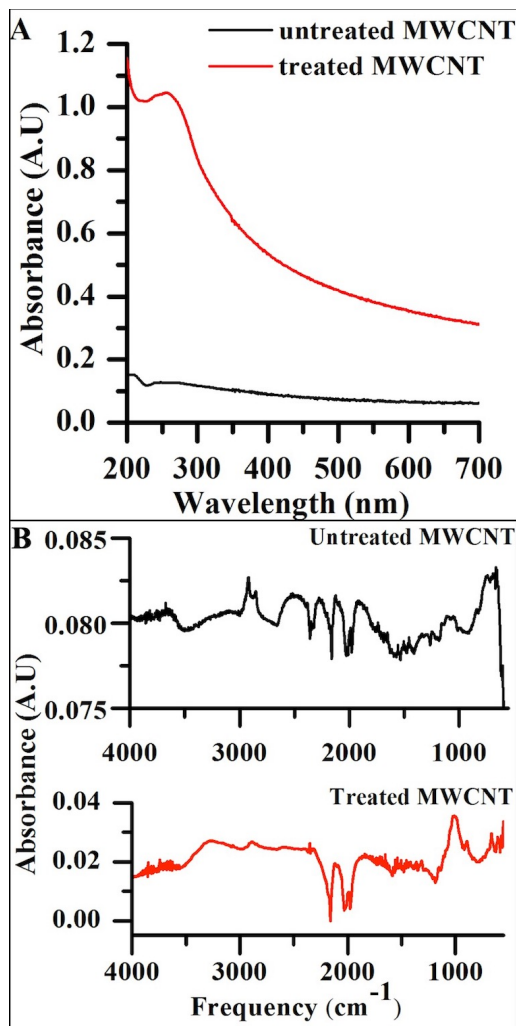


Figure 4.1. Ultraviolet-Visible Absorbance and Fourier Transform-Infrared Spectroscopy of Untreated and Acid-Treated Multiwalled Carbon Nanotubes. (A) Absorbance spectra of aqueous MWCNT solutions following sonication and centrifugation to remove undissolved MWCNTs. (B) FT-IR measurements of dried MWCNTs pre- and post-acid treatment.

The improved solubility of t-MWCNTs is attributed to the formation of polar functional groups on solvent-exposed surface of the nanotube structure, which were confirmed using Fourier

transform-infrared spectroscopy (FT-IR) (**Figure 4.1B**). FT-IR spectra reveal new hydroxyl (-OH, 3250 cm^{-1}), carboxylic acid (-COOH, 1725 cm^{-1}), and carbonyl groups (-CO, 1680 cm^{-1}) which are largely absent from the untreated MWCNT (u-MWCNT) spectrum. Despite chemical changes to the surface of t-MWCNTs, Raman spectroscopy revealed similar D/G peak ratios of 1.31 and 1.36 for u-MWCNT and t-MWCNT, respectively, indicating no significant change to the ratio of sp^2 to sp^3 carbon.¹⁷⁰ Carbon nanotubes exhibit high conductivities due to spanning networks of delocalized pi orbitals making it critical to preserve CNT hybridization following surface functionalization in electrochemical applications.

To characterize electrodes modified with t-MWCNT composites, the electrochemically active surface area (ECSA) enhancement of the t-MWCNT coated gold electrodes was measured. In order to accurately determine surface area enhancement, the double-layer capacitance of electrodes coated with both t-MWCNTs and u-MWCNTs were measured following a protocol recently reported by Voiry et al. (**Figure 4.2, inset**).¹⁷¹

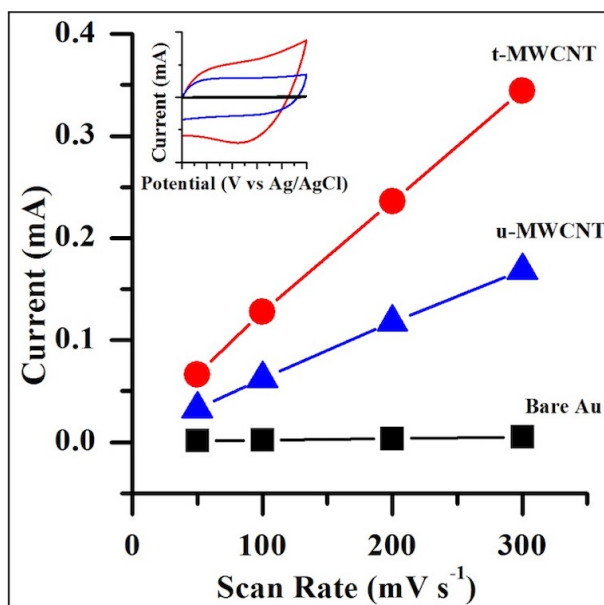


Figure 4.2. Plot of Capacitive Current Vs. Scan Rate for Treated and Untreated Multiwalled Carbon Nanotube Films. Scan rate (mV s^{-1}) plotted against the current response (mA) at 0.35 V vs Ag/AgCl for bare gold electrodes, treated and untreated MWCNT electrodes. Both MWCNT electrodes were coated with $100 \mu\text{L}$ of 1mg ml^{-1} solutions of their respective nanotubes. The inset features comparative cyclic voltammograms of the respective electrodes taken in 100mM KCl at a scan rate of 100mV s^{-1} .

Compared to a planar gold substrate, u-MWCNTs showed a surface area enhancement factor of 36 while the same added mass of t-MWCNTs demonstrated an enhancement factor of 64, indicating twice as much surface area accessible to solvent at treated nanotubes (**Figure 4.2**). This is believed to be due both the more uniform film deposition of t-MWCNT over u-MWCNTs, which experience high inter-nanotube forces leading to aggregation, as well as more solution-electrode interactions at the more hydrophilic t-MWCNT surface. Additionally, the ECSAF enhancement demonstrated strong correlation with deposition solution concentration using this technique (**Table 4.1**).

Table 4.1. t-MWCNT deposition solution concentration and corresponding electrochemically active surface area enhancement factor relative to an unmodified planar gold electrode. All t-MWCNT depositions consisted of 100 μL from stock solutions of different concentrations of nanotubes. Standard deviations were calculated from sample sizes of $n = 3$.

Deposition mass of t-MWCNT (μg)	ECSAF
25	35 ± 1
50	26 ± 2
100	45 ± 2
200	102 ± 5

Resistance to electron transfer was also measured to ensure functionalization of the t-MWCNT surface did not disrupt the conductive delocalized pi orbital network. Electrochemical impedance spectroscopy (EIS) was performed in the presence of ferri/ferrocyanide containing solution and fitted using a Randles equivalence circuit to calculate the charge transfer resistance (R_{ct}) of t-MWCNT films. The R_{ct} for the t-MWCNT films and bare gold substrates was found to be $15.7 \pm 2.83 \Omega$ and $49.1 \pm 16.93 \Omega$, respectively, indicating a slight increase in electrode conductivity with the addition of t-MWCNT network (**Figure 4.3**).

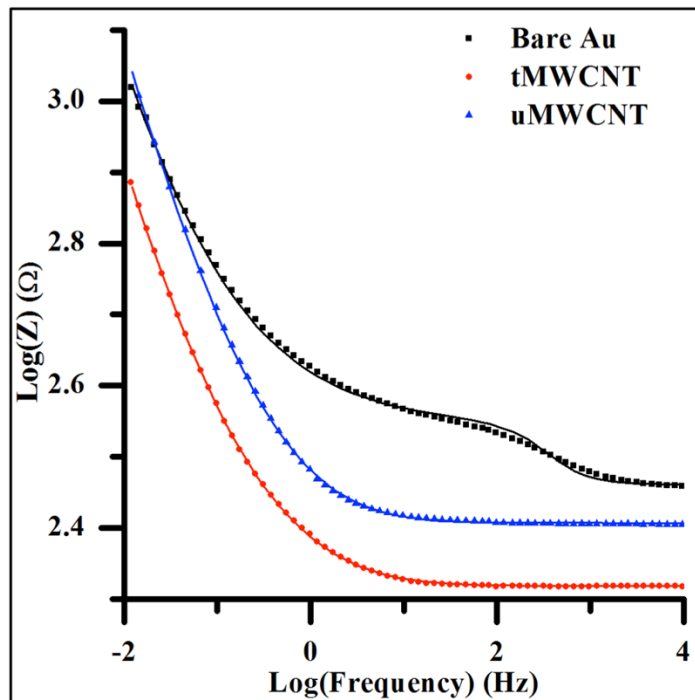


Figure 4.3. Electrochemical Impedance Spectroscopy of MWCNT Layers at Gold Electrodes. Devices of treated or untreated MWCNTs were prepared at gold electrodes and tested with EIS in the presence of ferri/ferrocyanide. The electrodes were held at the midpoint potential for the redox couple as measured by cyclic voltammetry and pulsed with a 10 mV amplitude between 10,000 and 0.01 Hz. Parameters such as R_{ct} were extracted from the resulting data following fitting with a Randles equivalence circuit.

MWCNTs are known for their superior conductivities owing to the expansive delocalized pi networks spanning the lengths of the carbon nanotubes.¹⁷² These changes in conductivity support the idea that the expansive t-MWCNT network is capable of functioning as an extension of the underlying gold electrode. This enhancement of conductivity, despite surface functionalization, is attributed to how MWCNTs can be chemically modified or functionalized on the outer most surface while leaving inner carbon planes unaffected, retaining conductivity despite modification of the surface promoting their use in biohybrid devices over SWCNTs.¹⁷³

To test the effectiveness of t-MWCNT scaffolds in PSI containing photoelectrochemical cells, PSI containing bioelectrodes were assembled and tested in the presence of multiple redox mediators to determine a suitable match for the system in question. Despite the identity of the

mediator across those tested, the PSI multilayers consistently produced anodic photocurrent profiles classifying them as promising bioanodes for broader applications. Of the mediators tested, hexamine ruthenium (RuHex) resulted in the highest photocurrent densities, surpassing currents seen at bare gold and t-MWCNT electrodes, promoting its use for subsequent tests (**Figure 4.4**).

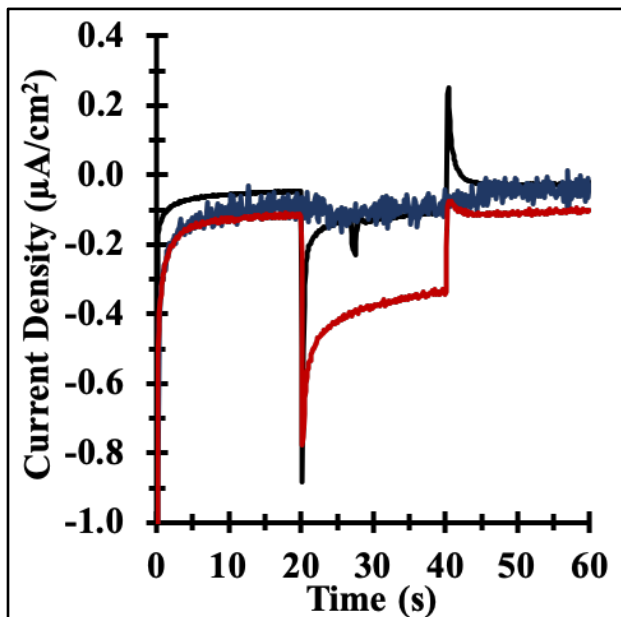


Figure 4.4. Photochronoamperometry of PSI on t-MWCNT Composite. Representative photochronoamperometry (PCA) of Au/PSI (black), Au/t-MWCNT (blue) and Au/t-MWCNT/PSI (red) devices in the presence of mediator containing 2mM RuHex and 100mM KCl. Devices were held in the dark for 20 s followed by 20 s of exposure to white light and finally returned to dark conditions for 20 s over the course of a typical PCA experiment.

PSI multilayers on bare gold electrodes resulted in a steady-state anodic photocurrent density (J_{ss}) of $0.26 \pm 0.04 \mu\text{A cm}^{-2}$ while PSI multilayers deposited on scaffolds of t-MWCNT yielded, on average, photocurrent densities of $0.64 \pm 0.05 \mu\text{A cm}^{-2}$ at loadings of 100 μg , exhibiting a photocurrent density enhancement factor of 2.5-fold. Similar photocurrent enhancement factors were observed for each MWCNT containing device despite the mass of deposited nanotubes when functionalized with PSI multilayers (**Figure 4.5**).

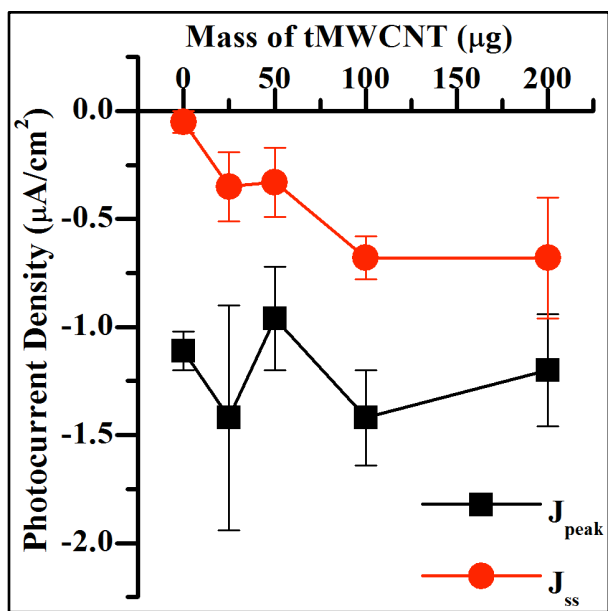


Figure 4.5. Composite Steady State Photocurrent Values of PSI on Treated Multiwalled Carbon Nanotubes. Steady state photocurrent densities of PSI-tMWCNT photoanodes assembled with varying amounts of t-MWCNT. The peak photocurrent density was measured at the time of illumination with white light and the steady state value was calculated by subtracting the dark photocurrent from the photocurrent after 10 s of illumination. All devices were tested in the presence of a 2mM RuHex mediator solution with 100mM KCl as the supporting electrolyte (n = 4 for all device types).

One characteristic of photoelectrochemical cells is the sharp increase in current followed by a rapid decay due diffusion which can be modeled by the Cottrell equation⁸⁶:

$$i_d(t) = \frac{nFAD_0^{1/2}C_0^*}{(\pi t)^{1/2}} \quad \text{Equation 4.1}$$

From the Cottrell equation, the sharp drop off in current is attributed to rapid depletion of oxidized ruthenium species (C_0) in the PSI multilayer, with the overall photocurrent decaying to a steady state value dependent on the influx of oxidized species back to the PSI reaction centers, specifically the terminal iron-sulfur complex.^{86,174} The addition of a t-MWCNT scaffold to the electrodes serves two functions contributing to the increase in photocurrent. First, having a higher electrode surface area provides more sites for mediator turnover, converting reduced ruthenium mediator back to its oxidized form. The t-MWCNT scaffold also serves as a pseudo-porous

substrate, an electrode geometry which has been shown to improve photoelectrochemical cell performance by shortening the distance between PSI reaction centers and the electrode. This in turn shortens the distance reduced species must travel before oxidation at the underlying electrode, overall increasing the frequency of heterogeneous reactions within the PSI multilayer which ultimately lead to higher photocurrent densities.¹⁵⁷

The beneficial impact on device performance was also observed in the percentage of conserved peak current with the addition of t-MWCNTs. In devices containing only PSI, only 11% of the initial peak photocurrent was retained after 10 s of light exposure (**Figure 4.6**).

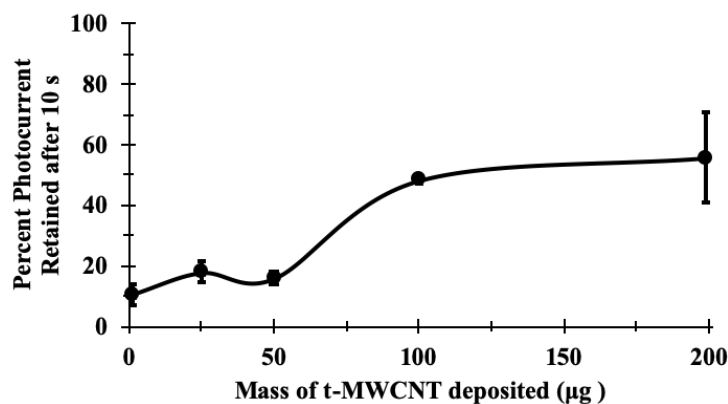


Figure 4.6. Percentage of Retained Peak Photocurrent Density as a Function of t-MWCNT Mass. The retained photocurrent of PSI multilayers assembled on varying amounts of t-MWCNT following 10 s of illumination. Devices were tested in the presence of a mediator solution containing 100 mM KCl and 2 mM RuHex. All data points were collected in triplicate.

Interestingly, devices containing under 100 µg saw drops in peak photocurrent densities to 16% of the initial value. As the mass of t-MWCNTs increased, the percentage of retained photocurrent after 10 s significantly increased to 48% and 56% for 100 µg and 200 µg, respectively. A similar trend is observed when photoelectrochemical cells are operated with mechanical stirring, which improves convection of mediator species throughout the cell.⁸⁶ These results demonstrate how t-MWCNT active layers can offer similar improvements without the need

for mechanical convection, making them an excellent candidate for use in devices utilizing controlled flow of solution throughout the assembled device, such as microfluidic systems. Overall, these results demonstrated how bioanodes containing t-MWCNTs exhibited a 2.5-fold enhancement in J_{ss} due to higher available electrode surface area without the need neither genetic or chemical modification of PSI nor additional electron transfer proteins such as Cytochrome C.

4.1.4. Conclusions & Future Outlooks

Multiwalled carbon nanotubes are a nontoxic, inexpensive material and, once chemically oxidized to improve their solubility, can easily be added to biohybrid devices to increase the available surface area for protein or enzyme loading. Treated MWCNT films deposited on gold wafers significantly enhanced the electrochemically active surface area of the electrode. When t-MWCNT films were used as scaffolds for PSI-based photoanodes, the observed steady-state photocurrent density saw a 2.5-fold increase, with t-MWCNT additions of 100 μg or more allowing for retention of up to 55% of the peak photocurrent without the need for mechanical convection. This work promotes the rapid incorporation of t-MWCNT scaffolds with biohybrid photoelectrochemical cells without the need of any additional genetic or chemical protein modifications. Future efforts towards optimizing the performance of MWCNT-PSI composites would be best focused towards mixed multilayers of protein and nanotubes prior to deposition. By utilizing different mixing conditions, such as ratio and concentration of the two components, the distance between each reaction center at PSI and the surrounding carbon electrode could be optimized as to minimize diffusional losses under sustained operation. These efforts would improve not only PSI photoelectrochemical cells, but also biological and inorganic electrochemical cells controlled by the diffusion of molecules throughout the system of interest.

4.2. Multiwalled Carbon Nanotube Substrates as Flexible, All-Carbon Electrodes for PSI-Based Biohybrid Devices

4.2.1. Introduction

The application of electrochemistry towards energy harvesting and chemical sensing often relies on metal-based electrodes as the gold standard for the field. Recently, advances in fabrication and characterization methods for non-conventional materials have been accompanied by a rise in the diversity and viability of carbon materials as substitutes for conventional electrodes.^{66,67,175-177} Some favorable properties unique to carbon-based electrodes include inherent biocompatibility, high conductivity, diverse chemical functionalization strategies, and low cost.¹⁷⁸⁻¹⁸¹ These advantages have brought about their increasing use in fields ranging from environmental and biological sensing, catalysis, and energy production. Energy production, specifically solar energy conversion, has the most to gain from widespread adoption of carbon-based electrodes since the carbon footprint of the top performing commercial devices is constituted primarily of the energy and environmental considerations surrounding the refinement of high-quality metals and semiconductors needed for efficient light-to-electricity conversion.¹⁸²

One class of solar cell which strongly benefits from widespread implementation of all-carbon electrodes are biohybrid devices. At their core biohybrid solar cells rely on materials derived or extracted from nature, such as the membrane protein PSI, to sustain light-to-energy conversion. Because of the inherent biocompatibility of naturally derived materials biohybrid devices already exhibit superior sustainability over conventional inorganic-based devices.³⁰⁻³² Yet many biohybrid devices still rely on metal-based electrodes detracting from environmental and economic benefits of this class of device. In some instances, carbon materials have been incorporated into biohybrid devices to improve performance or enhance properties of the exterior electrodes demonstrating their compatibility with bioelectrodes. Carbon nanotubes (CNTs), one of

the many allotropes of carbon, offer additional desired properties such as high surface area, good physical strength, and favorable electrical properties making them of particular-interest in light-to-electricity applications.^{180,183} By moving towards metal-free, all carbon electrodes for such biohybrid devices the overall carbon footprint of the solar cell will be greatly diminished leading to instances of truly “green” energy.

Biohybrid devices previously incorporating CNTs have been largely restricted to those containing PSI, the membrane protein in plants paramount to photosynthesis. PSI functions by absorbing low energy light at a special chlorophyll dimer (P_{700}) which is then used in the generation of an exciton-hole pair.⁵³ The exciton is then transferred across the length of the protein through a multistep electron transport chain before arriving at the terminal iron-sulfur cluster (F_B) where it can be transferred to an external carrier. One way in which CNTs have been used in biohybrid devices is by assembling oriented PSI complexes at the carbon surface through readily accessible binding chemistries, achieving unidirectional electron flow throughout the device. Kaniber et al. first characterized the optoelectronic response of PSI bound to CNT surfaces through residue-specific protein modifications demonstrating the creation of active electronic junctions capable of discrete functions.^{184,185} Nii et al. used similar PSI modification strategies to create photobioanodes generating up to 100 nA cm^{-2} under exposure to white light.⁶⁹ Ciornii et al. pushed the photocurrents seen at CNT-PSI conjugates further, up to $0.8 \text{ } \mu\text{A cm}^{-2}$ with modest applied biases.⁶⁸ Additional allotropes of carbon have also been used in similar enhancement strategies for PSI bioelectrodes. Graphene oxide flakes have been the primary carbon allotrope used in this manner due to their high surface area per mass and hydrophilic surfaces, as in results published by Darby et al., Leblanc et al. and, more recently, Morlock et al., with devices reaching photocurrent densities upwards of $13 \text{ } \mu\text{A cm}^{-2}$.^{70,71,186}

Despite the progress made with conjugate PSI-carbon systems, the prospect of an all-carbon, scalable bioelectrode has yet to be realized by the field. One promising carbon material towards realizing this goal is buckypaper (BP), or conductive, flexible composites made primarily of carbon nanotubes.¹⁸⁷ Buckypaper substrates adopt the same superior electrochemical conductivity and activity as their starting material, warranting their use in sensing and energy harvesting applications.¹⁸⁸⁻¹⁹³ Their high conductivity surface area also makes them promising candidates for PSI entrapment within electropolymerized composites, as the entirety of the porous substrate can be utilized for electrochemistry-based processes. In this work, we explore the function of BP as electrodes, with target applications in PSI-based photoelectrochemical cells, in a step towards low cost, flexible bioelectrodes for solar energy conversion.

4.2.2. Materials and Methods

Chemicals

Triton X-100, potassium chloride, hexamine ruthenium trichloride (RuHex), ferricyanide, ferrocyanide, aniline, hydrochloric acid, 3,4-ethylenedioxythiophene (EDOT), poly(sodium 4-styrenesulfonate) (PSS), N,N-dimethylformamide, isopropanol, ethanol (Millipore Sigma, St. Louis, MO) and sodium phosphate monobasic (Fisher Scientific, Hampton, NH) were used as purchased without any additional modification. Nafion (5%, Fisher Scientific) was diluted to 1% in ethanol prior to use. Multiwalled carbon nanotubes (10-20 nm O.D., 10-30 μm) were purchased (cheaptubes.com, Grafton, VT) and used as purchased. All solutions were made using deionized water (DI-H₂O) (18 M Ω cm) prepared from an in-house filtration system (Barnstead Nanopure, Thermo Scientific, Waltham, MA).

PSI Extraction

PSI was extracted from locally purchased baby spinach following a procedure by Reeves and Hall.¹⁹⁴ In short, chloroplast were isolated and lysed following maceration and filtration of whole leaf spinach. Following lysing of the chloroplast, and consequentially thylakoid membranes liberating PSI, the target protein complex was isolated using a hydroxyapatite column and stored at -80 °C until use. The concentration of PSI in the extract was estimated using Baba assay and was found to be 1.0 μM .

Buckypaper Preparation

Buckypaper electrode were prepared following similar vacuum-filtration methodology found in the literature.^{188,192} Briefly, MWCNT suspensions were prepared in either pure DI-H₂O, aqueous solutions containing 1% Triton X-100, or pure N,N-dimethylformamide (DMF) at concentrations denoted in the text (mg mL^{-1}). Complete dispersion of the MWCNTs in either solution was achieved through ultrasonication using a probe sonicator (Ultrasonic Processor, Ace Glass, Vineland, NJ) at 20% amplitude for 60 min prior to use. BP composites were formed by filtering 10 mL, unless otherwise noted, of the MWCNT suspension through Whatman polytetrafluoroethylene filter paper (0.45 μm pore size, 47 mm diameter) (Millipore Sigma) housed in a 5 cm diameter Buchner funnel with the aid of a vacuum pump. Films were then either washed with isopropanol (IPA) or left to dry overnight before being peeled from the filter paper.

Electrochemical Characterization

Following preparation of BP substrates, surface resistivity was measured using a standard multimeter (Amprobe, Everett, WA) across the diameter of the substrate. Additional electrochemical measurements were made using a CH 660A electrochemical workstation (CH Instruments, Austin, TX) using a platinum mesh counter electrode and 1 M Ag/AgCl reference

electrode. A glassy carbon disk working electrode (GCE) was used for both control measurements and as substrate for BP adhesion. BP electrodes were prepared by first cutting the BP into a disk (6 mm diameter) using a biopsy tool. The disks were then adhered to the glassy carbon electrode surface using 7.5 μL of 1 % Nafion solution in ethanol and left to dry for ~ 10 min before use.

For all cyclic voltammetry experiments, electrolyte solutions of 0.1, 1, or 2 M KCl and either 2 mM ferri/ferrocyanide, 2 mM RuHex, or no added mediator were used.

Electropolymerization was performed using a heterogeneous polymerization solution using a ratio of two premade solutions denoted A and B (in the form A:B). Solution A contained the monomer molecules for the target polymer, either polyaniline (PAni) (1 M aniline, 1 M hydrochloric acid, and 0.02 M sodium phosphate) or poly(3,4-ethylenedioxythiophene) polystyrene sulfonate (PEDOT:PSS) (0.02 M EDOT, 0.2 M PSS). Solution B was either a blank solution of 200 mM sodium phosphate with 0.001% Triton X-100, or eluted PSI following extraction. After combining solutions A and B in a 1:4 ratio A to B, electropolymerization was performed either potentiostatically (+1.2 V vs Ag/AgCl) or using cyclic voltammetry by scanning from 0 V to +1.4 V for a predetermined number of cycles at 0.1 V s⁻¹.

Additional Instrumentation

Raman measurements were conducted on a Thermo Scientific DXR confocal raman microscope. A window from 200 to 3500 cm⁻¹ was used for all scans, making sure to sample from the uppermost layer of nanotubes. All measurement were made using a 532 nm laser under normal operation parameters.

Scanning electron microscopy of the samples was conducted using a Zeiss Merlin system with a GEMINI II column using an InLens secondary electron detector. Imaging was performed at working distances of 5 mm with an accelerating voltage of 5.0 keV.

4.2.3. Results & Discussion

Buckypaper Preparation & Characterization

Vacuum-assisted filtration was chosen to fabricate BP substrates in accordance with previously published methods (**Figure 4.7**).¹⁹⁵⁻¹⁹⁷ While BP electrodes have been prepared using both single-walled and multiwalled carbon nanotubes (SWCNT & MWCNT, respectively), the electrodes prepared in this work consisted of MWCNTs for their higher surface area, improved structural strength and preserved electrical properties following surface modification.¹⁹⁸ To achieve adequate suspension of the MWCNTs, ultrasonication was required to overcome intranotube attraction which led to high aggregation, particularly in aqueous solvents. Inadequate solvation of MWCNTs prior to vacuum filtration led to patchy BP films unsuitable for use as electrodes.

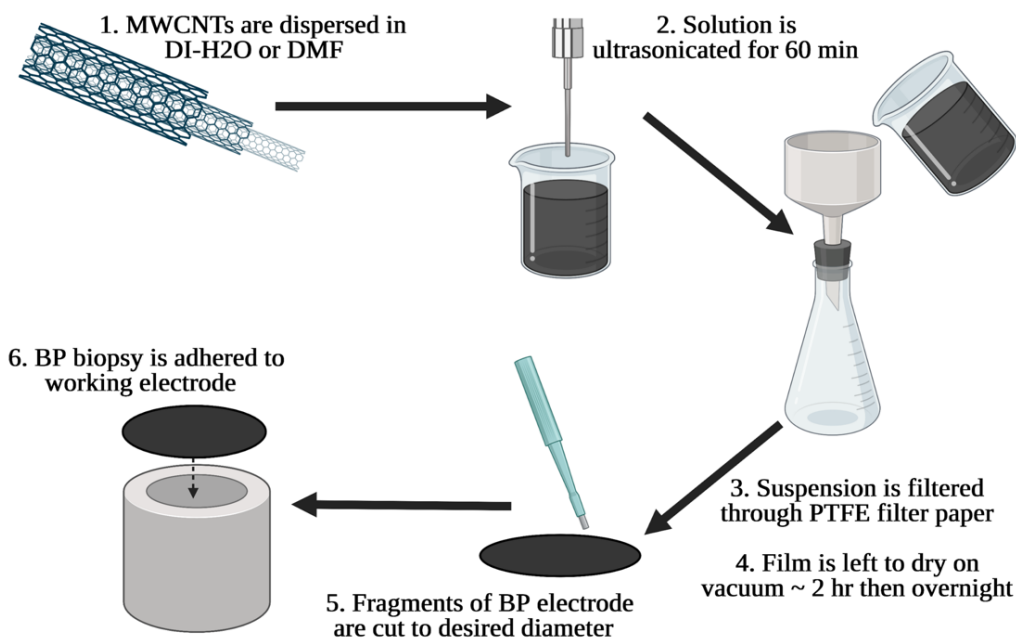


Figure 4.7. Fabrication schematic for BP electrodes using vacuum-assisted filtration. A representative scheme of the process used to fabricate BP electrodes. Figure made using www.biorender.com.

After ultrasonic treatment, MWCNT solutions remained homogeneous for a few days, and even longer if surfactant-containing solutions were used. MWCNT solutions in DMF were also prepared as to prepare surfactant-free BP electrodes. While functional PSI composites can be prepared in the presence of surfactant, chemicals like Triton X-100 can significantly impact electrochemical performance or molecular interactions at the electrode surface.^{177,188,199} It should be noted, however, that suspensions of carbon nanotubes in DMF were less stable than those made in surfactant-containing solutions and could not be prepared above 3 mg mL⁻¹, resulting in thin films susceptible to tear upon removal from the filter paper.

To prepare BP substrates, 10 mL aliquots of dispersed MWCNTs were passed through a 0.45 μm membrane filter using a vacuum-assisted filtration apparatus. The resulting BP composite was then left on vacuum for an additional 2 hr followed by resting at room temperature overnight to allow for adequate drying. Once dried, the BP substrates were carefully removed from the filter paper and used as prepared unless otherwise specified. Initial formation attempts using low masses of deposited MWCNTs (<30 mg) produced BP electrodes which either cracked upon drying or were too thin for removal from the underlying filter paper without tear. By increasing the mass of MWCNTs deposited, thicker composites suitable for use as free-standing electrodes were removed from the filter paper with ease (**Figure 4.8**). To reproducibly form freestanding BP substrates, a minimum of 60 mg of MWCNTs was applied for each tested electrode.

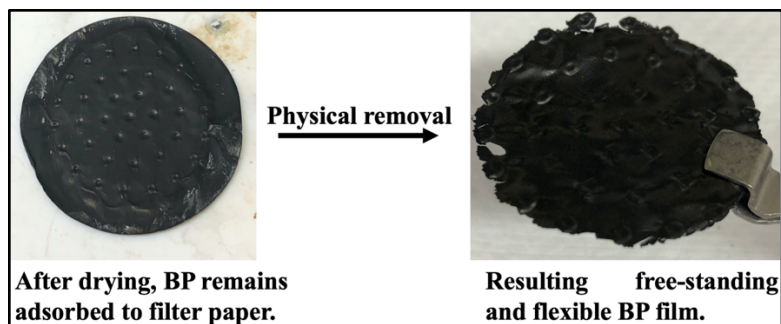


Figure 4.8. Images of Buckypaper Before and After Removal from Filtration Substrates. Buckypaper following vacuum-assisted filtration and drying before (left) and after (right) removal from the underlying filter paper.

All prepared BP substrates were first tested for electrical conductivity to ensure a coherent nanotube network was formed using this process. On average, the freestanding BPs exhibited surface conductivities of roughly $20 \Omega \text{ cm}^{-1}$ measured across the diameter of the substrate rivaling conventional metal electrodes such as gold or platinum. The superior conductivity of BP films suggests that the conductive framework of the pristine MWCNTs is preserved throughout suspension and filtration. Raman microscopy was used to verify the unchanged surface of MWCNTs following assembly into BP films which helps preserve the high conductivity of the starting materials. Furthermore, BP conductivity persisted when manually bending the substrates to conformations unachievable by bulk metal electrodes further demonstrating the advantages of all-carbon electrodes.

The resulting BP electrodes were tested for electrochemical activity using biopsied samples mounted to the end of glassy carbon electrodes with Nafion. Initial scans revealed poor electrode behavior under low electrolyte concentrations ($\sim 0.1 \text{ M KCl}$) when compared to similar scans performed at planar disk electrodes. The elliptical shape of the charging current (i_c) and wide peak splitting in voltammograms at the BP electrodes suggest unideal capacitive behavior of the carbon electrode (**Figure 4.9**).

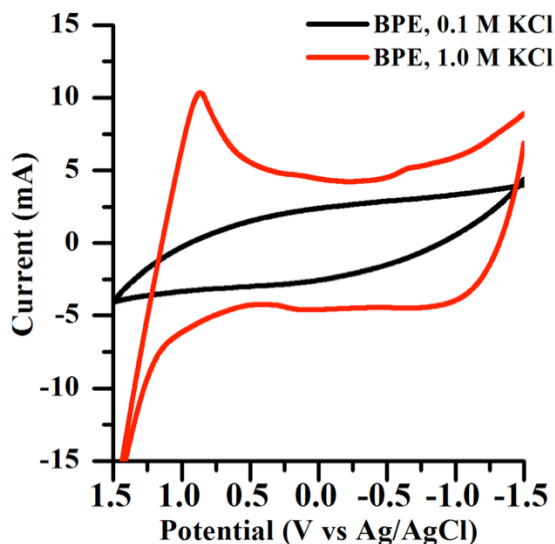


Figure 4.9. Cyclic Voltammograms of BP electrodes Under Varying Electrolyte Concentration. Cyclic voltammogram of BP modified glassy carbon electrode in 0.1 M KCl (black) and 1.0 M KCl (red) at a scan rate of 0.1 V s^{-1} . Under low electrolyte conditions, gradual increases in charging current are observed over the course of the potential scan. At high electrolyte concentrations (1.0 M KCl), charging currents are more consistent allowing for new faradaic processes tied to solvent oxidation/reduction are observed in the voltammogram.

At higher electrolyte concentrations the capacitive behavior of BP electrodes resembles that of an ideal double layer capacitor as evidenced by the more rectangular current profile.⁸⁷ Additionally, solvent oxidation is observed (1.0 V vs Ag/AgCl) at higher electrolyte concentration demonstrating how faradaic processes can be suppressed through poor solution resistances and competition between migration and diffusional processes.^{88,200} Chemical detection and solar-driven energy production often rely on heterogeneous reactions between the electrode and analytes of interest. Careful consideration of supporting conditions, such as electrolyte concentration, when working with high surface area carbon substrates versus their planar counterparts.

Using solutions of higher electrolyte concentrations, changes in the faradaic peak currents of known redox couples were used compare electroactive surface area between electrodes. Cyclic voltammetry was performed in solutions containing 2 mM of both ferricyanide and ferrocyanide. Initial scans in low electrolyte concentration (0.1 M KCl) verify poor faradaic electron transfer under standard electrolyte concentrations used in the field further confirming the need for high

electrolyte concentrations at BP electrodes (**Figure 4.10**). Poor electrode behavior was most prominent in the high peak-to-peak separation (ΔE_p) and broad shape of the ferri/ferro redox couple at BP electrodes compared to control scans at glassy carbon electrodes (**Figure 4.10**). At higher electrolyte concentrations, more defined peaks are seen at both BP and planar electrodes signifying a return to ideal electrochemical behavior allowing for further electrochemical characterization of the prepared electrodes.

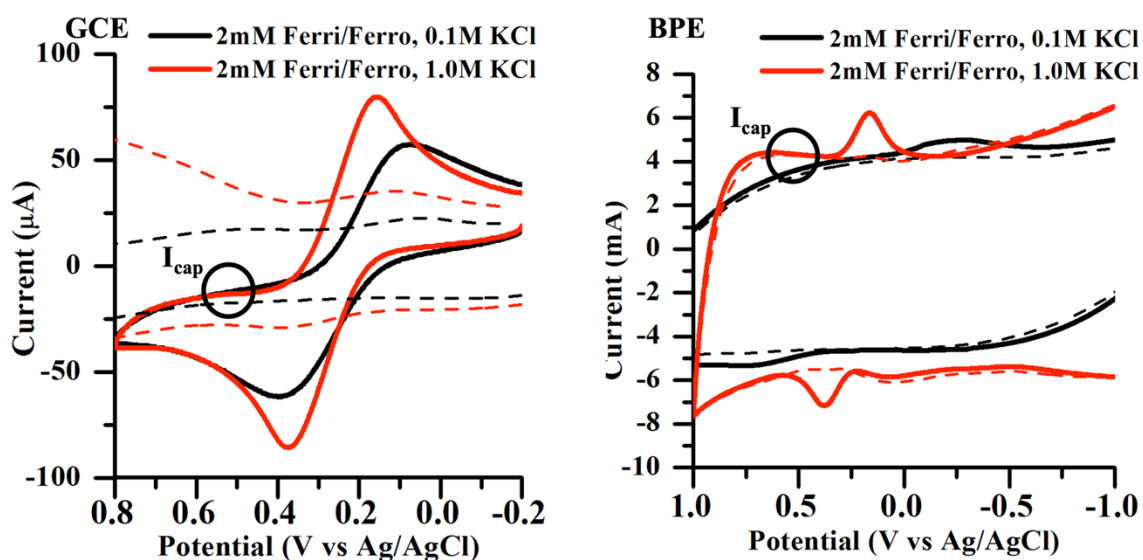


Figure 4.10. Cyclic Voltammograms of Ferri/Ferro at GCE and BP Electrodes in Different Concentrations of Supporting Electrolyte. Cyclic voltammograms at a glassy carbon electrode (left) and buckypaper electrode (right) in the presence (solid) and absence (dashed) of 2 mM ferri/ferrocyanide at different electrolyte concentrations. A scan rate of 100 mV s^{-1} was used for each run.

Using the faradaic peak current, the electroactive surface area of the as-prepared BP electrodes was measured under two different deposition masses of MWCNTs (**Figure 4.11**). BP electrodes prepared from 6 mg mL^{-1} MWCNT (BP₆) produced higher peak currents for the oxidation and reduction of ferri/ferrocyanide which correlate with an increase in the available electrode surface area. Peak currents increased from -0.04 to -0.7 mA and 0.04 to 0.9 mA for the oxidation and reduction, respectively, representing a 17 and 22-fold enhancement in the two

processes due to increased electrode surface area between planar glassy carbon and BP₆ electrodes. Based on the geometric area of the used disk GCEs ($r = 0.15 \text{ cm}$; $A = 0.071 \text{ cm}^2$) the electrode surface area for BP₆ is calculated to be 1.54 cm^2 based on the observed faradaic processes.

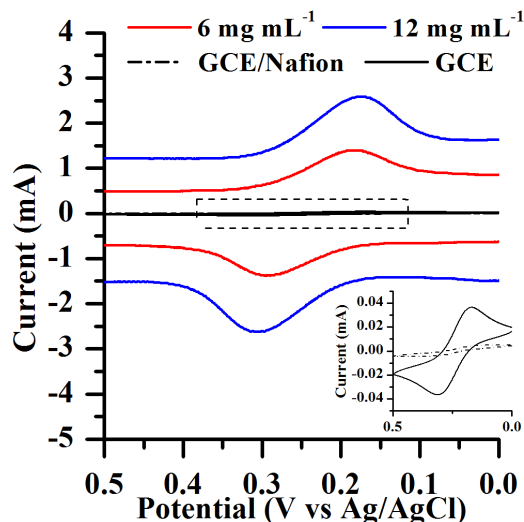


Figure 4.11. Cyclic Voltammograms of Ferri/Ferrocyanide Performed at BP Electrodes Prepared From Different Amounts of MWCNTs. Cyclic voltammograms of 2mM ferri/ferrocyanide in 1 M KCl at BP films made from stock MWCNT solutions of different concentrations. Control scans at GCE and Nafion-modified GCE can be seen in the inset. All scans were collected at 0.05 V s^{-1} .

While the raw surface area showed significant enhancement with the change in electrode, so too did the relative standard deviation of surface area enhancement between electrodes. BP electrodes exhibited a 15 % RSD in surface area compared to the 4 % RSD seen in planar GCE electrodes. This variance in the surface area of produced electrodes is likely due to the fabrication process, as MWCNTs are randomly compiled together during filtration assembly. In addition to increased variance between BP electrochemical reversibility also decreased, with the peak current ratio ($I_{p,a}/I_{p,c}$) dropping from 0.99 to 0.75 indicating a preference for reduction reactions at the BP surface. Despite these drawbacks, the facile fabrication, as well as the superior surface area highlight BP materials as promising electrodes for inexpensive, accessible, and metal-free electrodes.

BP electrodes prepared from 12 mg mL⁻¹ solutions (BP₁₂) were significantly thicker than BP₆ electrodes making them easier to remove the underlying filter paper formation. The resulting BP₁₂ electrodes were tested under similar electrochemical conditions for surface area enhancement and stability. Cyclic voltammograms showed higher peak currents of -1.3 and 1.5 mA for the oxidation and reduction peaks, respectively, reflecting an electrode surface area of 2.84 cm², or a 40-fold increase over bare GCEs (**Figure 4.11**). Increased current between BP samples is to be expected, as nearly twice the mass of MWCNTs was deposited on the filter paper during BP preparation, and as such the increase in peak currents for the BP₁₂ were roughly 2-fold over the BP₆.

Determining the Impact of Uncompensated Resistance at BP Electrodes

During electrochemical testing, it was observed that the BP electrodes exhibited large scan rate-dependent peak splitting (ΔE_p) compared to conventional disk electrodes. Initial tests measuring i_p dependence on scan rate (v) revealed strong correlation of both anodic and cathodic peak currents with $v^{1/2}$ indicating diffusional-controlled redox behavior over adsorption processes. Uncompensated solution resistance (R_u) can cause electrochemical systems to deviate from ideal behavior, observed as large ΔE_p in systems with high net currents (i.e. high surface area electrodes or high specific capacitance materials).^{87,201} Similar trends in ΔE_p and R_u have been observed in MWCNT-composite electrodes, and are to be expected in BP electrodes due to the nature of the material.²⁰² To further probe the impact of supporting electrolyte concentration on voltametric performance of BP₆ electrodes, systematic CV experiments in solutions of 2, 4, and 8 mM ferri/ferro at different concentrations of supporting electrolyte were performed (**Figure 4.12**).

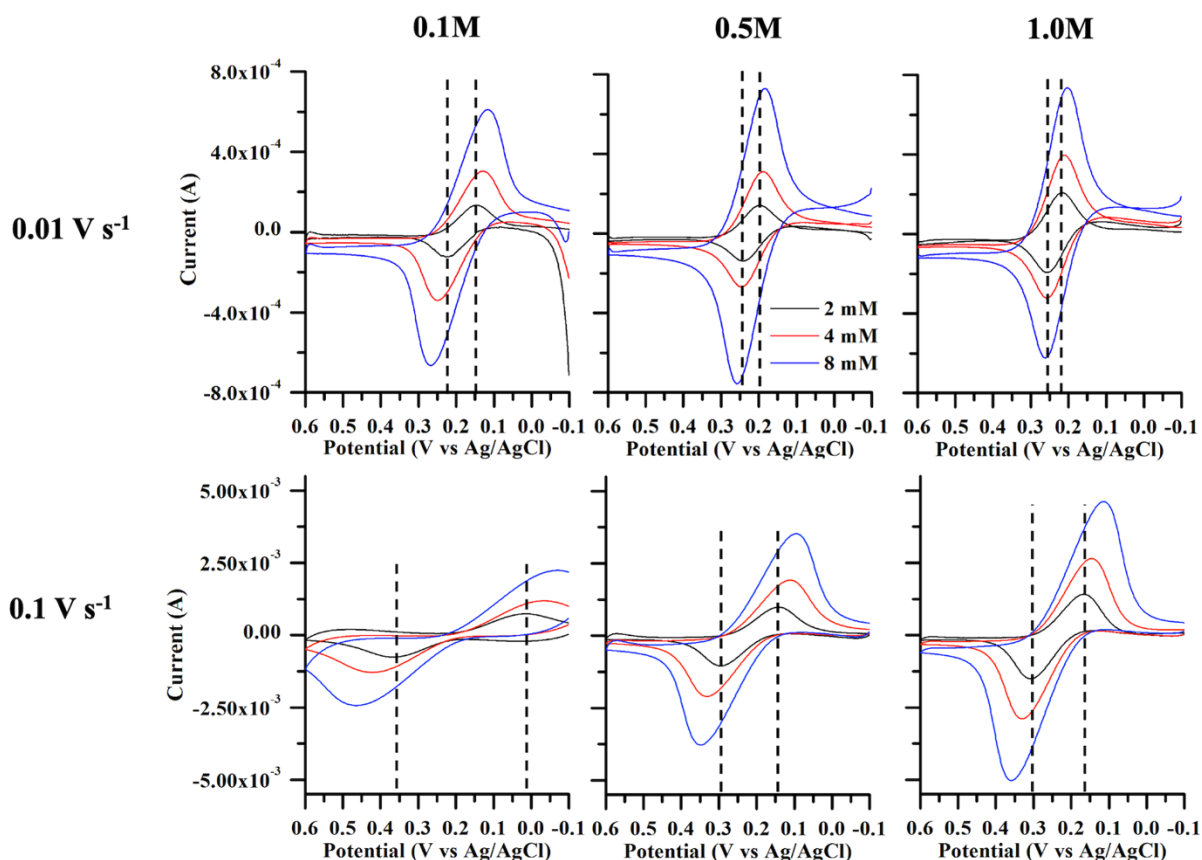


Figure 4.12. Dependence of Increases in ΔE_p with Scan Rate on Analyte Concentration for BP_6 Electrodes. Cyclic voltammograms at 0.01 and 0.1 $V s^{-1}$ of 2, 4, and 8 mM ferri/ferrocyanide solutions at BP_6 electrodes under different concentrations of KCl (0.1 M – 0.5 M – 1.0 M). As the magnitude of the current increases, either due to increased analyte concentration (black – red – blue) or increased scan rate, high electrolyte concentrations are required to preserve ideal electrochemical behavior. Dashed lines are drawn from the peak potentials seen at the lowest (2 mM) concentration of ferri/ferrocyanide for reference against the two additional cyclic voltammograms.

Prior to analysis, the capacitive current at each of the corresponding BP electrodes was measured and subtracted from the voltammogram. At low electrolyte concentrations (0.1 M KCl), ΔE_p for the ferri/ferro redox couple increases drastically with both scan rate and analyte concentration. As the supporting electrolyte concentration increased, the scan rate-dependence of ΔE_p became less prominent. In addition, the observed ΔE_p became more uniform at a single scan rate across tested analyte concentrations in the presence of 1 M KCl.

The strong influence of supporting electrolyte concentration on the electrochemical performance of BP electrodes likely ties back to the drastic increase in surface area and capacitance over conventional glassy carbon electrodes.^{189,203} Under low electrolyte concentrations the double layer capacitance (C_{dl}) charging is drawn out over much of the potential window, as observed with the drifting charging current in solutions of pure electrolyte (**Figure 4.9**). These impacts can lead to broadened and suppressed peaks, resembling heterogeneous kinetic limitations.⁸⁶ At higher concentrations of supporting electrolyte, capacitive charging occurs to completion in shorter times. This in turn allows for better analysis of kinetic limitations of the produced BP electrodes independent of influence from effects tied to R_u or C_{dl} . Similar effects have been reported by Ounnunkad et al. where BP kinetics improved after intercalating the substrate with secondary polymers to reduce the immense capacitive current of bare substrates.²⁰⁴

Electrochemical impedance spectroscopy (EIS) was performed in tandem to the above CV study to further measure the electrolyte concentration dependence of BP electrode properties (**Figure 4.13**).

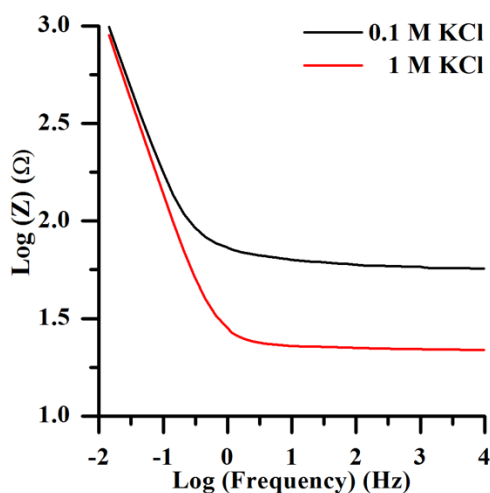


Figure 4.13. Electrochemical Impedance Spectroscopy of BP6 Electrodes in 0.1 and 1 M KCl. Bode plot of the impedance response from 10^4 to 10^{-2} Hz for BP₆ electrodes in differing concentrations of KCl. R_u can be interpreted from the impedance response at high frequencies.

By fitting the collected data against a Randles equivalence circuit, values for R_u could be determined. As suspected, R_u significantly decreased from $58 \pm 2 \Omega$ to $18 \pm 5 \Omega$ between supporting electrolyte concentrations of 0.1 and 1 M KCl, respectively. The contribution of R_u to the observed electrochemical potential for a given system can be modeled by Ohms law (**Equation 4.2**):

$$V = iR_u \quad \text{Equation 4.2}$$

In the equation above, i is the magnitude of the current and R_u is the uncompensated resistance of the system as measured using EIS. At the high currents ($\sim 10^{-4}$ A) seen at BP₆ electrodes, the ohmic drop from R_u to the observed peak potentials quickly becomes significant in comparison to contributions due to quasireversible limitations. At low electrolyte concentrations, the ohmic drop quickly increases from 10s of mV to 100s of mV at higher currents from increased analyte concentration or faster scan rates. By increasing the supporting electrolyte concentration, and in doing so reducing the observed R_u by nearly 70%, the contribution of ohmic drop to the system quickly diminishes (< 10 mV), especially at low analyte concentrations and slow scan rates. High electrolyte concentrations also facilitate greater current densities at fast scan rates, with the peak currents observed at 0.1 V s^{-1} increasing on average by a factor of 2.3 for each concentration of analyte. These results suggest that operational parameters must be carefully considered for systems utilizing carbon-based high surface area electrodes.

Determination of Heterogeneous Rate Constants at BP₆ Electrodes

To further characterize the assembled BP electrodes under sufficient supporting electrolyte concentrations, the heterogeneous electron transfer rate constants (k^0) were calculated based on the Nicholson method for quasi-reversible systems.²⁰⁵⁻²⁰⁷ Using the Nicholson approach, it is possible to calculate k^0 from the ΔE_p of a redox mediator in solution using the following equation:

$$k^{\circ} = \psi \left[\pi \left(\frac{nF}{RT} \right) D \nu \right]^{1/2} \quad \text{Equation 4.3}$$

where ψ is a dimensionless parameter, D is the diffusion coefficient of the molecule in solution ($\text{cm}^2 \text{s}^{-1}$), ν is the scan rate of the solution (V s^{-1}), n is the number of electrons transferred, and the from the original article by Nicholson or calculated using the following equation²⁰⁸:

$$\psi = \frac{(-0.6288 + 0.0021 * \Delta E_p)}{(1 - 0.017 * \Delta E_p)} \quad \text{Equation 4.4}$$

Hexamine ruthenium trichloride (RuHex) was used for all calculations of k° at both GCE and buckypaper electrodes. At polished GCEs, excellent reversible behavior was observed at all tested scan rates, with consistent ΔE_p of ~ 70 mV. Since Nicholson's approach is modeled for quasi-reversible systems, literature values for k° were used for comparison.²⁰⁸ BP₆ and BP₁₂ electrodes, on the other hand, did exhibit scan rate-dependent peak splitting validating the use of Nicholson's method for determining electrode kinetics in conditions minimizing contributions due to R_u (Figure 4.14).

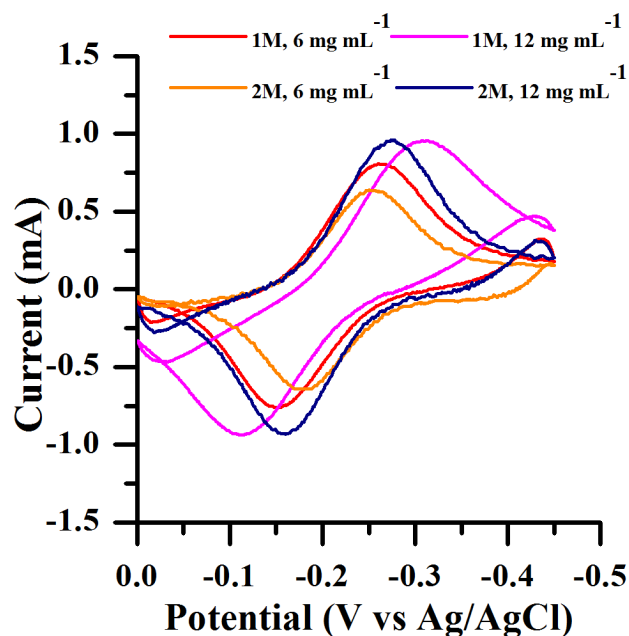


Figure 4.14. Background Subtracted Cyclic Voltammograms of BP Electrodes in the Presence of RuHex. Background subtracted cyclic voltammograms of 2 mM RuHex in varying concentrations of KCl at BP₆ (red/orange) and BP₁₂ (blue/magenta) electrodes.

To better determine the true ΔE_p at both BP electrodes, the non-faradaic current was first measured in the absence of the redox couple and background subtracted for each scan. Across the tested scan rates, both electrodes exhibited large ΔE_p values quickly deviating from the ideal $59/n$ mV, with n representing the number of electrons transferred. The resulting values are reported in **Table 4.2**.

Table 4.2. ΔE_p (mV), ψ , and k° (cm s^{-1}) for 2mM RuHex in 1 M KCl measured at at BP₆ and BP₁₂ electrodes at 0.1 V s^{-1} .

	ΔE_p	ψ	$k^\circ \times 10^3$
BP ₆ – 1	106	0.51	4.94
BP ₆ – 2	119	0.37	3.66
			4.3 ± 0.9
BP ₁₂ – 1	207	0.098	0.76
BP ₁₂ – 2	193	0.077	0.97
			0.9 ± 0.1

The calculated rate constant for the systematic oxidation and reduction of RuHex at BP₆, $4.3 \times 10^{-3} \text{ cm s}^{-1}$ was reasonable based on reported rate constant calculations for graphitic screen-printed electrodes ($\sim 2 \times 10^{-3} \text{ cm s}^{-1}$) found in the literature.^{209,210} Despite the higher electroactive surface

area of BP₁₂, the calculated heterogeneous rate constant of BP₆ was nearly 5-fold higher than the thicker electrode. The difference in k° could be the result of higher competition between non-faradaic and faradaic processes at BP₁₂ surfaces. To investigate this possibility, the same experiments were conducted in electrolyte containing 2 M KCl. The resulting electrochemical values are reported in **Table 4.3**.

Table 4.3. ΔE_p (mV), ψ , and k° (cm s⁻¹) for 2mM RuHex in 2 M KCl measured at at BP₆ and BP₁₂ electrodes at 0.1 V s⁻¹.

	ΔE_p	ψ	$k^\circ \times 10^3$
BP₆ – 1	74	1.82	18
BP₆ – 2	69	2.80	28
			23 ± 7
BP₁₂ – 1	150	0.2	2.0
BP₁₂ – 2	112	0.4	4.3
			3 ± 2

Both BP electrodes showed reduced ΔE_p and increased k° values by factors of 5.75 and 3 for BP₆ and BP₁₂, respectively, by doubling the supporting electrolyte concentration to 2 M KCl. Increased rate constants at high electrolyte concentrations suggest that competing non-faradaic processes at high surface area electrodes can have competitive effects on faradaic processes, which are the target of applications in sensing, electrocatalysis, and energy production. These results compliment kinetic studies at BP electrodes which have shown that hydrophilic BP surfaces are crucial for obtaining favorable reaction kinetics in aqueous systems.²¹¹ As such, a balance must be met between increased surface area and the supporting electrolyte concentration in order to efficiently optimize both parameters.

Buckypaper-PSI Electrodes in Photoelectrochemical Cells

To test the viability of BP composites as electrodes in biohybrid photoelectrochemical systems, PSI was immobilized within a conductive polymer matrix at the electrode surface and tested for photoactivity. The conductive polymers polyaniline (PAni) and poly(3,4-

ethylenedioxythiophene) polystyrene sulfonate (PEDOT:PSS) were chosen for PSI immobilization due to their previous success in past reported devices.^{60,61,212} Polymerization efficacy was evaluated for both PANi and PEDOT:PSS at BP electrodes to determine if competing electrochemical processes (i.e. solvent oxidation) would conflict polymer growth (**Figure 4.15**).

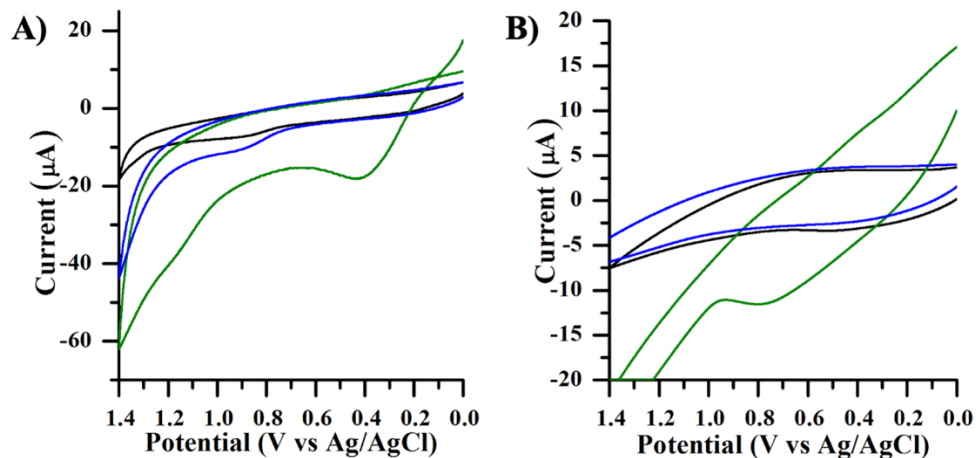


Figure 4.15. Onset Electropolymerization Potential for PEDOT:PSS and PANi at GCE and BP Electrodes. Cyclic voltammograms of phosphate buffer (**black**) and aniline (**green**), or 3,4-ethylenedioxythiophene) and polystyrene sulfonate (**blue**) at (A) bare GCE or (B) BP₆ electrode. Scans were conducted at 100 mV s⁻¹.

At both GCE and BP₆ electrodes, electropolymerization of aniline into PANi occurred around 1.0 V (vs Ag/AgCl), well before any solvent oxidation was observed further promoting its use with BP-based systems (**Figure 4.15**). Scans collected in solutions containing precursors for PEDOT:PSS polymerization, on the other hand, demonstrated significant overlap with control scans in electrolyte-only solution at BP electrodes (**Figure 4.15B**). Overlap in the resulting voltammograms suggests competition between electropolymerization and solvent oxidation at the electrode surface. Even though PEDOT:PSS polymerization has been reported at BP electrodes, PANi was selected for device formation going forward due to superior electrochemistry under the employed test conditions.

For both GCE and BP electrodes, PANi and PANi-PSI composites were prepared using modified procedures from previously published methods.^{212,213} Notably, a higher ratio of PSI to monomer solution was employed to offset higher degrees of polymerization expected at the porous carbon surface and, in turn, lower protein densities in the polymer composite. Initial biofilms were first prepared on planar GCEs to characterize the photoactive properties of PSI and PANi at carbon surfaces and to identify the best mediator selection for sustained photocurrent production. All films were polymerized at a constant +1.2 V (vs Ag/AgCl) for 40 s using a 1:4 volume ratio of aniline/HCl monomer solution and either eluted PSI or stock phosphate buffer. Both polymerization solution combinations consumed statistically similar amounts of charge during polymerization, independent of the presence of PSI. Films containing only PANi consumed on average -4.9 ± 0.5 mC while PANi-PSI composites consumed -4.3 ± 0.3 mC. Equal net charges indicates higher concentrations of PSI relative to aniline did not impede polymer growth.

When tested for photoactivity all composites, regardless of the presence of PSI or the identity of the selected mediator, produced anodic photocurrent on glassy carbon electrodes (**Figure 4.16A**).

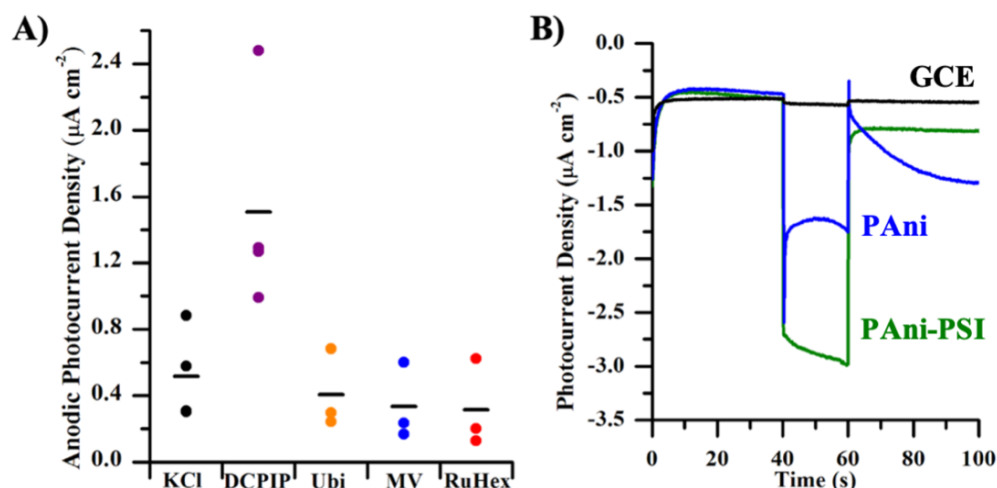


Figure 4.16. Photocurrent Densities of PANi and PANi-PSI Films on Glassy Carbon Electrodes. (A) Photocurrent densities of PANi films prepared in the absence or presence of PSI across multiple tested mediator solutions prepared in 1 M KCl. (B) Resulting current-time curves of PANi and PANi-PSI composites in the presence of 5 mM NaAscb/ 250 μM DCPIP in 1 M KCl.

Despite the inherent photoactivity of PANi, films prepared with PSI produced higher photocurrent densities with all mediators on average due to the synergistic activity between PSI and the surrounding PANi network. Films tested in a 1:20 ratio of 2,6-dichlorophenolindophenol (DCPIP) to sodium ascorbate (NaAscb) outperformed all other chemical mediators for both PSI containing and PANi only devices, which is in agreement with previous results, and as such was the focus for all proceeding analyses.²¹² The addition of PSI into PANi films at planar PCEs increased the photocurrent density from -0.4 to $-1.5 \mu\text{A cm}^{-2}$, representing nearly a 4-fold increase. Aside from higher photocurrent densities, films containing PSI also deviated from traditional diffusional-limited current responses, or Cottrellian behavior, instead increasing to a steady-state current (i_{ss}) (Figure 4.16B). Deviation from Cottrellian behavior suggests a different rate limiting electron transfer in the presence of PSI, likely a slower electron transfer between PSI and the conductive polymer matrix rather than diffusion of fresh mediator into the protein film. This behavior suggests that not only is PSI enhancing the produced photocurrent density of assembled films, but the

surrounding PANi matrix is at work as an integral component in shuttling photoexcited charge from PSI to the lying electrode.

Similar PANi and PANi-PSI composites were prepared on BP₆ electrodes to assess the impact of the high surface area carbon surface on the performance of the prepared photobioanodes. Under the same electropolymerization conditions, polymer growth at BP₆ electrodes exhibited much higher charges than what was observed at planar GCEs, increasing from -4.9 ± 0.5 mC to -480 ± 24 mC for PANi-PSI composites. Higher net charges suggests the more liberal growth of PANi throughout the three-dimensional electrode which was confirmed using SEM (**Figure 4.17**).

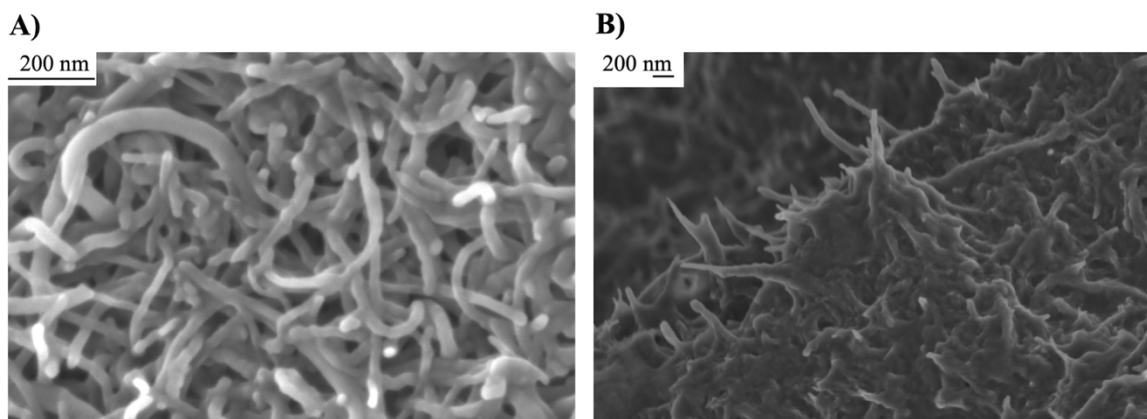


Figure 4.17. SEM Micrographs of Pristine and PANi-Coated BP₆. SEM images of (A) pristine BP₆ and (B) BP₆ following PANi electropolymerization. The grown PANi composite can be seen both filling inter-nanotube void space and coating the surface of nanotubes at the surface of the electrode as reflected in an increased variation of nanotube diameter.

Following polymerization, both the outer wall of surface confined MWCNTs and the inter-nanotube space becomes saturated with PANi. This is evidenced by the increase in relative standard deviation for nanotube diameter post-polymerization, from 14 % at pristine BP₆ to 56 % at PANi-coated BP surfaces. The increase in variance across nanotube diameters is primarily due to non-uniform polymerization throughout the substrate, with the highest degree of polymerization occurring at the solution-exposed surface of the BP electrode and, in some cases, little to no

polymerization occurring at protected nanotubes deep within the substrate. Regardless, partial polymerization at BP electrodes surpasses the extend of polymerization seen at planar electrodes demonstrating its promise as a modifiable high-surface area carbon electrode.

PAni and PAni-PSI composites prepared at BP₆ electrodes were tested under the same conditions as those films prepared at GCE electrodes, with DCPIP/NaAscb as the selected mediator. Increased photocurrent densities of all composites at BP₆ electrodes highlights the beneficial impact of more robust polymerization at high surface area BP composites over planar electrodes (**Figure 4.18**).

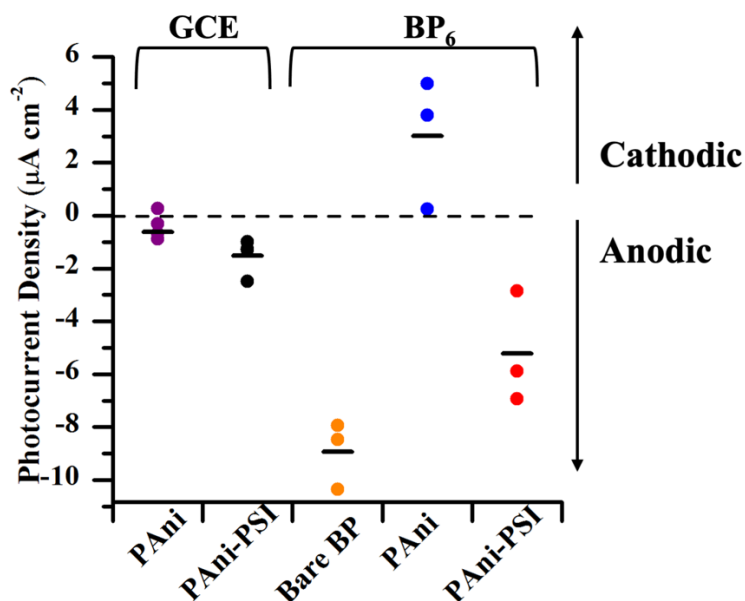


Figure 4.18. Photocurrent Densities of PAni and PAni-PSI Composites At GCE and BP₆ Electrodes. Photocurrent densities normalized to geometric surface area of PAni and PAni-PSI composites prepared at both GCE and BP₆ electrodes. All devices were tested in 1 M KCl electrolyte with 250 µM DCPIP and 5 mM sodium ascorbate. Average photocurrent densities are represented by bold lines in each column and a dashed line marks net zero current flow.

PAni-PSI composites produced, on average, $-5.2 \mu\text{A cm}^{-2}$ at the BP composite compared to $-1.5 \mu\text{A cm}^{-2}$ at planar carbon electrodes, demonstrating a nearly 3.5-fold increase in produced photocurrent density. Regardless of the carbon electrode, the mechanism of photocurrent generation seems to remain the same; photoexcited electrodes are efficiently shuttled from F_B^- to

the working electrode by means of the PANi scaffold while DCPIPH₂, a reduced form of DCPIP, can rapidly replenish P₇₀₀⁺ to sustain photocurrent generation.¹⁵⁷ In all, the substitution of porous, three-dimensional MWCNT substrates did not interfere with mediated photocurrent generation at PSI-PANi composites and shows promise towards developing truly sustainable sources of green energy.

4.2.4. Conclusions & Future Outlooks

The future of porous, three-dimensional, all-carbon electrodes is only limited by the creativity towards which existing carbon materials are processed and applied. Buckypaper serves as a key benchmark in our ability to transition to fully carbon electrodes capable of replacing their conventional inorganic counterparts. Through simple dissolution and filtration steps, high surface area BP electrodes were easily prepared and readily used as electrodes in the development of PSI biohybrid solar cells. The resulting BP electrodes exhibited higher electroactive surface areas 5-fold over planar carbon electrodes, with that value doubling with twice the mass of deposited MWCNTs. The performance of BP electrodes showed strong correlation with supporting electrolyte concentration, with higher (≥ 1 M) amounts leading to favorable kinetics (4.3 ± 0.9 cm s⁻¹) on par with conventional glassy carbon electrodes. Future efforts will seek to better characterize the inherent photoactivity of bare BP electrodes and progress towards implementing BP-based bioelectrodes into flexible, solid-state photovoltaic cells.

5. APPLICATION OF COMMERICALLY AVAILABLE CARBON COMPOSITES IN PHOTOSYSTEM I-BASED ELECTROCHEMICAL CELLS

Chapter 5 moves beyond towards commercially available carbon materials as metal-free electrodes for the assembly of PSI photoelectrochemical cells. The devices created in this chapter show immense promise towards a disposable, scalable biohybrid solar cell for rapid deployment outside of laboratory environments. This research was conducted with the help of Pamela Joy Tabaquin, LTC John Williams, and Elisabeth Woods, as well as Dr. Nsoki Phambu at Tennessee State University.

5.1. Utilizing Toray Paper as a High Surface Area Electrode for Photosystem I-Driven Solar Energy Conversion

5.1.1. Introduction

Rising environmental concerns have sparked interest in diverse sources of renewable, green energy over the past few decades. Biohybrid sources of energy, or those motivated by materials and processes found in nature, have pushed the idea of “green energy” even further by relying on materials with low environmental and economic costs.^{57,214,215} One such material, the photosynthetic protein complex Photosystem I (PSI), has been of particular interest due to its high efficiency and role as a photodiode in nature. These properties have made PSI a promising candidate for use in conventional energy harvesting systems and continue to inspire biohybrid research to this day.^{53,216,217}

The roughly 500 kDa protein is primarily composed of a large array of chlorophyll surrounding an electron-transport chain that begins at a chlorophyll dimer at the center of the protein (P₇₀₀) and travels through a series of phylloquinone mediators before arriving at a terminal iron-sulfur complex (F_B) where it is then accessible for transfer to external charge carriers.^{218,219}

The protein absorbs a wide range of solar energy due to the chlorophyll array and is capable of exciton generation of nearly -1.2 eV with low energy (>600 nm) light. At F_B electrons are transferred with energy of -3.9 eV compared to vacuum, making excitons energetically compatible with numerous materials, ranging from metals to semimetals to semiconductors.^{45,220}

Additional substrate properties of high importance when considering application for sustainable, PSI-based photoelectrochemical cells are geometry and composition. In terms of device impact, three-dimensional geometries have led to enhanced protein loading while low cost and disposable substrates preserve the sustainable nature of produced devices. By minimizing the cost of electrode materials used to prepare PSI-based bioelectrodes, the dispersibility and scalability of this technology will improved to a point where fabrication schemes can be rapidly scaled beyond traditional benchtop dimensions.²²¹⁻²²³ Recent research into electrodes for PSI-based solar energy conversion have focused on implementing porous substrates of materials such as gold, indium-doped tin oxide (ITO), and silicon.^{62,64,224,225} While porous materials can lead to higher photocurrent densities due to enhanced protein loading, the processes needed to convert metals or semiconducting materials to porous geometries are often energy intensive and must be decoupled from protein loading steps to preserve the structure of PSI.

Allotropes of carbon, on the other hand, are inexpensive, diverse in nature, and highly conductive materials compatible with energy-related applications.²²⁶⁻²²⁹ To date, carbon allotropes have only seen limited use in PSI-based biohybrid cells. Gunther et al. demonstrated how graphene could interface with monolayers of PSI for sustained anodic photocurrent production in the presence of diffusible chemical mediators.⁵⁸ Darby et al. expanded upon this work by substituting in reduced graphene oxide to facilitate higher amounts of PSI loading and lead to upwards of 5 $\mu\text{A cm}^{-2}$ of observed photocurrent.⁷⁰ Beyond planar allotropes of carbon, Ciornii et al. utilized

multiwalled carbon nanotubes as a scaffold for PSI immobilization through the use of the redox protein cytochrome C (cyt C) to produce up to $18 \mu\text{A cm}^{-2}$ at biased electrodes.⁶⁸ More recently, Morlock et al. created three-dimensional structures of reduced graphene oxide capable of similar cyt C immobilization of PSI, leading to high photocurrents ($14 \mu\text{A cm}^{-2}$) and high rates of protein turnover ($30 \text{ e}^- \text{ PSI}^{-1} \text{ s}^{-1}$).⁷¹ Despite their successes, past use of carbon allotropes in PSI biohybrid devices still relies on underlying electrode materials, often gold or glassy carbon, negating the benefits of low cost and scalability tied to many carbon materials.

Carbon paper (CP) is a promising candidate for biohybrid photoelectrochemical cells due to inherently high conductivities and surface areas.^{226,228} CP electrodes have been employed as electrodes in whole thylakoid devices, most prominently by Rasmussen et al. through the development of a photo-biocathode capable of highly sensitive herbicide detection from spinach-extracted thylakoids.^{76,230} The inherent high surface area of CP substrates makes them inherently promising electrodes for forming PSI-polymer composites through electropolymerization, which have shown great success in past work.^{48,61,90,212,231} Robinson et al. successfully encapsulated PSI multilayers within a vapor-phase polymerized poly(3,4-ethylenedioxythiophene) (PEDOT) scaffold. This combination of protein and polymer produced composite films resistant to delamination while preserving access to the reaction centers of PSI, as evidenced through higher cathodic photocurrents in the presence of aqueous redox mediator. Gizzie et al. employed a solution of PSI and aniline monomer to rapidly grow photoactive films on planar gold electrodes, showing that the entrapped PSI outperformed more dense multilayers prepared in the absence of polyaniline (PANi).²¹² Yet planar electrodes have shown limitations in electropolymerization processes as diminishing returns are observed beyond critical film thicknesses.²¹² These limiting factors can be overcome by using three-dimensional electrodes that offer significantly higher

electrode surface areas per geometric area, which enables significantly more electropolymerization before desorption limits any additional growth.^{232,233}

In this work, PSI is interfaced with CP electrodes either through physical adsorption or entrapment in conducting polymers formed *in situ*. Following preconditioning, the treated CP electrodes exhibit much improved hydrophilicity, which in turn increases the electrode surface areas and leads to the formation of dense electrode-active layers. The prepared PSI or PSI-polymer films are assembled by using different procedures and tested in the presence of multiple chemical mediators to identify the optimal conditions for devices of this nature. Optimal devices generated up to -220 nA cm^{-2} with the resulting current response reflecting diffusion-limited pathways rather than kinetic limitations at the electrode. The resulting devices demonstrate the full potential of PSI-bioelectrodes as low cost (<1 \$ USD per electrode), metal-free solution to solar energy conversion.

5.1.2. Materials and Methods

Chemicals and Materials

Toray Carbon Paper-060 was purchased from the Fuel Cell Store (fuelcellstore.com) in 20cm x 20cm sheets. The carbon paper sheets were covered with a standard 5% weight wet proofing layer of Teflon. Sheets were 0.19 mm thick, with a porosity of 78% and a resistivity of 80 mΩ cm through the plane as reported by the manufacturer. Hydrochloric acid, sulfuric acid, sodium phosphate monobasic, potassium chloride (Fisher Scientific), 3,4-ethylenedioxythiophene (EDOT), poly(sodium 4-styrenesulfonate) (PSS), aniline, ruthenium hexamine trichloride (RuHex), ferricyanide, ferrocyanide, methyl viologen dichloride (MV), sodium ascorbate, 2,6-dichlorophenolindophenol (DCPIP), 2,3-dimethoxy-5-methyl-p-benzoquinone (ubiquinone-0), Triton X-100 (Sigma Aldrich) were procured and used as received. All deionized water (DI-water)

was purified in-house (Millipore, 18 M Ω cm). Organic baby spinach from Kroger was used as the source of PSI for all experiments.

PSI extraction

The method used to extract PSI has been previously described and is based on the protocols developed by Reeves and Hall.¹⁹⁴ Fresh spinach was macerated in buffer to separate thylakoids from the rest of the leaves. After isolating the thylakoids from the remaining cell debris, Triton X-100 surfactant was added to release PSI from the membrane. The samples were once again centrifuged, and loaded through a hydroxyapatite column, trapping the PSI protein complex. The column was washed with a buffer solution to release the PSI protein under high salt buffers. Samples were then stored in 2 mL aliquots at -80° C and dialyzed to remove surfactants and salts prior to use within experiments. Concentration of PSI aliquots following quantification with Baba's assay was set to 1 μ M prior to sample preparation.⁸⁰

Electrode preparation

Toray carbon paper-060 was cut into rectangular electrodes, approximately 3cm x 2cm. A tag of adhesive copper tape, 3 cm in length was attached to one side of the electrode and used for electrical contact. The electrode was then covered with a PortHole inert electrochemical mask (Gamry Instruments) leaving a circular exposed area of 0.71 cm². Electrodes pretreated with acid were briefly wetted with ethanol, then submerged in 0.1 M sulfuric acid for five minutes. Samples were rinsed with DI-water and allowed to dry. Additional CP electrodes were subjected to flame treatment instead, consisting of 5 second exposures to an open flame, followed by a DI-water rinse and masking analogous to the previously discussed samples.

Electrochemical Measurements

All electronic measurements were conducted using a CH Instruments 660A electrochemical workstation using a three-electrode setup with either modified carbon paper or gold working electrode, a platinum mesh counter electrode and an Ag/AgCl (1M KCl) reference electrode. Cyclic voltammograms (CVs) of 2mM RuHex and ferri/ferrocyanide in electrolyte solution consisting of 1M KCl were obtained using CP electrodes subjected to different treatment methods as the working electrode.

Electropolymerization of polymer or polymer-PSI composites were prepared using a protocol modified from previous works.²³⁴ For poly(3,4-ethylenedioxythiophene) polystyrene sulfonate (PEDOT:PSS) and PEDOT-PSI films, a monomer stock solution containing 0.01 M EDOT and 0.1 M PSS were combined with a 0.02 M phosphate buffer containing 0.001% wt. Triton X-100 with or without PSI. The two solutions, denoted as solution A (EDOT & PSS) and solution B (eluted PSI or phosphate buffer) were combined volumetrically at a 1:4 unless otherwise specified. Films were polymerized either potentiostatically at +1.2 V (vs. Ag/AgCl) for varied times or by cycling the working electrode potential between 0 and +1.3 V at a scan rate of 0.1 V s⁻² for varied numbers of cycles.

Photochronoamperometry (PCA) was performed under applied potentials matching the open circuit potential in either pure electrolyte or mediator solutions containing 2 mM RuHex, 2 mM MV, 5 mM sodium ascorbate/250 μ M DCPIP, or 2mM ubiquinone in 1 M KCl unless otherwise specified. During photocurrent measurements, electrodes were held in the dark for 40 s before illumination using a 100 mW cm⁻² light source (KL 2500 LCD, Micro Optical Solutions, Newburyport, MA) with 20 s followed by another 40 s of darkness.

Electrochemical impedance spectroscopy (EIS) was performed in a solution containing 2 mM RuHex and 1 M KCl using a three-electrode configuration as described above. The potential was oscillated 10 mV above and below the measured OCP (usually around -0.112 V vs Ag/AgCl) from 10,000 Hz to 0.01 Hz. The relevant values were obtained from the resulting data by fitting against a Randles equivalent circuit.

Additional Instrumentation

Scanning electron microscopy of the samples was conducted using a Zeiss Merlin system with a GEMINI II column. Samples were dissected transversely to observe both the surface and cross section of electrodes where applicable.

All contact angle measurements were made using a Rame-Hart goniometer. A single (1 μ L) drop of deionized water was added to each sample for each measurement.

Raman measurements were conducted on a Thermo Scientific DXR confocal Raman microscope. All measurement were made using a 532 nm laser under normal operation parameters.

5.1.3. Results and Discussion

Toray Paper Electrode Preparation

Many carbon paper substrates are prepared for applications as gas permeation membranes and, as such, often come pretreated with a polytetrafluoroethylene (PTFE) coating. This PTFE coating fortifies the CP materials against tear and does not detract from the material's superior conductivity. As a result of this treatment, however, CP surfaces often express hydrophobic or superhydrophobic properties making them incompatible with aqueous electrochemical systems, including PSI-containing solutions. To prepare the electrodes for use in PSI biohybrid devices, CP substrates were pretreated by either chemical oxidation using sulfuric acid or flame treated using a Bunsen burner prior to use in electrochemical applications. By first wetting the substrate with ethanol followed by a brief (5 min) exposure to sulfuric acid, the wettability of the CP substrate

was significantly enhanced as shown by the change in contact angle from $122 \pm 4^\circ$ to $24 \pm 2^\circ$ (Figure 5.1). More extreme surface modification was achieved through flame treatment and the resulting substrate (FT-CP) was fully wettable ($\theta < 5^\circ$) posing no barrier to interaction with PSI-containing solutions. The superior wettability and minimal pretreatment requirements of FT-CP made it the modification method of choice going forward with this work.

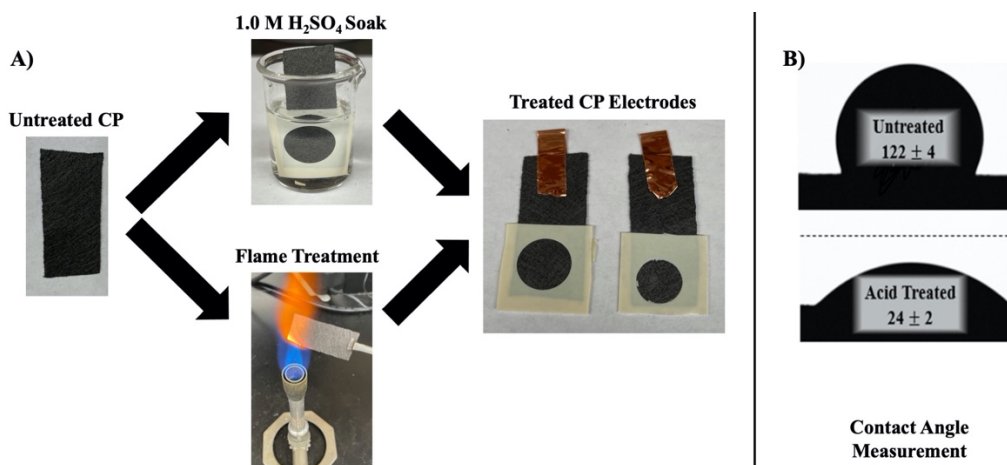


Figure 5.1. Protocol for Oxidative Treatment of Carbon Paper Substrates. (A) Schematic of the oxidative treatment process used on CP substrates. Substrates were first cut to the desired dimensions. Samples to be acid treated were masked first followed by submerging the exposed surface area to a 1.0 M solution of H₂SO₄. (B) Following treatment CP surfaces exhibited superior hydrophilicity as compared to their untreated counterparts.

This improved hydrophilicity is attributed to simultaneously increasing the physical roughness of CP fibers, as evident in SEM images pre and post-treatment, removing the PTFE coating, and increasing functionalized sp³ carbon as evidenced in the resulting Raman spectra (Figure 5.2). Over the two treatment methods applied to CP substrates, the ratio of the D-band ($\sim 1356 \text{ cm}^{-1}$) to the G-band ($\sim 1585 \text{ cm}^{-1}$), comprising of signal from sp³ and sp² carbon, respectively, increased from 0.13 (CP) to 0.60 (FT-CP).

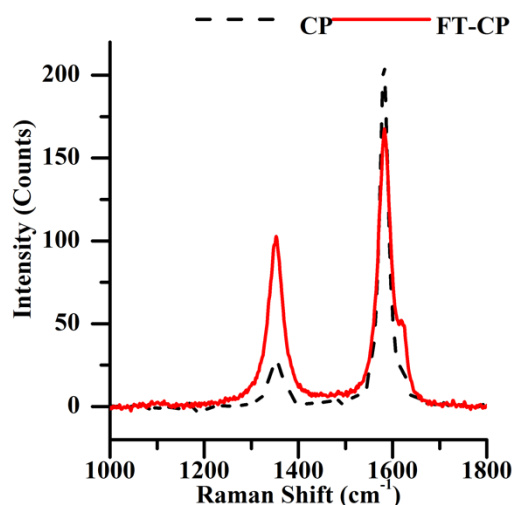


Figure 5.2. Raman Spectra of Untreated CP and FT-CP electrodes. The resulting Raman spectra for untreated CP and flame treated CP electrodes. Following flame treatment, the I_D/I_G increases from 0.13 to 0.60 representing an increase in sp^3 functionalized carbon at the substrate surface.

An increase in sp^3 hybridized carbon at the electrode surface suggests a more polarity, and in turn, an increasingly hydrophilic substrate. This is consistent with the results Choi et al., who sonicated commercial carbon paper in a mixture of concentrated sulfuric and nitric acid to improve the adhesion of polyaniline (PAni) polymerized from aqueous solutions.²³⁵

Electrochemical characterization was used to measure changes in the electroactive surface area, likely a result of improved CP hydrophilicity following surface pretreatment. Cyclic voltammograms of CP substrates treated using different methods show increased faradaic and non-faradaic current responses over those without any form of modification. Increased faradaic responses at CP electrodes that underwent more intense pretreatment demonstrate superior electroactive surface areas when compared to untreated CP or planar glassy carbon (**Figure 5.3**)

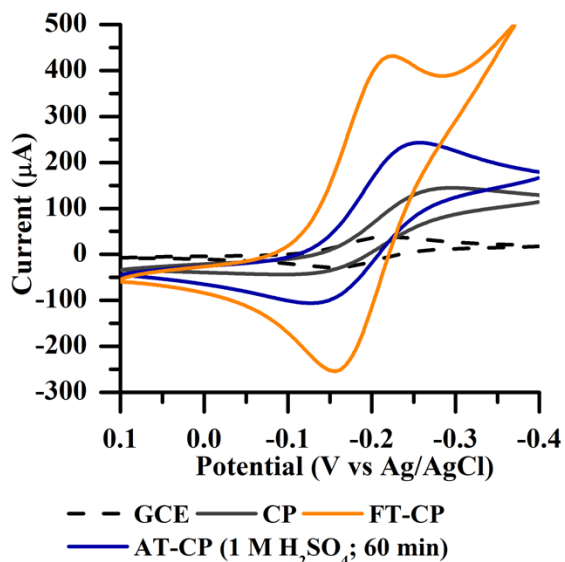


Figure 5.3. Cyclic Voltammetry of Hexamineruthenium at Carbon Paper Electrodes Subjected to Different Pretreatment Methods. Cyclic voltammograms at 100 mVs^{-1} of untreated CP, acid treated CP (treated with $1 \text{ M H}_2\text{SO}_4$ for 60 min), flame-treated CP, and a bare glassy carbon electrode in the presence of 2 mM RuHex and 1 M KCl mediator solution.

Peak currents (i_p) for the FT-CP increased by factors of 6 and 9 for the observed oxidation and 3 and 11 for the observed reduction reaction, with respect to untreated CP and glassy carbon controls. These results, in conjunction with the observed increase in hydrophilicity, suggest that the applied treatment methods allow more of the available surface area of the CP substrates to be accessed by aqueous solutions, promoting their use in energy or sensing applications including use with PSI-based systems.

As with the development of porous metal or semiconducting electrodes, the impact of porosity on electrochemical behavior can often obscure the true surface area. Measuring changes in the capacitive behavior of the electrode can help elucidate the true electrochemically active surface area (ECSA) of a porous material.¹⁷¹ By plotting the increase in non-faradaic current at varying scan rates, the capacitance values for the electrode can be obtained and compared to determine changes in surface area between electrodes of similar composition (**Figure 5.4**). Flame

treatment of the CP substrate resulted in a calculated electroactive area roughly 170 times that of untreated CP.

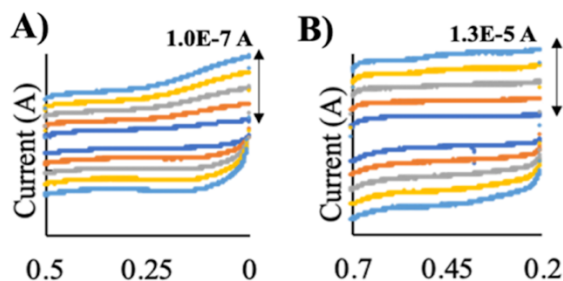


Figure 5.4. Capacitive Cyclic Voltammograms of Carbon Paper Electrodes Following Pretreatment. CVs of CP electrodes in 1 M KCl electrolyte with either (A) no pretreatment, (B) 5 min soak in 0.5 M H₂SO₄, (C) or flame treated for 5 s.

These results support the trends observed with increases in the faradaic current from CP pretreatment. As it stands untreated CP remains largely inaccessible with aqueous solutions detracting from its application in PSI-based biohybrid devices. Through rapid and accessible pretreatment methods, CP electrodes can easily be converted into a usable, high surface area substrate in biohybrid solar energy conversion, serving as a greener alternative to conventional metal electrodes.

PSI Multilayers on Carbon Paper Substrates

In order to demonstrate the viability of CP substrates in PSI-based photoelectrochemical devices, electrodes were coated with varying amounts of PSI using vacuum assisted deposition, a common method for loading PSI or other biological species on electrode surfaces.^{48,61,64} The resulting photocurrents of multilayered devices were anodic regardless of the mediator species (Figure 5.5A).

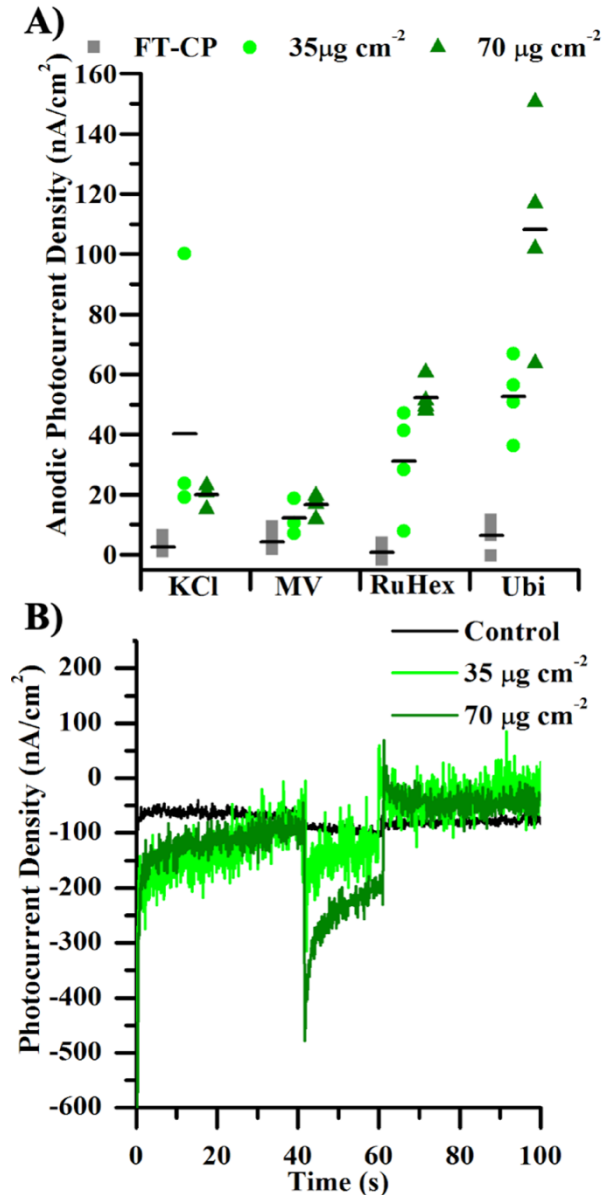


Figure 5.5. Photochronoamperometry of PSI Multilayers on Flame-Treated Carbon Paper. (A) Steady state photocurrent densities of control and PSI multilayers on FT-CP in the presence of various mediators ($n = 4$). Average photocurrent densities are represented by a solid dash. (B) The resulting photocurrent behavior of PSI multilayers under different deposition amounts in the presence of a 2 mM ubiquinone mediator.

The chosen mediators preferentially accept photoexcited electrons from the stromal F_B^- reaction center, resulting in the observed anodic behavior of the assembled devices. Of the mediators tested ubiquinone and RuHex showed the best improvement in photocurrent density, which is attributed to greater overpotentials versus the F_B reaction center of PSI (**Figure 5.6**).

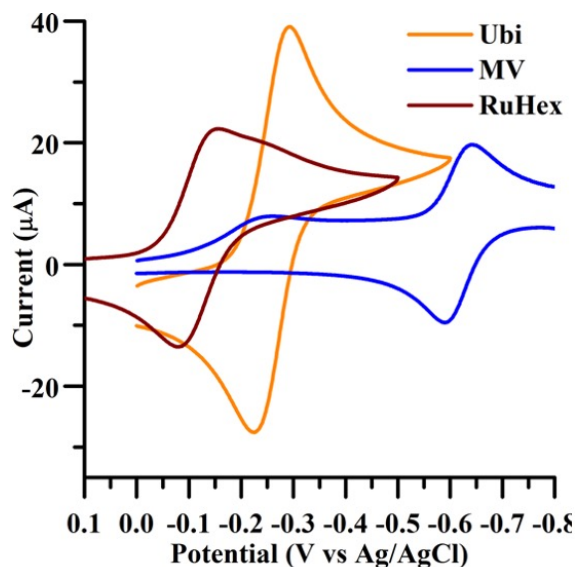


Figure 5.6. Cyclic Voltammetry of Tested Mediators with PSI on Glassy Carbon Electrodes. Representative cyclic voltammograms of 2 mM solutions of ubiquinone, methyl viologen, and ruthenium hexamine.

As expected, there was an inherent photoactivity observed in the control devices; however, the magnitude of this current was negligible ($< 5 \text{ nA cm}^{-2}$) compared to the photocurrent densities produced with PSI-modified electrodes. The shape of the current profile exhibit time-dependent Cottrellian decay, indicating similar behavior of PSI on carbon fiber electrodes to multilayers assembled on conventional inorganic electrodes (**Figure 5.5B**). Furthermore, the time-dependent decay indicates diffusion-limited pathways are responsible for the sustained photocurrent which directly benefit from increased electrode surface areas. Overall, PSI-modified carbon paper electrodes produced significantly higher photocurrent densities than bare CP electrodes. When tested in the presence ubiquinone, the average anodic photocurrent density was $0.11 \text{ } \mu\text{A cm}^{-2}$, a 15-fold enhancement over bare FT-CP ($0.007 \text{ } \mu\text{A cm}^{-2}$). These results validate adequately treated CP substrates as suitable electrodes for PSI, offering a unique, all-carbon alternative to traditional electrode materials.

Rapid Immobilization of PSI on CP Substrates Through Electropolymerization

In order to take advantage of the high surface area of treated CP substrates in PSI-immobilization, electropolymerization was used to entrap PSI within a conducting polymer scaffold formed *in situ*.^{60,234} As a result of their electrochemical growth, polymers used in electropolymerization are often inherently conductive, making them favorable for use in solar cells or other energy-related applications. Beyond PSI entrapment for solar energy conversion, this technique is also useful for the immobilization of enzymes and other sustainable components useful for sensing, energy production, and fuel generation.

To successfully entrap PSI in a conductive, electrochemically polymerized layer on CP or treated CP substrates, all components must first be combined and exposed to sufficient electrical potential needed to drive polymerization. The conductive polymer poly(3,4-ethylenedioxythiophene) polystyrene sulfonate (PEDOT:PSS) was chosen for its optical transparency, low inherent photoactivity, and previously demonstrated success when used in PSI-based devices.^{61,236} In order to verify the occurrence of electropolymerization at the CP surface, substrates subjected to different treatment methods were exposed to both control and monomer-containing solutions and held at a constant potential of +1.2 V (vs Ag/AgCl), and the resulting charge transferred to the solution was compared to evaluate the extent of polymerization (Table 5.1).

Table 5.1. Mean charge delivered (mC) during a 40 s hold of fixed potential +1.2 V (vs Ag/AgCl) in the absence and presence of EDOT:PSS and PSI (n = 3).

	Control	PEDOT:PSS	PEDOT:PSS + PSI
CP	-0.18 ± 0.06	-0.68 ± 0.08	-0.49 ± 0.50
FT-CP	-3.4 ± 0.1	-13 ± 2	-9.8 ± 0.8

All-carbon electrodes produced higher net charges in runs containing EDOT and PSS when compared to exposure to pure electrolyte solution, indicating the occurrence of new faradaic processes tied to polymer formation. FT-CP consumed a 19-fold higher net charge over untreated CP indicating more extensive polymerization at hydrophilic surfaces. SEM images also confirm the more liberal growth of polymer off treated CP surfaces compared to unmodified carbon paper (Figure 5.7). When polymerized in the presence of PSI, the total charge passed during polymerization remained largely unchanged, suggesting the presence of PSI protein did not significantly impede the growth of PEDOT:PSS.

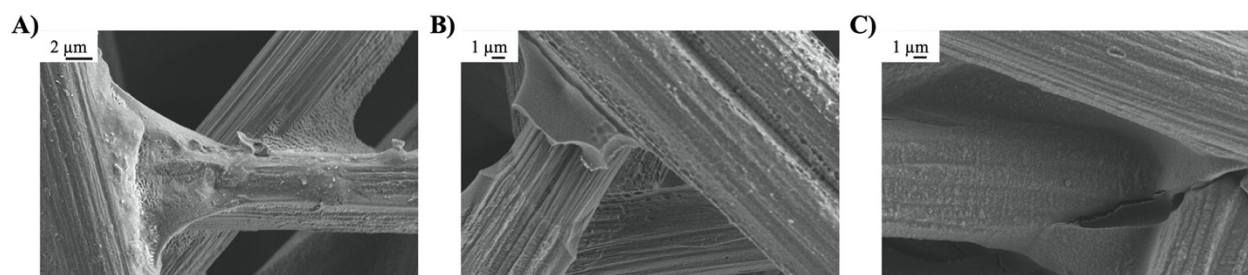


Figure 5.7. SEM Micrographs of CP, FT-CP, and FT-CP Following PEDOT:PSS Electropolymerization. SEM micrographs of (A) untreated CP and (B) FT-CP electrodes. (C) FT-CP electrodes were then subjected to electropolymerization under potentiostatic conditions for 40 s using a 4:1 ratio of EDOT:PSS solution to stock elution buffer and imaged.

Protein films were formed using an electropolymerization solution composed of a 1:4 ratio of precursor solution (0.01 M EDOT and 0.1 M PSS) to extracted PSI solution, with control films substituting unmodified elution buffer for PSI extract. Higher ratios of PSI to monomer than what have been used previously on planar electrodes were necessary to improve protein loading in the rapidly forming films due to higher surface area at treated carbon surfaces. Devices were tested in mediator solutions of 1 M KCl electrolyte. High electrolyte concentrations were used to improve the overall performance of the devices, as lower concentrations of KCl lead to drifting dark photocurrents (i_{dark}). The drifting i_{dark} most likely stems from the high charging current associated

with high surface area, highly capacitive materials and should be accounted for when applying these materials to electrochemical systems.²⁰²

Across the mediators tested, PSI-polymer films produced anodic photocurrent, similar to the results observed with vacuum deposited protein. Photocurrent densities were calculated by taking the difference between average light photocurrent densities (J_{light}) and dark photocurrent densities (J_{dark}) before and after light exposure. Across most mediators, composites containing PSI outperformed PEDOT:PSS films devices fabricated on flame treated CP (**Figure 5.8**).

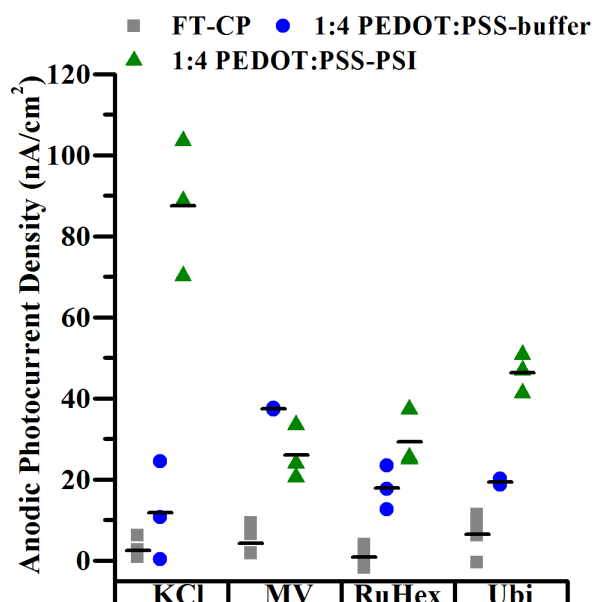


Figure 5.8. Photocurrent Densities of PEDOT:PSS-PSI Films on Flame-Treated Carbon Paper. Photocurrent densities of composites formed on flame-treated CP substrates under potentiostatic conditions of +1.2 V for 40s in 1 M KCl with no mediator, 2mM MV, 2 mM RuHex, 2 mM ubiquinone ($n = 3$). Average photocurrent density values are represented by a solid dash.

The best performance was seen in pure electrolyte solution, suggesting dissolved oxygen is effective at shuttling charge from the composite films to the underlying carbon electrode, with PSI-containing devices exhibiting a 7-fold increase in current density (-12 nA cm^{-2} vs -87 nA cm^{-2}). Relying on dissolved oxygen is not ideal for sustained photocurrent generation, however, as the

formation of reactive oxygen species (ROS) can lead to protein and polymer degradation.²³⁷ The next best performance was observed in the presence of ubiquinone. Ubiquinone and other quinone derivatives are known to be natural electron acceptors in aerobic photosynthesis making them suitable candidates for PSI-based biohybrid devices.

In order to optimize PEDOT:PSS-PSI composites on FT-CP substrates, multiple polymerization conditions were tested to maximize polymer growth and PSI entrapment. Using a 1:4 volumetric ratio of monomer solution to PSI solution, different times were tested under potentiostatic growth conditions. Potential sweep-based polymerization methods were also tested to promote protein migration into the actively growing films. All photocurrent measurements were tested using a 2 mM ubiquinone solution in 1 M KCl electrolyte (**Figure 5.9**).

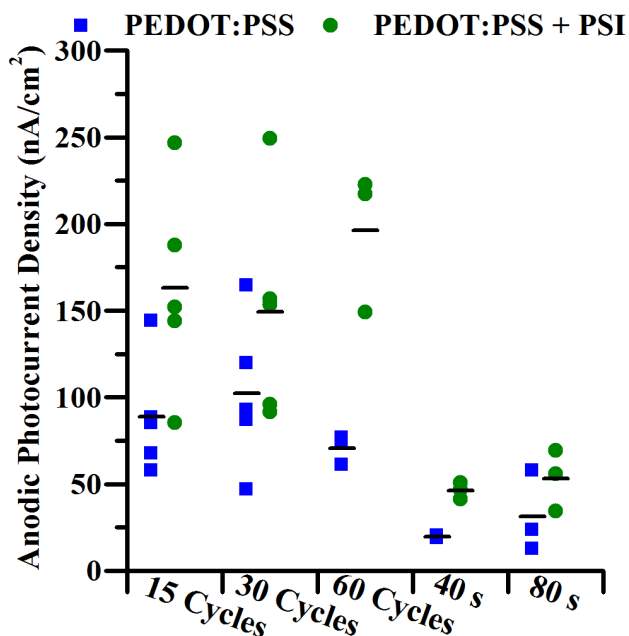


Figure 5.9. Photocurrent Densities of PEDOT:PSS-PSI Composites Fabricated Using Different Electrochemical Conditions. Photocurrent densities of PEDOT and PEDOT-PSI composites on FT-CP. Composites were formed under both potentiostatic conditions at varying times or by potential sweep methods (100 mV s^{-1} scan rate from 0 V to +1.3 V for a varied number of cycles). All films were tested with a 2 mM ubiquinone/1 M KCl. Average photocurrent density values are represented by a solid dash. An $n = 3$ was used for all potentiostatic conditions and 60-cycles devices while $n = 5$ for 15 and 30-cycle devices.

Of the tested devices, increasing the polymerization time for composites formed under potentiostatic conditions lead to more photoactive films, albeit with more variability in performance. Polymerizing PEDOT:PSS using cyclic voltammetry methods seemed to have a more pronounced impact on the quality of protein-polymer composite. The net charge consumed in polymerization through cyclic voltammetry was greater than that tested for potentiostatic growth, indicating more polymer was formed at the electrode surface. Yet these films also demonstrated the greatest improvement in mediated photocurrent density in the presence of PSI at high cycle, resulting in an increase from -67 nA cm^{-2} to -220 nA cm^{-2} or a nearly 4-fold increase. These values are comparable to PSI multilayers assembled on graphene and graphene oxide coated substrates; however, the methods proposed in this study can be more readily applied in large scale device assembly applications and are better suited for distributable energy production.^{58,70}

Raid Scaling of Produced PEDOT:PSS-PSI Composites on Carbon Paper Substrates

One of the advantages of the chosen carbon paper material is its commercial availability in a wide range of dimensions. Since the applied treatment methods, primarily flame treatment, are easily applied to substrates of any dimensions, large scale devices were prepared and tested to investigate their viability. FT-CP substrates were prepared using normal procedures, with exposed working areas of either 1, 4, or 9 cm² (**Figure 5.10A**). Cyclic voltammetry was then used to verify proportional scaling of the electrically accessible surface area in a manner similar to when pretreatment methods were compared. From the resulting voltammograms, the faradaic current response did scale with the device dimensions, with both anodic and cathodic peak currents for the oxidation and reduction of RuHex, respectively, increasing by a factor of 13.5 (**Figure 5.10B**).

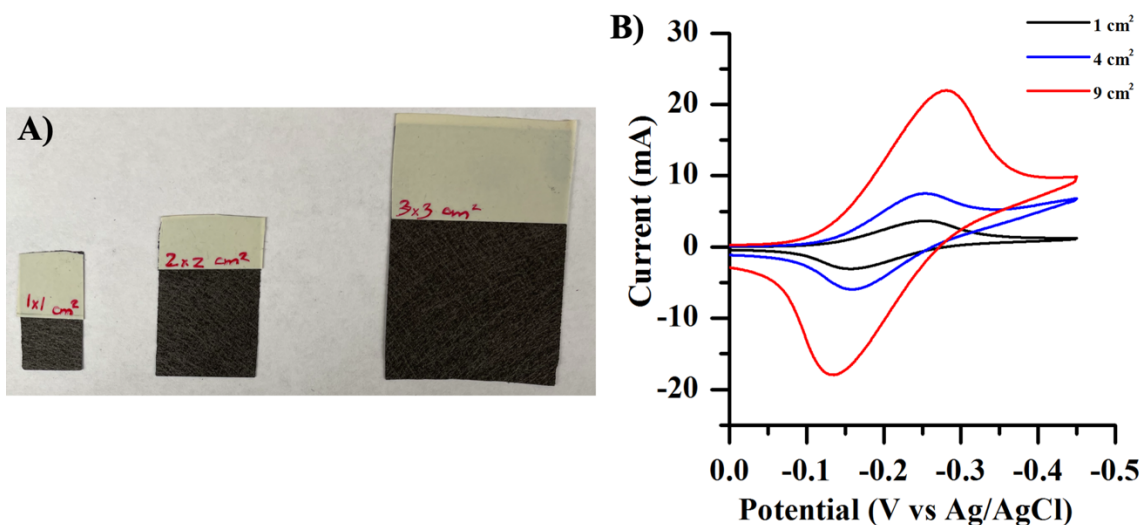


Figure 5.10. Upscaling of PSI-Devices Using Carbon Paper Electrodes. (A) Image of the two sizes of devices tested for upscaling proof of concept following flame treatment and masking. The two devices exhibit different exposed working areas of 1 cm² (left), 4 cm² (middle) and 9 cm² (right). (B) Cyclic voltammograms of 2 mM [Ru(NH₃)₆]^{3+/2+} mediator in 1 M KCl.

Initial potentiostatic polymerization at substrates with increased geometric surface areas followed similar scaling as seen with faradaic detection of RuHex at FT-CP electrodes of different exposed working areas. As a preliminary test, PEDOT:PSS was polymerized using a potential sweep method for 30 cycles at each electrode (Table 5.2).

Table 5.2. Peak currents and total polymerization charges delivered for FT-CP devices (n = 3) assembled to different geometric surface areas.

S.A.	Peak Current (a/c) (mA)	Charge (C)
1 cm ²	-1.8 ± 0.5/2.9 ± 0.5	-0.19
4 cm ²	-4 ± 1/8 ± 1 2.1/2.8	-0.49 ± 0.03 2.5
9 cm ²	-12 ± 3/20 ± 3 2.9/2.4	-1.3 ± 0.2 2.3

The quantity of charge consumed as well as the peak currents from voltametric analysis of RuHex scaled well with geometric area, as expected. When tested for photoactivity, however, the

photocurrent generated decreased with increasing electrode surface area. The diminished current is likely the result of higher amounts of uncoated carbon fiber exposed to solution as electropolymerization processes seemed to localize around the edges of larger electrodes.

Despite setbacks in efforts towards upscaled device geometries, the FT-CP electrodes open the door to inexpensive PSI-driven energy production. Based on current protocols, the total cost of materials from PSI extraction to FT-CP device testing lies at just below 1 USD. For comparison, the same class PSI bioelectrode prepared at a gold electrode would cost upwards of 3 USD per electrode. The limiting cost in device assembly when using FT-CP electrodes becomes the PSI extraction itself, in particular the quantity of hydroxyapatite resin used for purification of the protein. By optimizing the extraction procedure to use less hydroxyapatite or a different resin altogether, the total cost of PSI photoelectrochemical cells based on FT-CP electrodes can be further reduced adding to the accessibility of the technology.

5.1.4. Conclusions & Future Outlooks

Carbon paper was successfully utilized as a green, low-cost alternative to inorganic electrodes in conventional PSI-based biohybrid photoelectrochemical cells for mediator-driven solar energy conversion. Prior to use, it is critical to pretreat CP substrates to maximize the accessible surface area through both the removal of any protective coating and the creation of hydrophilic moieties on the fibers surface. Simple treatments such as soaking in acid solutions or exposure to an open flame proved effective, with flame treatment improving the electrochemically active surface area by a factor of roughly 10 for faradaic processes. PSI vacuum deposited on flame treated CP produced anodic photocurrent ($0.11 \mu\text{A cm}^{-2}$) using a ubiquinone mediator. More stable photoactive composites can be formed by entrapping PSI within an electropolymerized composite, which capitalizes on the improved CP electrode surface area following pretreatment. Using cyclic voltammetry as a polymerization method, the produced photocurrent densities could be pushed to

0.22 $\mu\text{A cm}^{-2}$ under the conditions tested in this study. These methods can be readily employed to upscale the size of the produced photoactive electrode as the treatment methods and electrochemical processes are susceptible scaling beyond benchtop dimensions.

Future directions for this project should be directed towards optimizing the performance of upscaled devices, allowing CP-based PSI bioelectrodes to transcend conventional benchtop testing dimensions. For photoelectrochemical cells scaled surface areas should allow devices to produce relevant current densities (mA cm^{-2}) with ease provided sufficient light dispersion and adequate testing apparatus are used. Poor currents at upscaled devices likely stems from the higher amount of exposed carbon surface which comes with larger dimensions. This hypothesis is supported by the non-uniform coating of FT-CP electrodes subjected to varying lengths of electropolymerization. By ensuring polymerization is driven to completion and total coating of substrate is achieved, a more homogeneous system can be established which should allow for more consistent performance. Mastering the performance of CP-based PSI electrodes at larger dimensions will also aid in the fabrication of solid-state photovoltaics assembled with PSI-polymer composites further pushing the viability of this technology as a truly green, deployable, and sustainable source of renewable energy.

6. CONCLUSION & FUTURE DIRECTIONS

6.1. Summary

This dissertation has focused on the preparation and processing of a small sampling of carbon-based materials as prospective components for PSI-based biohybrid solar cells. Previous work in the field has improved the viability of biohybrid devices through a host of research efforts from electrode engineering to protein functionalization. Some of the more recent improvements in PSI-related research include engineering redox molecules for targeted electron transport, designing porous or three-dimensional electrodes capable of higher degrees of protein loading, and exploring new polymeric materials to immobilize and construct photoactive electrodes, to name a few.^{48,65,71,157} Despite continual advances in the field, little effort has been focused towards capitalizing on the low-resource nature of PSI, a significant distinguishing factor between biohybrid materials and traditional light harvesting complexes. The work presented in this dissertation targets the simultaneous improvement of biohybrid device performance while attempting to minimize devices cost and environmental impact by exploring the application of carbon-based materials into PSI-modified photoelectrochemical cells.

In Chapter 3, the synthesis and characterization of carbon dots was discussed. The goal of this project is to leverage the high customizability of carbon materials to engineer discrete batches of particles to serve different roles within biohybrid devices. As presented in this work, a 1:2 doping ratio of nitrogen to carbon creates particles which are electrochemically oxidized at +0.35 V vs Ag/AgCl which is energetically aligned with the luminal P₇₀₀ reaction center of PSI. Likewise, all synthesized carbon dots energetically aligned with F_B in the reduced state suggesting functionality as electron transport materials. Further optical characterization (luminescence assays, FRET analysis) and electrochemical (solid-state electrochemistry of CD films) of these

heterogeneous electron transfer reactions would help push this material to its first use with PSI-biohybrid devices.

Chapter 4 explored two applications of MWCNTs in PSI photo-bioelectrodes. The first application explored how MWCNT films could be rapidly applied to substrates as high surface area extensions of the electrode. Furthermore, the surface area enhancement of resulting devices w Following the deposition of oxidized MWCNTs on gold electrodes, the mediated anodic steady-state photocurrent of PSI multilayers was increased from $0.24 \mu\text{A cm}^{-2}$ to $0.64 \mu\text{A cm}^{-2}$, or roughly by a factor of 2.5. This enhancement of photocurrent demonstrates the prospect of MWCNTs as an inexpensive carbon material capable of supporting PSI-multilayers within mediated photoelectrochemical cells.

The second application discussed in Chapter 4 explored the fabrication of free-standing composites of MWCNTs, or buckypaper, and their sequential use as electrodes in the fabrication and evaluation of photoactive PSI-polymer composites. Unlike previously tested carbon electrodes, buckypaper served as flexible, metal-free, high surface area electrodes, the likes of which have not been applied to PSI systems. While the variance between BP electrodes increased over planar electrodes, the overall surface area was immensely improved by a factor of nearly 20, from 0.07 cm^2 to 1.54 cm^2 . The higher electrode surface area led to the growth of denser PSI-PAni composites which significantly increased the produced photocurrent densities from $-1.5 \mu\text{A cm}^{-2}$ to $-5.2 \mu\text{A cm}^{-2}$.

Chapter 5 moved beyond synthesized materials and instead explored commercially available carbon fiber substrates as three-dimensional electrodes. The morphology of carbon fiber electrodes warrants their use with PSI-polymer composites, much like buckypaper. In addition to favorable costs, devices assembled on CP electrodes can be rapidly assembled and are inherently

disposable due to the nature of the materials used in device assembly. Assembled devices using PSI and the conductive polymer PEDOT:PSS generated up to $0.22 \mu\text{A cm}^{-2}$ when tested in the presence of ubiquinone. These results demonstrate the potential of CP materials as metal-free electrode which each device costing under 1 USD, nearly a fourth of the cost of bioelectrodes prepared at gold electrodes.

6.2. Outlook

The field of PSI-based biohybrid solar cells has grown immensely from its ambitious beginning with efforts towards the platinization of whole chloroplasts.⁴² Thanks to advances in parallel fields like materials science, and nanoscale engineering, the standings of PSI-biohybrid solar cells within global efforts towards improving solar energy conversion look bright with improvements in the availability and processability of organic and inorganic materials.^{35,44} Yet the potential of PSI systems to go truly “green” and transition into devices free of precious earth metals or high processing and environmental costs is dependent on our increased reliance on organic electrode materials, with allotropes carbon being the most approaching material in this class to date. Carbon materials find themselves in the unique position to simultaneously boost device performance while minimizing costs tied to device fabrication. Feasibly a single allotrope of carbon could achieve both goals; however, one could also imagine designing a device leveraging multiple carbon-based materials for targeted improvements of different properties within a PSI-based solar cell.

Reflecting on the process of photosynthesis and what makes PSI an attractive material for solar energy conversion, the photoexcitation of electrons within the PSI protein complex is highly efficient (approaching near perfect internal quantum efficiency) and results in a high energy exciton of nearly 1 eV of energy at the F_B site. While PSI has been used as a sensitizer to TiO_2

cells, past research has struggled with preserving the high internal efficiency and photovoltage associated with PSI outside of its native environment.^{14,47} Carbon dots, as described in Chapter 3, find themselves in a position to target charge transfer to and from P_{700}^+ and F_B^- , respectively, due to their tunable redox potentials, favorable solubility, and relative size compared to the native metalloproteins which contribute to photosynthesis (**Figure 6.1**).

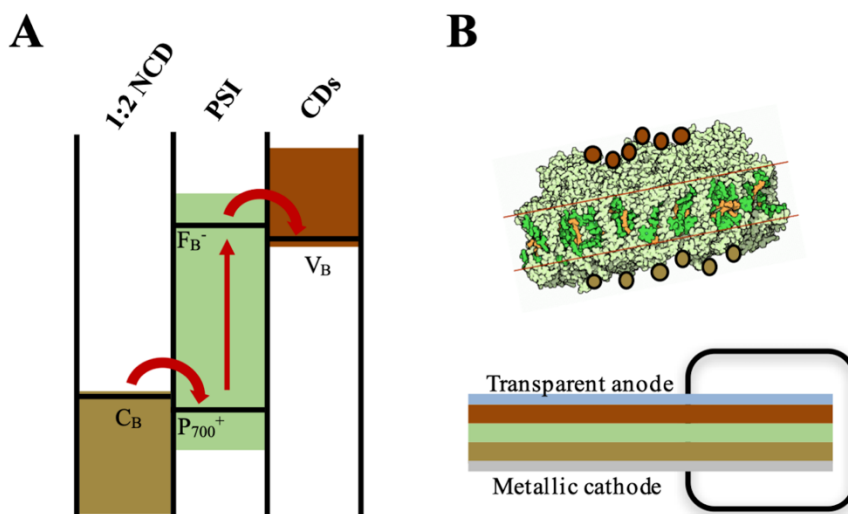


Figure 6.1. Proposed Use of CDs and Doped CDs as Electron and Hole Transport Materials in PSI Photovoltaics. (A) Generalized band diagram reflecting the proposed incorporation of CD materials as finely tuned hole and electron acceptors for PSI proteins. (B, top) Model of side-selective attachment of 1:2 NCD and undoped CDs to individual PSI proteins. (B, bottom) Proposed device architecture incorporating CD as transport materials in a preexisting PSI device.

Carbon dots, either as modifiers to composite layers interfaced with PSI multilayers or directly conjugated to the surface of PSI, could be incorporated into existing solid-state devices with the goal of improving device performance by harnessing more of the inherent energy which draws researchers to the photosystem protein complexes. Alternatively, the luminescence properties of CDs also exhibit dopant-dependance and, as such, could be tuned to align with the optimal wavelengths of light for PSI absorbance to expand the usable range of light for biohybrid devices.⁹⁶

Expanding to the macroscopic level, carbon-based electrodes are readily available to improve PSI performance within biohybrid devices while retaining economic and environmental advantages tied to their metal-free nature. Chapters 4 and 5 serve as proof-of-concept records for carbon composites as working electrodes within PSI biohybrid solar cells but leave much room for optimization and improvement. While the BP electrodes tested within this dissertation were biopsied fractions only 6 mm in diameter and mounted on glassy carbon disk electrodes, BP substrates post-filtration can serve as freestanding electrodes. Using vacuum-assisted filtration, the dimensions of the resulting BP composite are only limited by the diameter of the filtration apparatus used, as well as the diameter of the filter paper. By increasing the dimensions of both components, the geometric surface area the prepared BP will be adequately scaled, as will the electroactive surface area. These largescale, flexible, BP electrodes would be ideal for creating unique PSI bioelectrodes capable of forming robust, flexible solar cells.

In a similar manner, carbon paper-based PSI bioelectrodes can also be rapidly scaled beyond typical testing dimensions ($<1\text{ cm}^2$) with the added advantage of commercial availability. Initial testing on large scale (4 cm^2 and 9 cm^2) in Chapter 5 revealed proportional increases to measured faradaic current and charge delivered during electropolymerization experiments. Yet when tested for photoactivity, large-scale electrodes performed systematically worse than devices prepared at conventional dimensions (0.71 cm^2) under the tested preparation conditions. The working hypothesis for this decrease in performance is that larger electrodes require more time to sufficiently coat the entirety of the electrode working area, which is supported by visual changes in FT-CP electrodes subjected to different durations of electropolymerization (**Figure 6.2**).

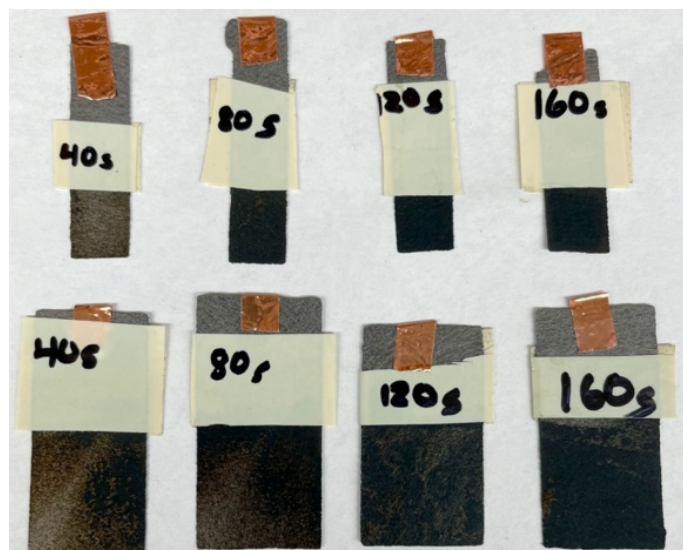


Figure 6.2. Photograph of PANi Growth at FT-CP Electrodes of Different Geometric Dimensions. Electrodes were prepared in a polymerization solution consisting of a 1:4 volume ratio of aniline solution and phosphate buffer. Electropolymerization was performed at a set +1.3 V (vs Ag/AgCl) for varied time. At larger dimensions, longer polymerization times are required to achieve complete, uniform films of PANi throughout the CP electrode.

Once a protocol for fabricating large-scale electrodes has been established, the dimensions of PSI electrodes prepared at CP substrates can be rapidly scaled by using high volume electrochemical cells. Under these conditions, bioelectrodes upwards of 100s of cm² can be rapidly prepared with modest increases to cost-per-device, limited only by the quantity of PSI used during device preparation.

Carbon materials will provide accessible pathways to PSI devices boasting dimensions not previously seen in the field, which when coupled with their overall low cost makes them competitive with biohybrid cells made with inorganic components. In a similar manner, the low cost-per-device of carbon-based PSI devices makes the technology discussed in this dissertation approachable in low resource settings promoting their use in future energy harvesting applications (Figure 6.3.).

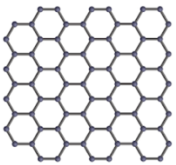
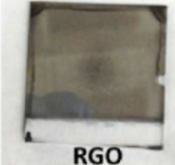
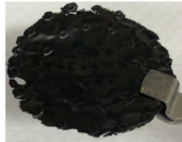
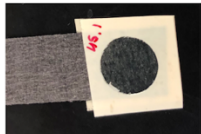
				
Material	Graphene¹	rGraphene Oxide²	Buckypaper	Carbon Paper
Preparation	- CVD growth - Attachment to glass	-Spin coat onto glass -Reduce with hydrazine	-Vacuum-assisted filtration	-Flame-treatment of purchased product
Surface Area Enhancement	GSA x 1 cm ²	GSA x 1 cm ²	GSA x 5.5 cm ²	GSA x 3.3 cm ²
Photocurrent Density	0.5 μA cm ⁻²	5.0 μA cm ⁻²	5.2 μA cm ⁻²	0.22 μA cm ⁻²
Cost	9.80 USD cm ⁻²	1.09 USD cm ⁻²	2.05 USD cm ⁻²	0.09 USD cm ⁻²

Figure 6.3. Comparison of Carbon Materials Prepared In Recent Years. A comparison of metrics tied to past published carbon electrode materials and those discussed in this dissertation. Metrics include the required preparation steps, the relative electroactive surface area with respect to exposed geometric area, the average photocurrent density reported at the electrode surface, and the average cost of electrode per cm² as estimated based on prices obtained from Sigma Aldrich. ¹Metrics for graphene electrode were calculated based on the reported results in **Reference 58**. ²Metrics for reduced graphene oxide (rGraphene Oxide) electrodes were calculated based on reported results from **Reference 70**. The figure for rGraphene Oxide was reprinted with permission from Darby, E, et al. Photoactive Films of Photosystem I on Transparent Reduced Graphene Oxide Electrodes. *Langmuir* 2014, 30 (29), 8990-8994. Copyright 2021 American Chemical Society.

Examples of environments which can prosper from access to low-cost renewable energy include rural settings with minimal infrastructure in place for energy dispersion, and educational settings like classrooms or museums which help disseminate the benefits of renewable energy to all people. Through these creative applications of biohybrid renewable energy, as well as those to come, PSI will continue to serve the planet as it has for all of history.

7. REFERENCES

1. Kahan, A. *EIA projects nearly 50% increase in the world energy usage by 2050, led by growth in Asia*; U.S. Energy and Information Administration: 09/24/2019, 2019.
2. Omer, A. M., Energy use and environmental impacts: A general review. *Journal of Renewable and Sustainable Energy* **2009**, *1* (5), 053101.
3. Kabir, E.; Kumar, P.; Kumar, S.; Adelodun, A. A.; Kim, K.-H., Solar energy: Potential and future prospects. *Renewable and Sustainable Energy Reviews* **2018**, *82*, 894-900.
4. Spanggaard, H.; Krebs, F. C., A brief history of the development of organic and polymeric photovoltaics. *Solar Energy Materials and Solar Cells* **2004**, *83* (2), 125-146.
5. Gratzel, M., Photoelectrochemical cells. *Nature (London, U. K.)* **2001**, *414* (6861), 338-344.
6. Yong, Y.; Cheng, X.; Bao, T.; Zu, M.; Yan, L.; Yin, W.; Ge, C.; Wang, D.; Gu, Z.; Zhao, Y., Tungsten Sulfide Quantum Dots as Multifunctional Nanotheranostics for In Vivo Dual-Modal Image-Guided Photothermal/Radiotherapy Synergistic Therapy. *ACS Nano* **2015**, *9* (12), 12451-12463.
7. Link, S.; El-Sayed, M. A., Shape and size dependence of radiative, non-radiative and photothermal properties of gold nanocrystals. *Int. Rev. Phys. Chem.* **2000**, *19* (3), 409-453.
8. Jain, P. K.; Huang, X.; El-Sayed, I. H.; El-Sayed, M. A., Noble Metals on the Nanoscale: Optical and Photothermal Properties and Some Applications in Imaging, Sensing, Biology, and Medicine. *Acc. Chem. Res.* **2008**, *41* (12), 1578-1586.
9. Zhou, H.; Chen, Q.; Li, G.; Luo, S.; Song, T.-b.; Duan, H.-S.; Hong, Z.; You, J.; Liu, Y.; Yang, Y., Interface engineering of highly efficient perovskite solar cells. *Science* **2014**, *345* (6196), 542.

10. Correa-Baena, J.-P.; Saliba, M.; Buonassisi, T.; Grätzel, M.; Abate, A.; Tress, W.; Hagfeldt, A., Promises and challenges of perovskite solar cells. *Science* **2017**, *358* (6364), 739.
11. Han, S.-Y.; Akhtar, M. S.; Jung, I.; Yang, O. B., ZnO nanoflakes nanomaterials via hydrothermal process for dye sensitized solar cells. *Materials Letters* **2018**, *230*, 92-95.
12. Chen, X.; Mao, S. S., Titanium Dioxide Nanomaterials: Synthesis, Properties, Modifications, and Applications. *Chem. Rev. (Washington, DC, U. S.)* **2007**, *107* (7), 2891-2959.
13. Senthil, T. S.; Muthukumarasamy, N.; Velauthapillai, D.; Agilan, S.; Thambidurai, M.; Balasundaraprabhu, R., Natural dye (cyanidin 3-O-glucoside) sensitized nanocrystalline TiO₂ solar cell fabricated using liquid electrolyte/quasi-solid-state polymer electrolyte. *Renewable Energy* **2011**, *36* (9), 2484-2488.
14. Bach, U.; Lupo, D.; Comte, P.; Moser, J. E.; Weissortel, F.; Salbeck, J.; Spreitzer, H.; Grätzel, M., Solid-state dye-sensitized mesoporous TiO₂ solar cells with high photon-to-electron conversion efficiencies. *Nature (London)* **1998**, *395* (6702), 583-585.
15. Li, H.; Li, S.; Wang, Y.; Sarvari, H.; Zhang, P.; Wang, M.; Chen, Z., A modified sequential deposition method for fabrication of perovskite solar cells. *Solar Energy* **2016**, *126*, 243-251.
16. Green, M. A.; Ho-Baillie, A.; Snaith, H. J., The emergence of perovskite solar cells. *Nat. Photonics* **2014**, *8* (7), 506-514.
17. Nozik, A. J., Quantum dot solar cells. *Physica E (Amsterdam, Neth.)* **2002**, *14* (1-2), 115-120.
18. Kamat, P. V., Quantum Dot Solar Cells. Semiconductor Nanocrystals as Light Harvesters. *J. Phys. Chem. C* **2008**, *112* (48), 18737-18753.

19. Jean, J.; Woodhouse, M.; Bulović, V., Accelerating Photovoltaic Market Entry with Module Replacement. *Joule* **2019**, *3* (11), 2824-2841.
20. Krebs, F. C., Fabrication and processing of polymer solar cells: A review of printing and coating techniques. *Solar Energy Materials and Solar Cells* **2009**, *93* (4), 394-412.
21. Thompson, B. C.; Frechet, J. M. J., Organic photovoltaics - Polymer-fullerene composite solar cells. *Angewandte Chemie-International Edition* **2008**, *47* (1), 58-77.
22. Musazade, E.; Voloshin, R.; Brady, N.; Mondal, J.; Atashova, S.; Zharmukhamedov, S. K.; Huseynova, I.; Ramakrishna, S.; Najafpour, M. M.; Sheng, J. R.; Bruce, B. D.; Allakhverdiev, S. I., Biohybrid solar cells: Fundamentals, progress, and challenges. *Journal of Photochemistry and Photobiology C-Photochemistry Reviews* **2018**, *35*, 134-156.
23. Vidal, R.; Alberola-Borras, J. A.; Habisreutinger, S. N.; Gimeno-Molina, J. L.; Moore, D. T.; Schloemer, T. H.; Mora-Sero, I.; Berry, J. J.; Luther, J. M., Assessing health and environmental impacts of solvents for producing perovskite solar cells. *Nature Sustainability* **2021**, *4* (3), 277-285.
24. Goetz, K. P.; Taylor, A. D.; Hofstetter, Y. J.; Vaynzof, Y., Sustainability in Perovskite Solar Cells. *Acs Appl Mater Inter* **2021**, *13* (1), 1-17.
25. Mariotti, N.; Bonomo, M.; Fagiolari, L.; Barbero, N.; Gerbaldi, C.; Bella, F.; Barolo, C., Recent advances in eco-friendly and cost-effective materials towards sustainable dye-sensitized solar cells. *Green Chemistry* **2020**, *22* (21), 7168-7218.
26. Sánchez, S.; Vallés-Pelarda, M.; Alberola-Borràs, J.-A.; Vidal, R.; Jerónimo-Rendón, J. J.; Saliba, M.; Boix, P. P.; Mora-Seró, I., Flash infrared annealing as a cost-effective and low environmental impact processing method for planar perovskite solar cells. *Materials Today* **2019**, *31*, 39-46.

27. Peng, J.; Lu, L.; Yang, H., Review on life cycle assessment of energy payback and greenhouse gas emission of solar photovoltaic systems. *Renewable and Sustainable Energy Reviews* **2013**, *19*, 255-274.
28. Günes, S.; Neugebauer, H.; Sariciftci, N. S., Conjugated Polymer-Based Organic Solar Cells. *Chemical Reviews* **2007**, *107* (4), 1324-1338.
29. Li, G.; Shrotriya, V.; Huang, J.; Yao, Y.; Moriarty, T.; Emery, K.; Yang, Y., High-efficiency solution processable polymer photovoltaic cells by self-organization of polymer blends. *Nature Materials* **2005**, *4* (11), 864-868.
30. Darling, S. B.; You, F. Q., The case for organic photovoltaics. *Rsc Adv* **2013**, *3* (39), 17633-17648.
31. Emmott, C. J. M.; Urbina, A.; Nelson, J., Environmental and economic assessment of ITO-free electrodes for organic solar cells. *Solar Energy Materials and Solar Cells* **2012**, *97*, 14-21.
32. Azzopardi, B.; Emmott, C. J. M.; Urbina, A.; Krebs, F. C.; Mutale, J.; Nelson, J., Economic assessment of solar electricity production from organic-based photovoltaic modules in a domestic environment. *Energy & Environmental Science* **2011**, *4* (10), 3741-3753.
33. Musazade, E.; Voloshin, R.; Brady, N.; Mondal, J.; Atashova, S.; Zharmukhamedov, S. K.; Huseynova, I.; Ramakrishna, S.; Najafpour, M. M.; Shen, J.-R.; Bruce, B. D.; Allakhverdiev, S. I., Biohybrid solar cells: Fundamentals, progress, and challenges. *J. Photochem. Photobiol., C* **2018**, *35*, 134-156.
34. Kim, Y.; Shin, S. A.; Lee, J.; Yang, K. D.; Nam, K. T., Hybrid system of semiconductor and photosynthetic protein. *Nanotechnology* **2014**, *25* (34).

35. Wolfe, K. D.; Dervishogullari, D.; Passantino, J. M.; Stachurski, C. D.; Jennings, G. K.; Clifffel, D. E., Improving the stability of photosystem I-based bioelectrodes for solar energy conversion. *Current Opinion in Electrochemistry* **2020**, *19*, 27-34.
36. Nguyen, K.; Bruce, B. D., Growing green electricity: Progress and strategies for use of Photosystem I for sustainable photovoltaic energy conversion. *Biochim. Biophys. Acta, Bioenerg.* **2014**, *1837* (9), 1553-1566.
37. Calogero, G.; Yum, J.-H.; Sinopoli, A.; Di Marco, G.; Graetzel, M.; Nazeeruddin, M. K., Anthocyanins and betalains as light-harvesting pigments for dye-sensitized solar cells. *Sol. Energy* **2012**, *86* (5), 1563-1575.
38. Sun, T.; Feng, L.; Gao, X.; Jiang, L., Bioinspired Surfaces with Special Wettability. *Acc. Chem. Res.* **2005**, *38* (8), 644-652.
39. Bonderer, L. J.; Studart, A. R.; Gauckler, L. J., Bioinspired Design and Assembly of Platelet Reinforced Polymer Films. *Science (Washington, DC, U. S.)* **2008**, *319* (5866), 1069-1073.
40. Ye, Q.; Zhou, F.; Liu, W., Bioinspired catecholic chemistry for surface modification. *Chem. Soc. Rev.* **2011**, *40* (7), 4244-4258.
41. *U.S. energy facts explained*; U.S. Energy Information Administration: May 7, 2020, 2020.
42. Lee, J. W.; Lee, I.; Laible, P. D.; Owens, T. G.; Greenbaum, E., Chemical platinization and its effect on excitation transfer dynamics and P700 photooxidation kinetics in isolated photosystem I. *Biophys J* **1995**, *69* (2), 652-659.
43. Greenbaum, E., Platinized Chloroplasts: A Novel Photocatalytic Material. *Science* **1985**, *230* (4732), 1373.

44. Teodor, A. H.; Bruce, B. D., Putting Photosystem I to Work: Truly Green Energy. *Trends Biotechnol.* **2020**, *38* (12), 1329-1342.
45. Lubner, C. E.; Grimme, R.; Bryant, D. A.; Golbeck, J. H., Wiring Photosystem I for Direct Solar Hydrogen Production. *Biochemistry* **2010**, *49* (3), 404-414.
46. Wolfe, K. D.; Dervishogullari, D.; Stachurski, C. D.; Passantino, J. M.; Jennings, G. K.; Cliffel, D. E., Photosystem I Multilayers within Porous Indium Tin Oxide Cathodes Enhance Mediated Electron Transfer. *Chemelectrochem* **2020**, *7* (3).
47. Robinson, M. T.; Armbruster, M. E.; Gargye, A.; Cliffel, D. E.; Jennings, G. K., Photosystem I Multilayer Films for Photovoltage Enhancement in Natural Dye-Sensitized Solar Cells. *Acs Appl Energ Mater* **2018**, *1* (2), 301-305.
48. Dervishogullari, D.; Gizzie, E. A.; Jennings, G. K.; Cliffel, D. E., Polyviologen as Electron Transport Material in Photosystem I-Based Biophotovoltaic Cells. *Langmuir* **2018**, *34* (51), 15658-15664.
49. Barhom, H.; Carmeli, C.; Carmeli, I., Fabrication of Electronic Junctions between Oriented Multilayers of Photosystem I and the Electrodes of Optoelectronic Solid-State Devices. *J. Phys. Chem. B* **2021**, *125* (3), 722-728.
50. Ciornii, D.; Koelsch, A.; Zouni, A.; Lisdat, F., A precursor-approach in constructing 3D ITO electrodes for the improved performance of photosystem I-cyt c photobioelectrodes. *Nanoscale* **2019**, *11* (34), 15862-15870.
51. Tapia, C.; Milton, R. D.; Pankratova, G.; Minter, S. D.; Aakerlund, H.-E.; Leech, D.; De Lacey, A. L.; Pita, M.; Gorton, L., Wiring of Photosystem I and Hydrogenase on an Electrode for Photoelectrochemical H₂ Production by using Redox Polymers for Relatively Positive Onset Potential. *Chemelectrochem* **2017**, *4* (1), 90-95.

52. Rasmussen, M.; Wingersky, A.; Minter, S. D., Improved performance of a thylakoid bio-solar cell by incorporation of carbon quantum dots. *ECS Electrochem. Lett.* **2014**, *3* (2), H1-H3.
53. Golbeck, J. H.; Bryant, D. A., Photosystem I. *Curr. Top. Bioenerg.* **1991**, *16*, 83-177.
54. Höhner, R.; Pribil, M.; Herbstová, M.; Lopez, L. S.; Kunz, H.-H.; Li, M.; Wood, M.; Svoboda, V.; Puthiyaveetil, S.; Leister, D.; Kirchhoff, H., Plastocyanin is the long-range electron carrier between photosystem II and photosystem I in plants. *Proceedings of the National Academy of Sciences* **2020**, *117* (26), 15354-15362.
55. Gao, J.; Wang, H.; Yuan, Q.; Feng, Y., Structure and Function of the Photosystem Supercomplexes. *Front Plant Sci* **2018**, *9* (357).
56. Brady, N. G.; Li, M.; Ma, Y.; Gumbart, J. C.; Bruce, B. D., Non-detergent isolation of a cyanobacterial photosystem I using styrene maleic acid alternating copolymers. *Rsc Adv* **2019**, *9* (54), 31781-31796.
57. Agostiano, A.; Ceglie, A.; Monica, M. D., Current-potential curves of photosystems adsorbed on platinized platinum electrodes. *Bioelectrochemistry and Bioenergetics* **1983**, *10* (4), 377-384.
58. Gunther, D.; LeBlanc, G.; Prasai, D.; Zhang, J. R.; Cliffel, D. E.; Bolotin, K. I.; Jennings, G. K., Photosystem I on Graphene as a Highly Transparent, Photoactive Electrode. *Langmuir* **2013**, *29* (13), 4177-4180.
59. LeBlanc, G.; Winter, K. M.; Crosby, W. B.; Jennings, G. K.; Cliffel, D. E., Integration of Photosystem I with Graphene Oxide for Photocurrent Enhancement. *Advanced Energy Materials* **2014**, *4* (9).

60. Gizzie, E. A.; Scott Niezgod, J.; Robinson, M. T.; Harris, A. G.; Kane Jennings, G.; Rosenthal, S. J.; Cliffel, D. E., Photosystem I-polyaniline/TiO₂ solid-state solar cells: simple devices for biohybrid solar energy conversion. *Energy & Environmental Science* **2015**, *8* (12), 3572-3576.
61. Robinson, M. T.; Simons, C. E.; Cliffel, D. E.; Jennings, G. K., Photocatalytic photosystem I/PEDOT composite films prepared by vapor-phase polymerization. *Nanoscale* **2017**, *9* (18), 6158-6166.
62. Bennett, T. H.; Vaughn, M. D.; Davari, S. A.; Park, K.; Mukherjee, D.; Khomami, B., Jolly green MOF: confinement and photoactivation of photosystem I in a metal-organic framework. *Nanoscale Adv.* **2019**, *1* (1), 94-104.
63. Ciornii, D.; Kolsch, A.; Zouni, A.; Lisdat, F., A precursor-approach in constructing 3D ITO electrodes for the improved performance of photosystem I-cyt c photobioelectrodes. *Nanoscale* **2019**, *11* (34), 15862-15870.
64. Wolfe, K. D.; Dervishogullari, D.; Stachurski, C. D.; Passantino, J. M.; Kane Jennings, G.; Cliffel, D. E., Photosystem I Multilayers within Porous Indium Tin Oxide Cathodes Enhance Mediated Electron Transfer. *Chemelectrochem* **2020**, *7* (3), 585-585.
65. Teodor, A. H.; Ooi, E.-J.; Medina, J.; Alarcon, M.; Vaughn, M. D.; Bruce, B. D.; Bergkamp, J. J., Aqueous-soluble bipyridine cobalt(ii/iii) complexes act as direct redox mediators in photosystem I-based biophotovoltaic devices. *Rsc Adv* **2021**, *11* (18), 10434-10450.
66. McCreery, R. L., Advanced Carbon Electrode Materials for Molecular Electrochemistry. *Chem. Rev. (Washington, DC, U. S.)* **2008**, *108* (7), 2646-2687.
67. Wang, G.; Zhang, L.; Zhang, J., A review of electrode materials for electrochemical supercapacitors. *Chem. Soc. Rev.* **2012**, *41* (2), 797-828.

68. Ciornii, D.; Feifel, S. C.; Hejazi, M.; Koelsch, A.; Lokstein, H.; Zouni, A.; Lisdar, F., Construction of photobiocathodes using multi-walled carbon nanotubes and photosystem I. *Phys. Status Solidi A* **2017**, *214* (9), n/a.
69. Nii, D.; Miyachi, M.; Shimada, Y.; Nozawa, Y.; Ito, M.; Homma, Y.; Ikehira, S.; Yamanoi, Y.; Nishihara, H.; Tomo, T., Conjugates between photosystem I and a carbon nanotube for a photoresponse device. *Photosynth. Res.* **2017**, *133* (1-3), 155-162.
70. Darby, E.; LeBlanc, G.; Gizzie, E. A.; Winter, K. M.; Jennings, G. K.; Cliffel, D. E., Photoactive Films of Photosystem I on Transparent Reduced Graphene Oxide Electrodes. *Langmuir* **2014**, *30* (29), 8990-8994.
71. Morlock, S.; Subramanian, S. K.; Zouni, A.; Lisdar, F., Scalable Three-Dimensional Photobioelectrodes Made of Reduced Graphene Oxide Combined with Photosystem I. *Acs Appl Mater Inter* **2021**, *13* (9), 11237-11246.
72. Feifel, S. C.; Lokstein, H.; Hejazi, M.; Zouni, A.; Lisdar, F., Unidirectional Photocurrent of Photosystem I on π -System-Modified Graphene Electrodes: Nanobionic Approaches for the Construction of Photobiohybrid Systems. *Langmuir* **2015**, *31* (38), 10590-10598.
73. Kiliszek, M.; Harputlu, E.; Szalkowski, M.; Kowalska, D.; Unlu, C. G.; Haniewicz, P.; Abram, M.; Wiwatowski, K.; Niedziolka-Jonsson, J.; Mackowski, S.; Ocakoglu, K.; Kargul, J., Orientation of photosystem I on graphene through cytochrome c553 leads to improvement in photocurrent generation. *J. Mater. Chem. A* **2018**, *6* (38), 18615-18626.
74. Vermass, W. F. J.; Rutherford, A. W.; Hansson, Ö., Site-directed mutagenesis in photosystem II of the cyanobacterium Synechocystis sp. PCC 6803:

Donor D is a tyrosine residue in the D2 protein. *Proceedings of the National Academy of Sciences* **1988**, *85* (22), 8477.

75. Rasmussen, M.; Shrier, A.; Minter, S. D., High performance thylakoid bio-solar cell using laccase enzymatic biocathodes. *Phys. Chem. Chem. Phys.* **2013**, *15* (23), 9062-9065.

76. Rasmussen, M.; Wingersky, A.; Minter, S. D., Comparative study of thylakoids from higher plants for solar energy conversion and herbicide detection. *Electrochim. Acta* **2014**, *140*, 304-308.

77. Reeves, S. G.; Hall, D. O., [8] Higher plant chloroplasts and grana: General preparative procedures (excluding high carbon dioxide fixation ability chloroplasts). In *Methods in Enzymology*, San Pietro, A., Ed. Academic Press: 1980; Vol. 69, pp 85-94.

78. Musazade, E.; Voloshin, R.; Brady, N.; Mondal, J.; Atashova, S.; Zharmukhamedov, S. K.; Huseynova, I.; Ramakrishna, S.; Najafpour, M. M.; Shen, J.-R.; Bruce, B. D.; Allakhverdiev, S. I., Biohybrid solar cells: Fundamentals, progress, and challenges. *Journal of Photochemistry and Photobiology C: Photochemistry Reviews* **2018**, *35*, 134-156.

79. Korotych, O.; Mondal, J.; Gattás-Asfura, K. M.; Hendricks, J.; Bruce, B. D., Evaluation of commercially available styrene-co-maleic acid polymers for the extraction of membrane proteins from spinach chloroplast thylakoids. *European Polymer Journal* **2019**, *114*, 485-500.

80. Baba, K.; Itoh, S.; Hastings, G.; Hoshina, S., Photoinhibition of Photosystem I electron transfer activity in isolated Photosystem I preparations with different chlorophyll contents. *Photosynth Res* **1996**, *47* (2), 121-130.

81. Ciesielski, P. N.; Hijazi, F. M.; Scott, A. M.; Faulkner, C. J.; Beard, L.; Emmett, K.; Rosenthal, S. J.; Cliffel, D.; Kane Jennings, G., Photosystem I – Based biohybrid photoelectrochemical cells. *Bioresource Technology* **2010**, *101* (9), 3047-3053.

82. Ciesielski, P. N.; Faulkner, C. J.; Irwin, M. T.; Gregory, J. M.; Tolk, N. H.; Cliffel, D. E.; Jennings, G. K., Enhanced Photocurrent Production by Photosystem I Multilayer Assemblies. *Adv Funct Mater* **2010**, *20* (23), 4048-4054.
83. Stieger, K. R.; Feifel, S. C.; Lokstein, H.; Hejazi, M.; Zouni, A.; Lisdat, F., Biohybrid architectures for efficient light-to-current conversion based on photosystem I within scalable 3D mesoporous electrodes. *J. Mater. Chem. A* **2016**, *4* (43), 17009-17017.
84. Ciesielski, P. N.; Hijazi, F. M.; Scott, A. M.; Faulkner, C. J.; Beard, L.; Emmett, K.; Rosenthal, S. J.; Cliffel, D.; Jennings, G. K., Photosystem I - Based biohybrid photoelectrochemical cells. *Bioresource Technology* **2010**, *101* (9), 3047-3053.
85. Robinson, M. T.; Cliffel, D. E.; Jennings, G. K., An Electrochemical Reaction-Diffusion Model of the Photocatalytic Effect of Photosystem I Multilayer Films. *J Phys Chem B* **2018**, *122* (1), 117-125.
86. Bard, A. J., *Electrochemical methods : fundamentals and applications / Allen J. Bard, Larry R. Faulkner*. Wiley: New York, 1980.
87. Bard, A. J.; Faulkner, L. R., *Electrochemical Methods - Fundamentals and Applications*. 2 ed.; John Wiley & Sons, Inc.: 2001; p 833.
88. Elgrishi, N.; Rountree, K. J.; McCarthy, B. D.; Rountree, E. S.; Eisenhart, T. T.; Dempsey, J. L., A Practical Beginner's Guide to Cyclic Voltammetry. *Journal of Chemical Education* **2018**, *95* (2), 197-206.
89. Wang, J., *Analytical Electrochemistry, Third Edition*. John Wiley & Sons, Inc.: 2006.
90. Gizzie, E. A.; Niezgoda, J. S.; Robinson, M. T.; Harris, A. G.; Jennings, G. K.; Rosenthal, S. J.; Cliffel, D. E., Photosystem I-polyaniline/TiO₂ solid-state solar cells: simple

devices for biohybrid solar energy conversion. *Energy & Environmental Science* **2015**, 8 (12), 3572-3576.

91. Wang, R.; Lu, K.-Q.; Tang, Z.-R.; Xu, Y.-J., Recent progress in carbon quantum dots: synthesis, properties and applications in photocatalysis. *J Mater Chem A* **2017**, 5 (8), 3717-3734.

92. Wang, Q.; Huang, X.; Long, Y.; Wang, X.; Zhang, H.; Zhu, R.; Liang, L.; Teng, P.; Zheng, H., Hollow luminescent carbon dots for drug delivery. *Carbon* **2013**, 59, 192-199.

93. Xu, X.; Ray, R.; Gu, Y.; Ploehn, H. J.; Gearheart, L.; Raker, K.; Scrivens, W. A., Electrophoretic Analysis and Purification of Fluorescent Single-Walled Carbon Nanotube Fragments. *Journal of the American Chemical Society* **2004**, 126 (40), 12736-12737.

94. Rasmussen, M.; Wingersky, A.; Minter, S. D., Improved Performance of a Thylakoid Bio-Solar Cell by Incorporation of Carbon Quantum Dots. *Ecs Electrochem Lett* **2013**, 3 (2), H1-H3.

95. Zhang, X.; Wang, F.; Huang, H.; Li, H.; Han, X.; Liu, Y.; Kang, Z., Carbon quantum dot sensitized TiO₂ nanotube arrays for photoelectrochemical hydrogen generation under visible light. *Nanoscale* **2013**, 5 (6), 2274-2278.

96. Meng, Y.; Zhang, Y.; Sun, W.; Wang, M.; He, B.; Chen, H.; Tang, Q., Biomass converted carbon quantum dots for all-weather solar cells. *Electrochim Acta* **2017**, 257, 259-266.

97. Kong, T.; Hao, L.; Wei, Y.; Cai, X.; Zhu, B., Doxorubicin conjugated carbon dots as a drug delivery system for human breast cancer therapy. *Cell Proliferation* **2018**, 51 (5), e12488.

98. Esteves da Silva, J. C. G.; Gonçalves, H. M. R., Analytical and bioanalytical applications of carbon dots. *TrAC Trends in Analytical Chemistry* **2011**, 30 (8), 1327-1336.

99. Paulo, S.; Palomares, E.; Martinez-Ferrero, E., Graphene and Carbon Quantum Dot-Based Materials in Photovoltaic Devices: From Synthesis to Applications. *Nanomaterials* **2016**, *6* (9).
100. Paulo, S.; Stoica, G.; Cambarau, W.; Martinez-Ferrero, E.; Palomares, E., Carbon quantum dots as new hole transport material for perovskite solar cells. *Synthetic Metals* **2016**, *222*, 17-22.
101. Sun, D.; Ban, R.; Zhang, P.-H.; Wu, G.-H.; Zhang, J.-R.; Zhu, J.-J., Hair fiber as a precursor for synthesizing of sulfur- and nitrogen-co-doped carbon dots with tunable luminescence properties. *Carbon* **2013**, *64*, 424-434.
102. Calabro, R. L.; Yang, D.-S.; Kim, D. Y., Liquid-phase laser ablation synthesis of graphene quantum dots from carbon nano-onions: Comparison with chemical oxidation. *Journal of Colloid and Interface Science* **2018**, *527*, 132-140.
103. Du, F.; Yuan, J.; Zhang, M.; Li, J.; Zhou, Z.; Li, Z.; Cao, M.; Chen, J.; Zhang, L.; Liu, X.; Gong, A.; Xu, W.; Shao, Q., Nitrogen-doped carbon dots with heterogeneous multi-layered structures. *Rsc Adv* **2014**, *4* (71), 37536-37541.
104. Yan, L.; Yang, Y.; Ma, C.-Q.; Liu, X.; Wang, H.; Xu, B., Synthesis of carbon quantum dots by chemical vapor deposition approach for use in polymer solar cell as the electrode buffer layer. *Carbon* **2016**, *109*, 598-607.
105. Rigodanza, F.; Đorđević, L.; Arcudi, F.; Prato, M., Customizing the Electrochemical Properties of Carbon Nanodots by Using Quinones in Bottom-Up Synthesis. *Angewandte Chemie International Edition* **2018**, *57* (18), 5062-5067.
106. De, B.; Karak, N., A green and facile approach for the synthesis of water soluble fluorescent carbon dots from banana juice. *Rsc Adv* **2013**, *3* (22), 8286-8290.

107. Dong, Y.; Pang, H.; Yang, H. B.; Guo, C.; Shao, J.; Chi, Y.; Li, C. M.; Yu, T., Carbon-Based Dots Co-doped with Nitrogen and Sulfur for High Quantum Yield and Excitation-Independent Emission. *Angewandte Chemie International Edition* **2013**, *52* (30), 7800-7804.
108. Zhang, H.; Chen, Y.; Liang, M.; Xu, L.; Qi, S.; Chen, H.; Chen, X., Solid-Phase Synthesis of Highly Fluorescent Nitrogen-Doped Carbon Dots for Sensitive and Selective Probing Ferric Ions in Living Cells. *Analytical Chemistry* **2014**, *86* (19), 9846-9852.
109. Peng, H.; Travas-Sejdic, J., Simple Aqueous Solution Route to Luminescent Carbogenic Dots from Carbohydrates. *Chemistry of Materials* **2009**, *21* (23), 5563-5565.
110. Qu, D.; Zheng, M.; Du, P.; Zhou, Y.; Zhang, L.; Li, D.; Tan, H.; Zhao, Z.; Xie, Z.; Sun, Z., Highly luminescent S, N co-doped graphene quantum dots with broad visible absorption bands for visible light photocatalysts. *Nanoscale* **2013**, *5* (24), 12272-12277.
111. Qu, D.; Zheng, M.; Zhang, L.; Zhao, H.; Xie, Z.; Jing, X.; Haddad, R. E.; Fan, H.; Sun, Z., Formation mechanism and optimization of highly luminescent N-doped graphene quantum dots. *Scientific reports* **2014**, *4*, 5294-5294.
112. Fernando, K. A. S.; Sahu, S.; Liu, Y.; Lewis, W. K.; Gulians, E. A.; Jafariyan, A.; Wang, P.; Bunker, C. E.; Sun, Y.-P., Carbon Quantum Dots and Applications in Photocatalytic Energy Conversion. *Acs Appl Mater Inter* **2015**, *7* (16), 8363-8376.
113. Jiang, K.; Sun, S.; Zhang, L.; Lu, Y.; Wu, A.; Cai, C.; Lin, H., Red, Green, and Blue Luminescence by Carbon Dots: Full-Color Emission Tuning and Multicolor Cellular Imaging. *Angewandte Chemie International Edition* **2015**, *54* (18), 5360-5363.
114. Lim, C. S.; Hola, K.; Ambrosi, A.; Zboril, R.; Pumera, M., Graphene and carbon quantum dots electrochemistry. *Electrochem Commun* **2015**, *52*, 75-79.

115. Ding, H.; Yu, S.-B.; Wei, J.-S.; Xiong, H.-M., Full-Color Light-Emitting Carbon Dots with a Surface-State-Controlled Luminescence Mechanism. *ACS Nano* **2016**, *10* (1), 484-491.
116. Wang, H.; Sun, P.; Cong, S.; Wu, J.; Gao, L.; Wang, Y.; Dai, X.; Yi, Q.; Zou, G., Nitrogen-Doped Carbon Dots for “green” Quantum Dot Solar Cells. *Nanoscale Research Letters* **2016**, *11* (1), 27.
117. Shen, Z.; Guo, X.; Liu, L.; Sunarso, J.; Wang, G.; Wang, S.; Liu, S., Carbon-Dot/Natural-Dye Sensitizer for TiO₂ Solar Cells Prepared by a One-Step Treatment of Celery Leaf Extract. *ChemPhotoChem* **2017**, *1* (10), 470-478.
118. Liao, S.; Zhu, F.; Zhao, X.; Yang, H.; Chen, X., A reusable P, N-doped carbon quantum dot fluorescent sensor for cobalt ion. *Sensors and Actuators B: Chemical* **2018**, *260*, 156-164.
119. Wu, X.; Wu, L.; Cao, X.; Li, Y.; Liu, A.; Liu, S., Nitrogen-doped carbon quantum dots for fluorescence detection of Cu²⁺ and electrochemical monitoring of bisphenol A. *Rsc Adv* **2018**, *8* (36), 20000-20006.
120. Zhang, Y.; He, Y. H.; Cui, P. P.; Feng, X. T.; Chen, L.; Yang, Y. Z.; Liu, X. G., Water-soluble, nitrogen-doped fluorescent carbon dots for highly sensitive and selective detection of Hg²⁺ in aqueous solution. *Rsc Adv* **2015**, *5* (50), 40393-40401.
121. Jiang, K.; Sun, S.; Zhang, L.; Wang, Y.; Cai, C.; Lin, H., Bright-Yellow-Emissive N-Doped Carbon Dots: Preparation, Cellular Imaging, and Bifunctional Sensing. *Acs Appl Mater Inter* **2015**, *7* (41), 23231-23238.
122. Li, Y.; Hu, Y.; Zhao, Y.; Shi, G.; Deng, L.; Hou, Y.; Qu, L., An Electrochemical Avenue to Green-Luminescent Graphene Quantum Dots as Potential Electron-Acceptors for Photovoltaics. *Adv Mater* **2011**, *23* (6), 776-780.

123. Sun, M.; Ma, X.; Chen, X.; Sun, Y.; Cui, X.; Lin, Y., A nanocomposite of carbon quantum dots and TiO₂ nanotube arrays: enhancing photoelectrochemical and photocatalytic properties. *Rsc Adv* **2014**, *4* (3), 1120-1127.
124. Wang, X.; Zhang, M.; Huo, X.; Zhao, W.; Kang, B.; Xu, J.-J.; Chen, H., Modulating the electronic structure of a semiconductor to optimize its electrochemiluminescence performance. *Nanoscale Adv* **2019**, *1* (5), 1965-1969.
125. Peng, H.; Li, Y.; Jiang, C.; Luo, C.; Qi, R.; Huang, R.; Duan, C.-G.; Trivas-Sejdic, J., Tuning the properties of luminescent nitrogen-doped carbon dots by reaction precursors. *Carbon* **2016**, *100*, 386-394.
126. Privitera, A.; Righetto, M.; Mosconi, D.; Lorandi, F.; Isse, A. A.; Moretto, A.; Bozio, R.; Ferrante, C.; Franco, L., Boosting carbon quantum dots/fullerene electron transfer via surface group engineering. *Phys Chem Chem Phys* **2016**, *18* (45), 31286-31295.
127. Chen, Y.; Zheng, M.; Xiao, Y.; Dong, H.; Zhang, H.; Zhuang, J.; Hu, H.; Lei, B.; Liu, Y., A Self-Quenching-Resistant Carbon-Dot Powder with Tunable Solid-State Fluorescence and Construction of Dual-Fluorescence Morphologies for White Light-Emission. *Adv Mater* **2016**, *28* (2), 312-318.
128. Liu, Y.; Gong, X.; Dong, W.; Zhou, R.; Shuang, S.; Dong, C., Nitrogen and phosphorus dual-doped carbon dots as a label-free sensor for Curcumin determination in real sample and cellular imaging. *Talanta* **2018**, *183*, 61-69.
129. Fan, Y. Z.; Zhang, Y.; Li, N.; Liu, S. G.; Liu, T.; Li, N. B.; Luo, H. Q., A facile synthesis of water-soluble carbon dots as a label-free fluorescent probe for rapid, selective and sensitive detection of picric acid. *Sensors and Actuators B: Chemical* **2017**, *240*, 949-955.

130. Das, P.; Ganguly, S.; Mondal, S.; Bose, M.; Das, A. K.; Banerjee, S.; Das, N. C., Heteroatom doped photoluminescent carbon dots for sensitive detection of acetone in human fluids. *Sensors and Actuators B: Chemical* **2018**, *266*, 583-593.
131. Jiang, H.; Liu, L.; Zhao, K.; Liu, Z.; Zhang, X.; Hu, S., Effect of pyridinic- and pyrrolic-nitrogen on electrochemical performance of Pd for formic acid electrooxidation. *Electrochim Acta* **2020**, *337*, 135758.
132. Dukes, A. D.; Samson, P. C.; Keene, J. D.; Davis, L. M.; Wikswo, J. P.; Rosenthal, S. J., Single-Nanocrystal Spectroscopy of White-Light-Emitting CdSe Nanocrystals. *The Journal of Physical Chemistry A* **2011**, *115* (16), 4076-4081.
133. Orfield, N. J.; McBride, J. R.; Wang, F.; Buck, M. R.; Keene, J. D.; Reid, K. R.; Htoon, H.; Hollingsworth, J. A.; Rosenthal, S. J., Quantum Yield Heterogeneity among Single Nonblinking Quantum Dots Revealed by Atomic Structure-Quantum Optics Correlation. *ACS Nano* **2016**, *10* (2), 1960-1968.
134. Chung, D. D. L., Review Graphite. *Journal of Materials Science* **2002**, *37* (8), 1475-1489.
135. Gao, F.; Ma, S.; Li, J.; Dai, K.; Xiao, X.; Zhao, D.; Gong, W., Rational design of high quality citric acid-derived carbon dots by selecting efficient chemical structure motifs. *Carbon* **2017**, *112*, 131-141.
136. Amjadi, M.; Hallaj, T.; Asadollahi, H.; Song, Z.; de Frutos, M.; Hildebrandt, N., Facile synthesis of carbon quantum dot/silver nanocomposite and its application for colorimetric detection of methimazole. *Sensors and Actuators B: Chemical* **2017**, *244*, 425-432.

137. LeCroy, G. E.; Messina, F.; Sciortino, A.; Bunker, C. E.; Wang, P.; Fernando, K. A. S.; Sun, Y.-P., Characteristic Excitation Wavelength Dependence of Fluorescence Emissions in Carbon “Quantum” Dots. *The Journal of Physical Chemistry C* **2017**, *121* (50), 28180-28186.
138. Wu, Z. L.; Gao, M. X.; Wang, T. T.; Wan, X. Y.; Zheng, L. L.; Huang, C. Z., A general quantitative pH sensor developed with dicyandiamide N-doped high quantum yield graphene quantum dots. *Nanoscale* **2014**, *6* (7), 3868-3874.
139. Yang, Z.; Xu, M.; Liu, Y.; He, F.; Gao, F.; Su, Y.; Wei, H.; Zhang, Y., Nitrogen-doped, carbon-rich, highly photoluminescent carbon dots from ammonium citrate. *Nanoscale* **2014**, *6* (3), 1890-1895.
140. Yuan, Y. H.; Liu, Z. X.; Li, R. S.; Zou, H. Y.; Lin, M.; Liu, H.; Huang, C. Z., Synthesis of nitrogen-doping carbon dots with different photoluminescence properties by controlling the surface states. *Nanoscale* **2016**, *8* (12), 6770-6776.
141. Hu, C.; Li, M.; Qiu, J.; Sun, Y.-P., Design and fabrication of carbon dots for energy conversion and storage. *Chemical Society Reviews* **2019**, *48* (8), 2315-2337.
142. Sun, Y.-P.; Zhou, B.; Lin, Y.; Wang, W.; Fernando, K. A. S.; Pathak, P.; Meziani, M. J.; Harruff, B. A.; Wang, X.; Wang, H.; Luo, P. G.; Yang, H.; Kose, M. E.; Chen, B.; Veca, L. M.; Xie, S.-Y., Quantum-Sized Carbon Dots for Bright and Colorful Photoluminescence. *Journal of the American Chemical Society* **2006**, *128* (24), 7756-7757.
143. Zhang, Q.; Zhang, C.; Li, Z.; Ge, J.; Li, C.; Dong, C.; Shuang, S., Nitrogen-doped carbon dots as fluorescent probe for detection of curcumin based on the inner filter effect. *Rsc Adv* **2015**, *5* (115), 95054-95060.

144. Gong, X.; Lu, W.; Paau, M. C.; Hu, Q.; Wu, X.; Shuang, S.; Dong, C.; Choi, M. M. F., Facile synthesis of nitrogen-doped carbon dots for Fe³⁺ sensing and cellular imaging. *Analytica Chimica Acta* **2015**, *861*, 74-84.
145. Yang, Y.; Lin, X.; Li, W.; Ou, J.; Yuan, Z.; Xie, F.; Hong, W.; Yu, D.; Ma, Y.; Chi, Z.; Chen, X., One-Pot Large-Scale Synthesis of Carbon Quantum Dots: Efficient Cathode Interlayers for Polymer Solar Cells. *Acs Appl Mater Inter* **2017**, *9* (17), 14953-14959.
146. Zhang, D.-W.; Papaioannou, N.; David, N. M.; Luo, H.; Gao, H.; Tanase, L. C.; Degousée, T.; Samorì, P.; Sapelkin, A.; Fenwick, O.; Titirici, M.-M.; Krause, S., Photoelectrochemical response of carbon dots (CDs) derived from chitosan and their use in electrochemical imaging. *Materials Horizons* **2018**, *5* (3), 423-428.
147. Cong, K.; Radtke, M.; Stumpf, S.; Schröter, B.; McMillan, D. G. G.; Rettenmayr, M.; Ignaszak, A., Electrochemical stability of the polymer-derived nitrogen-doped carbon: an elusive goal? *Materials for Renewable and Sustainable Energy* **2015**, *4* (2), 5.
148. Lou, F.; Buan, M. E. M.; Muthuswamy, N.; Walmsley, J. C.; Rønning, M.; Chen, D., One-step electrochemical synthesis of tunable nitrogen-doped graphene. *J Mater Chem A* **2016**, *4* (4), 1233-1243.
149. Pelzer, K. M.; Cheng, L.; Curtiss, L. A., Effects of Functional Groups in Redox-Active Organic Molecules: A High-Throughput Screening Approach. *The Journal of Physical Chemistry C* **2017**, *121* (1), 237-245.
150. Inamdar, S. N.; Ingole, P. P.; Haram, S. K., Determination of Band Structure Parameters and the Quasi-Particle Gap of CdSe Quantum Dots by Cyclic Voltammetry. *ChemPhysChem* **2008**, *9* (17), 2574-2579.

151. Ciesielski, P. N.; Hijazi, F. M.; Scott, A. M.; Faulkner, C. J.; Beard, L.; Emmett, K.; Rosenthal, S. J.; Cliffel, D.; Kane Jennings, G., Photosystem I- based biohybrid photoelectrochemical cells. *Bioresour. Technol.* **2010**, *101* (9), 3047-3053.
152. Rincón, R. A.; Lau, C.; Luckarift, H. R.; Garcia, K. E.; Adkins, E.; Johnson, G. R.; Atanassov, P., Enzymatic fuel cells: Integrating flow-through anode and air-breathing cathode into a membrane-less biofuel cell design. *Biosensors and Bioelectronics* **2011**, *27* (1), 132-136.
153. Higgins, S. R.; Lau, C.; Atanassov, P.; Minter, S. D.; Cooney, M. J., Hybrid Biofuel Cell: Microbial Fuel Cell with an Enzymatic Air-Breathing Cathode. *ACS Catalysis* **2011**, *1* (9), 994-997.
154. Shinkarev, V. P.; Vassiliev, I. R.; Golbeck, J. H., A Kinetic Assessment of the Sequence of Electron Transfer from FX to FA and Further to FB in Photosystem I: The Value of the Equilibrium Constant between FX and FA. *Biophysical Journal* **2000**, *78* (1), 363-372.
155. Ocakoglu, K.; Krupnik, T.; van den Bosch, B.; Harputlu, E.; Gullo, M. P.; Olmos, J. D. J.; Yildirimcan, S.; Gupta, R. K.; Yakuphanoglu, F.; Barbieri, A.; Reek, J. N. H.; Kargul, J., Photosystem I-based Biophotovoltaics on Nanostructured Hematite. *Advanced Functional Materials* **2014**, *24* (47), 7467-7477.
156. Ciesielski, P. N.; Scott, A. M.; Faulkner, C. J.; Berron, B. J.; Cliffel, D. E.; Jennings, G. K., Functionalized nanoporous gold leaf electrode films for the immobilization of photosystem I. *ACS Nano* **2008**, *2* (12), 2465-72.
157. Wolfe, K. D.; Dervishogullari, D.; Stachurski, C. D.; Passantino, J. M.; Kane Jennings, G.; Cliffel, D. E., Photosystem I Multilayers within Porous Indium Tin Oxide Cathodes Enhance Mediated Electron Transfer. *ChemElectroChem* **2019**, *7* (3), 596-603.

158. Darby, E.; LeBlanc, G.; Gizzie, E. A.; Winter, K. M.; Jennings, G. K.; Cliffel, D. E., Photoactive films of photosystem I on transparent reduced graphene oxide electrodes. *Langmuir* **2014**, *30* (29), 8990-4.
159. Gunther, D.; LeBlanc, G.; Prasai, D.; Zhang, J. R.; Cliffel, D. E.; Bolotin, K. I.; Jennings, G. K., Photosystem I on graphene as a highly transparent, photoactive electrode. *Langmuir* **2013**, *29* (13), 4177-80.
160. Wang, J., Carbon-Nanotube Based Electrochemical Biosensors: A Review. *Electroanalysis* **2005**, *17* (1), 7-14.
161. Nii, D.; Miyachi, M.; Shimada, Y.; Nozawa, Y.; Ito, M.; Homma, Y.; Ikehira, S.; Yamanoi, Y.; Nishihara, H.; Tomo, T., Conjugates between photosystem I and a carbon nanotube for a photoresponse device. *Photosynth Res* **2017**, *133* (1-3), 155-162.
162. Ciornii, D.; Feifel, S. C.; Hejazi, M.; Kölsch, A.; Lokstein, H.; Zouni, A.; Lisdat, F., Construction of photobiocathodes using multi-walled carbon nanotubes and photosystem I. *physica status solidi (a)* **2017**, *214* (9).
163. Kaniber, S. M.; Brandstetter, M.; Simmel, F. C.; Carmeli, I.; Holleitner, A. W., On-chip functionalization of carbon nanotubes with photosystem I. *J Am Chem Soc* **2010**, *132* (9), 2872-3.
164. Carmeli, I.; Mangold, M.; Frolov, L.; Zebli, B.; Carmeli, C.; Richter, S.; Holleitner, A. W., A Photosynthetic Reaction Center Covalently Bound to Carbon Nanotubes. *Adv Mater* **2007**, *19* (22), 3901-3905.
165. Calkins, J. O.; Umasankar, Y.; O'Neill, H.; Ramasamy, R. P., High photo-electrochemical activity of thylakoid-carbon nanotube composites for photosynthetic energy conversion. *Energ Environ Sci* **2013**, *6* (6).

166. Cai, C.; Chen, J., Direct electron transfer of glucose oxidase promoted by carbon nanotubes. *Analytical Biochemistry* **2004**, *332* (1), 75-83.
167. Zhang, M.; Smith, A.; Gorski, W., Carbon Nanotube–Chitosan System for Electrochemical Sensing Based on Dehydrogenase Enzymes. *Analytical Chemistry* **2004**, *76* (17), 5045-5050.
168. Reid, R. C.; Jones, S. R.; Hickey, D. P.; Minteer, S. D.; Gale, B. K., Modeling Carbon Nanotube Connectivity and Surface Activity in a Contact Lens Biofuel Cell. *Electrochimica Acta* **2016**, *203*, 30-40.
169. Kincaid, H. A.; Niedringhaus, T.; Ciobanu, M.; Cliffel, D. E.; Jennings, G. K., Entrapment of Photosystem I within Self-Assembled Films. *Langmuir* **2006**, *22* (19), 8114-8120.
170. Suslova, E.; Savilov, S.; Egorov, A.; Shumyantsev, A.; Lunin, V., Carbon nanotube frameworks by spark plasma sintering. *Microporous and Mesoporous Materials* **2019**, 109807.
171. Voiry, D.; Chhowalla, M.; Gogotsi, Y.; Kotov, N. A.; Li, Y.; Penner, R. M.; Schaak, R. E.; Weiss, P. S., Best Practices for Reporting Electrocatalytic Performance of Nanomaterials. *ACS Nano* **2018**, *12* (10), 9635-9638.
172. Yang, Q.; Ma, L.; Xiao, S.; Zhang, D.; Djoulde, A.; Ye, M.; Lin, Y.; Geng, S.; Li, X.; Chen, T.; Sun, L., Electrical Conductivity of Multiwall Carbon Nanotube Bundles Contacting with Metal Electrodes by Nano Manipulators inside SEM. *Nanomaterials* **2021**, *11* (5).
173. Besteman, K.; Lee, J.-O.; Wiertz, F. G. M.; Heering, H. A.; Dekker, C., Enzyme-Coated Carbon Nanotubes as Single-Molecule Biosensors. *Nano Letters* **2003**, *3* (6), 727-730.

174. Robinson, M. T.; Cliffler, D. E.; Jennings, G. K., An Electrochemical Reaction-Diffusion Model of the Photocatalytic Effect of Photosystem I Multilayer Films. *The Journal of Physical Chemistry B* **2018**, *122* (1), 117-125.
175. Lee, J.; Kim, J.; Hyeon, T., Recent progress in the synthesis of porous carbon materials. *Adv. Mater. (Weinheim, Ger.)* **2006**, *18* (16), 2073-2094.
176. Singh, V.; Joung, D.; Zhai, L.; Das, S.; Khondaker, S. I.; Seal, S., Graphene based materials: Past, present and future. *Prog. Mater. Sci.* **2011**, *56* (8), 1178-1271.
177. Gross, A. J.; Holzinger, M.; Cosnier, S., Buckypaper bioelectrodes: emerging materials for implantable and wearable biofuel cells. *Energy Environ. Sci.* **2018**, *11* (7), 1670-1687.
178. Thostenson, E. T.; Ren, Z.; Chou, T. W., Advances in the science and technology of carbon nanotubes and their composites: a review. *Compos. Sci. Technol.* **2001**, *61* (13), 1899-1912.
179. Lam, C.-w.; James, J. T.; McCluskey, R.; Arepalli, S.; Hunter, R. L., A Review of Carbon Nanotube Toxicity and Assessment of Potential Occupational and Environmental Health Risks. *Crit. Rev. Toxicol.* **2006**, *36* (3), 189-217.
180. Tasis, D.; Tagmatarchis, N.; Bianco, A.; Prato, M., Chemistry of Carbon Nanotubes. *Chem. Rev. (Washington, DC, U. S.)* **2006**, *106* (3), 1105-1136.
181. Halamkova, L.; Halamek, J.; Bocharova, V.; Szczupak, A.; Alfonta, L.; Katz, E., Implanted Biofuel Cell Operating in a Living Snail. *J. Am. Chem. Soc.* **2012**, *134* (11), 5040-5043.
182. Alberola-Borràs, J.-A.; Vidal, R.; Mora-Seró, I., Evaluation of multiple cation/anion perovskite solar cells through life cycle assessment. *Sustainable Energy & Fuels* **2018**, *2* (7), 1600-1609.

183. Kymakis, E.; Amaratunga, G. A. J., Single-wall carbon nanotube/conjugated polymer photovoltaic devices. *Appl. Phys. Lett.* **2002**, *80* (1), 112-114.
184. Kaniber, S. M.; Simmel, F. C.; Holleitner, A. W.; Carmeli, I., The optoelectronic properties of a photosystem I–carbon nanotube hybrid system. *Nanotechnology* **2009**, *20* (34), 345701.
185. Kaniber, S. M.; Brandstetter, M.; Simmel, F. C.; Carmeli, I.; Holleitner, A. W., On-Chip Functionalization of Carbon Nanotubes with Photosystem I. *J. Am. Chem. Soc.* **2010**, *132* (9), 2872-2873.
186. Le Blanc, G.; Winter, K. M.; Crosby, W. B.; Jennings, G. K.; Cliffler, D. E., Integration of Photosystem I with Graphene Oxide for Photocurrent Enhancement. *Adv. Energy Mater.* **2014**, *4* (9), n/a.
187. Endo, M.; Muramatsu, H.; Hayashi, T.; Kim, Y. A.; Terrones, M.; Dresselhaus, M. S., Nanotechnology: 'Buckypaper' from coaxial nanotubes. *Nature (London, U. K.)* **2005**, *433* (7025), 476.
188. Elouarzaki, K.; Bourourou, M.; Holzinger, M.; Le Goff, A.; Marks, R. S.; Cosnier, S., Freestanding HRP-GOx redox buckypaper as an oxygen-reducing biocathode for biofuel cell applications. *Energy Environ. Sci.* **2015**, *8* (7), 2069-2074.
189. Ngo, L. T.; Tran, T. P.; Ngo, V. K. T.; Do, Q. H., High performance supercapacitor based on thick buckypaper/polyaniline composite electrodes. *Adv. Nat. Sci.: Nanosci. Nanotechnol.* **2019**, *10* (2), 25004.
190. Salve, M.; Amreen, K.; Rajurkar, P.; Pattnaik, P. K.; Goel, S., Miniaturized disposable buckypaper-polymer substrate based electrochemical purine sensing platform. *ECS Trans.* **2020**, *98* (11), 51-58.

191. Gross, A. J.; Robin, M. P.; Nedellec, Y.; O'Reilly, R. K.; Shan, D.; Cosnier, S., Robust bifunctional buckypapers from carbon nanotubes and polynorbornene copolymers for flexible engineering of enzymatic bioelectrodes. *Carbon* **2016**, *107*, 542-547.
192. Chen, X.; Yin, L.; Lv, J.; Gross, A. J.; Le, M.; Gutierrez, N. G.; Li, Y.; Jeerapan, I.; Giroud, F.; Berezovska, A.; O'Reilly, R. K.; Xu, S.; Cosnier, S.; Wang, J., Stretchable and Flexible Buckypaper-Based Lactate Biofuel Cell for Wearable Electronics. *Adv. Funct. Mater.* **2019**, *29* (46), 1905785.
193. Masi, M.; Bollella, P.; Riedel, M.; Lisdat, F.; Katz, E., Photobiofuel Cell with Sustainable Energy Generation Based on Micro/Nanostructured Electrode Materials. *Acs Appl Energ Mater* **2020**, *3* (10), 9543-9549.
194. Reeves, S. G.; Hall, D. O., Higher plant chloroplasts and grana: General preparative procedures (excluding high carbon dioxide fixation ability chloroplasts). In *Methods in Enzymology*, San Pietro, A., Ed. Academic Press: 1980; Vol. 69, pp 85-94.
195. Bourourou, M.; Elouarzaki, K.; Holzinger, M.; Agnès, C.; Le Goff, A.; Reverdy-Bruas, N.; Chaussy, D.; Party, M.; Maaref, A.; Cosnier, S., Freestanding redox buckypaper electrodes from multi-wall carbon nanotubes for bioelectrocatalytic oxygen reduction via mediated electron transfer. *Chem Sci* **2014**, *5* (7), 2885-2888.
196. Elouarzaki, K.; Bourourou, M.; Holzinger, M.; Le Goff, A.; Marks, R. S.; Cosnier, S., Freestanding HRP–GOx redox buckypaper as an oxygen-reducing biocathode for biofuel cell applications. *Energy & Environmental Science* **2015**, *8* (7), 2069-2074.
197. Gross, A. J.; Holzinger, M.; Cosnier, S., Buckypaper bioelectrodes: emerging materials for implantable and wearable biofuel cells. *Energy & Environmental Science* **2018**, *11* (7), 1670-1687.

198. Sui, X.; Wagner, H. D., Tough Nanocomposites: The Role of Carbon Nanotube Type. *Nano Letters* **2009**, *9* (4), 1423-1426.
199. Vittal, R.; Gomathi, H.; Kim, K.-J., Beneficial role of surfactants in electrochemistry and in the modification of electrodes. *Advances in Colloid and Interface Science* **2006**, *119* (1), 55-68.
200. Muriel, M. L.; Narayanan, R.; Bandaru, P. R., The Modification of the Pore Characteristics of Activated Carbon, for Use in Electrical Double Layer Capacitors, through Plasma Processing. *ECS Transactions* **2017**, *77* (11), 533-544.
201. Feldberg, S. W., Effect of uncompensated resistance on the cyclic voltammetric response of an electrochemically reversible surface-attached redox couple: Uniform current and potential across the electrode surface. *J Electroanal Chem* **2008**, *624* (1), 45-51.
202. Tsierkezos, N. G.; Ritter, U., Influence of concentration of supporting electrolyte on electrochemistry of redox systems on multi-walled carbon nanotubes. *Physics and Chemistry of Liquids* **2012**, *50* (5), 661-668.
203. Wang, X.; Wei, H.; Liu, X.; Du, W.; Zhao, X.; Wang, X., Novel three-dimensional polyaniline nanothorns vertically grown on buckypaper as high-performance supercapacitor electrode. *Nanotechnology* **2019**, *30* (32), 325401.
204. Ounnunkad, S.; Minett, A. I.; Imisides, M. D.; Duffy, N. W.; Fleming, B. D.; Lee, C.-Y.; Bond, A. M.; Wallace, G. G., Comparison of the electrochemical behaviour of buckypaper and polymer-intercalated buckypaper electrodes. *J Electroanal Chem* **2011**, *652* (1), 52-59.
205. Nicholson, R. S., Theory and Application of Cyclic Voltammetry for Measurement of Electrode Reaction Kinetics. *Analytical Chemistry* **1965**, *37* (11), 1351-1355.

206. Smalley, J. F.; Finklea, H. O.; Chidsey, C. E. D.; Linford, M. R.; Creager, S. E.; Ferraris, J. P.; Chalfant, K.; Zawodzinsk, T.; Feldberg, S. W.; Newton, M. D., Heterogeneous Electron-Transfer Kinetics for Ruthenium and Ferrocene Redox Moieties through Alkanethiol Monolayers on Gold. *Journal of the American Chemical Society* **2003**, *125* (7), 2004-2013.
207. Moldenhauer, J.; Meier, M.; Paul, D. W., Rapid and Direct Determination of Diffusion Coefficients Using Microelectrode Arrays. *J Electrochem Soc* **2016**, *163* (8), H672-H678.
208. Randviir, E. P., A cross examination of electron transfer rate constants for carbon screen-printed electrodes using Electrochemical Impedance Spectroscopy and cyclic voltammetry. *Electrochim Acta* **2018**, *286*, 179-186.
209. Metters, J. P.; Houssein, S. M.; Kampouris, D. K.; Banks, C. E., Paper-based electroanalytical sensing platforms. *Analytical Methods* **2013**, *5* (1), 103-110.
210. Foster, C. W.; Metters, J. P.; Kampouris, D. K.; Banks, C. E., Ultraflexible Screen-Printed Graphitic Electroanalytical Sensing Platforms. *Electroanalysis* **2014**, *26* (2), 262-274.
211. Mustafa, I.; Lopez, I.; Younes, H.; Susantyoko, R. A.; Al-Rub, R. A.; Almheiri, S., Fabrication of Freestanding Sheets of Multiwalled Carbon Nanotubes (Buckypapers) for Vanadium Redox Flow Batteries and Effects of Fabrication Variables on Electrochemical Performance. *Electrochim Acta* **2017**, *230*, 222-235.
212. Gizzie, E. A.; LeBlanc, G.; Jennings, G. K.; Cliffel, D. E., Electrochemical Preparation of Photosystem I-Polyaniline Composite Films for Biohybrid Solar Energy Conversion. *Acs Appl Mater Inter* **2015**, *7* (18), 9328-9335.
213. Ngo, L. T.; Tran, T. P.; Ngo, V. K. T.; Do, Q. H., High performance supercapacitor based on thick buckypaper/polyaniline composite electrodes. *Advances in Natural Sciences: Nanoscience and Nanotechnology* **2019**, *10* (2), 025004.

214. Gust, D.; Moore, T. A.; Moore, A. L., Solar Fuels via Artificial Photosynthesis. *Acc. Chem. Res.* **2009**, *42* (12), 1890-1898.
215. Ong, W.-J.; Tan, L.-L.; Ng, Y. H.; Yong, S.-T.; Chai, S.-P., Graphitic Carbon Nitride (g-C₃N₄)-Based Photocatalysts for Artificial Photosynthesis and Environmental Remediation: Are We a Step Closer To Achieving Sustainability? *Chem. Rev. (Washington, DC, U. S.)* **2016**, *116* (12), 7159-7329.
216. Meyer, T. J., Chemical approaches to artificial photosynthesis. *Acc. Chem. Res.* **1989**, *22* (5), 163-70.
217. Golbeck, J. H., Structure and function of photosystem I. *Annu. Rev. Plant Physiol. Plant Mol. Biol.* **1992**, *43*, 293-324.
218. Fromme, P.; Jordan, P.; Krauß, N., Structure of photosystem I. *Biochimica et Biophysica Acta (BBA) - Bioenergetics* **2001**, *1507* (1), 5-31.
219. Amunts, A.; Drory, O.; Nelson, N., The structure of a plant photosystem I supercomplex at 3.4 Å resolution. *Nature* **2007**, *447* (7140), 58-63.
220. Grimme, R. A.; Lubner, C. E.; Bryant, D. A.; Golbeck, J. H., Photosystem I/Molecular Wire/Metal Nanoparticle Bioconjugates for the Photocatalytic Production of H₂. *J. Am. Chem. Soc.* **2008**, *130* (20), 6308-6309.
221. Li, T.; Yang, M., Electrochemical sensor utilizing ferrocene loaded porous polyelectrolyte nanoparticles as label for the detection of protein biomarker IL-6. *Sens. Actuators, B* **2011**, *158* (1), 361-365.
222. Desmaele, D.; Nguyen-Boisse, T. T.; Renaud, L.; Tingry, S., Integration of cantilevered porous electrodes into microfluidic co-laminar enzymatic biofuel cells: Toward higher enzyme loadings for enhanced performance. *Microelectron. Eng.* **2016**, *165*, 23-26.

223. Cai, J.; Gou, X.; Sun, B.; Li, W.; Li, D.; Liu, J.; Hu, F.; Li, Y., Porous graphene-black phosphorus nanocomposite modified electrode for detection of leptin. *Biosens. Bioelectron.* **2019**, *137*, 88-95.
224. Ciesielski, P. N.; Scott, A. M.; Faulkner, C. J.; Berron, B. J.; Cliffel, D. E.; Jennings, G. K., Functionalized Nanoporous Gold Leaf Electrode Films for the Immobilization of Photosystem I. *ACS Nano* **2008**, *2* (12), 2465-2472.
225. He, Y.; Wang, X.; Huang, H.; Zhang, P.; Chen, B.; Guo, Z., In-situ electropolymerization of porous conducting polyaniline fibrous network for solid-state supercapacitor. *Appl. Surf. Sci.* **2019**, *469*, 446-455.
226. Hasan, K.; Milton, R. D.; Grattieri, M.; Wang, T.; Stephanz, M.; Minteer, S. D., Photobioelectrocatalysis of Intact Chloroplasts for Solar Energy Conversion. *ACS Catal.* **2017**, *7* (4), 2257-2265.
227. Sjöholm, K. H.; Rasmussen, M.; Minteer, S. D., Bio-Solar Cells Incorporating Catalase for Stabilization of Thylakoid Bioelectrodes during Direct Photoelectrocatalysis. *Ecs Electrochem Lett* **2012**, *1* (5), G7-G9.
228. Wang, T.; Reid, R. C.; Minteer, S. D., A Paper-Based Mitochondrial Electrochemical Biosensor for Pesticide Detection. *Electroanalysis* **2016**, *28* (4), 854-859.
229. Hecht, D. S.; Hu, L.-B.; Irvin, G., Emerging Transparent Electrodes Based on Thin Films of Carbon Nanotubes, Graphene, and Metallic Nanostructures. *Adv. Mater. (Weinheim, Ger.)* **2011**, *23* (13), 1482-1513.
230. Rasmussen, M.; Minteer, S. D., Investigating the mechanism of thylakoid direct electron transfer for photocurrent generation. *Electrochim. Acta* **2014**, *126*, 68-73.

231. Xiao, X.; Wang, M. e.; Li, H.; Si, P., One-step fabrication of bio-functionalized nanoporous gold/poly(3,4-ethylenedioxythiophene) hybrid electrodes for amperometric glucose sensing. *Talanta* **2013**, *116*, 1054-1059.
232. Zhang, Z.; Liu, H.; Deng, J., A Glucose Biosensor Based on Immobilization of Glucose Oxidase in Electropolymerized o-Aminophenol Film on Platinized Glassy Carbon Electrode. *Analytical Chemistry* **1996**, *68* (9), 1632-1638.
233. He, Y.; Wang, X.; Huang, H.; Zhang, P.; Chen, B.; Guo, Z., In-situ electropolymerization of porous conducting polyaniline fibrous network for solid-state supercapacitor. *Applied Surface Science* **2019**, *469*, 446-455.
234. Gizzie, E. A.; LeBlanc, G.; Jennings, G. K.; Cliffel, D. E., Electrochemical Preparation of Photosystem I–Polyaniline Composite Films for Biohybrid Solar Energy Conversion. *Acs Appl Mater Inter* **2015**, *7* (18), 9328-9335.
235. Choi, D. J.; Boscá, A.; Pedrós, J.; Martínez, J.; Barranco, V.; Rojo, J. M.; Yoo, J. J.; Kim, Y.-H.; Calle, F., Improvement of the adhesion between polyaniline and commercial carbon paper by acid treatment and its application in supercapacitor electrodes. *Composite Interfaces* **2016**, *23* (2), 133-143.
236. Kazemzadeh, S.; Riazi, G.; Ajeian, R., Novel Approach of Biophotovoltaic Solid State Solar Cells Based on a Multilayer of PS1 Complexes as an Active Layer. *ACS Sustainable Chem. Eng.* **2017**, *5* (11), 9836-9840.
237. Wolfe, K. D.; Dervishogullari, D.; Passantino, J. M.; Stachurski, C. D.; Jennings, G. K.; Cliffel, D. E., Improving the stability of photosystem I–based bioelectrodes for solar energy conversion. *Current Opinion in Electrochemistry* **2020**, *19*, 27-34.

